Nicolaus Copernicus Astronomical Center
Polish Academy of Sciences

Observational constraints on jet production efficiency in Active Galactic Nuclei

Author: Katarzyna Rusinek-Abarca

Supervisor: Prof. Marek Sikora

January 2022

Contents

Abstract

The main goal of this thesis is to investigate the jet production efficiency in Active Galactic Nuclei (AGN), distinguishing between radio-quiet (RQ) and radio-loud (RL) AGNs. From radio observations we observe not only a significant scatter of these efficiencies (4-5 orders of magnitude) but also unusually large jet powers (P_j) among RL objects, sometimes exceeding their accretion powers ($P_{\rm accr} = \dot{M}c^2 = L_{\rm bol}/\epsilon_d$, where $L_{\rm bol}$ is the bolometric luminosity and ϵ_d is the radiative efficiency) of these AGNs. This in turn leads to four questions: (1) what exactly causes such a large range of jet production efficiencies ($\eta_j \equiv P_j/P_{\rm accr}$); (2) is there only one mechanism uniformly responsible for the production of jets we observe (among RQ and RL objects) or are there several different processes; (3) does the production of the strong jets observed in RL objects correspond to the crossing of a specific threshold(s); (4) how are the most powerful observed jets obtained?

The answers to the above questions have been sought after over the past five years of doctoral studies (2016-2021) through careful analyses of diverse sets of AGNs, presented in three peer-reviewed papers. Although these studies, when compared among themselves, may seemingly appear inconsistent (described below), from all the collected results and their theoretical considerations a coherent picture emerges that leads to the same conclusion – namely, not all AGNs are able to produce very strong jets, where the appropriate accumulation of the magnetic field at the center is an extremely important factor, as the only model explaining the existence of jets with the highest strengths is the magnetically arrested disk (MAD) scenario. In this model, jets are produced in the Blandford-Znajek mechanism, where they are powered by the rotational energy of the black hole, and the high efficiency of their production is ensured by the large flux of the magnetic field sustained on the black hole (BH) by the pressure of its accreting matter.

In Paper I, the jet production efficiencies were analyzed for four diverse sets of AGNs, whose common feature was the presence of a pair of FR II type radio lobes which provide the possibility of calculating their jet powers from the calorimetry of these lobes. A comparison of these objects showed a clear decrease in the jet production efficiency at higher accretion rates ($\lambda_{\rm Edd} \equiv L_{\rm bol}/L_{\rm Edd}$). Such a decrease, which could be explained by the transition from a radiatively inefficient, optically thin, but geometrically thick accretion disk to an optically thick and geometrically thin standard disk, which occurs for objects with moderate accretion rates ($\lambda_{\rm Edd} \sim 0.01$) where $P_j > L_{\rm bol}$ suggests the presence of MAD in these sources while assuming thicker accretion disks than the standard theory predicts.

In Paper II, we focused on studying the radio bimodality (i.e. the radio loudness distribution, $R = L_{\rm radio}/L_{\rm optical}$, illustrating $\sim P_j/L_{\rm bol}$) in one carefully selected and extremely homogeneous

sample of AGNs. Our research confirmed the bimodal distribution of radio loudness and revealed a deficit of jets with intermediate jet production efficiencies (calculated analogously to those in Paper I but with a limited number of objects with double radio lobes) implying the existence of a certain threshold(s) condition(s) for the production of the strongest jets. Finally we considered in detail various scenarios of the MAD formation.

In Paper III, we analyzed how the RL fraction (RLF) of quasars (QSOs) changes with cosmic time. In order to do so, as a first step, similarly to Paper II, we carefully selected the objects under study creating three subsets for which we found a decrease in RLF with an increase in redshift. Furthermore, by removing the bias implied by the dependence of RLF on the redshift by narrowing its range, we were able to examine more closely the dependence of RLF on BH mass and Eddington ratio finding an increase in RLF with an increase in $M_{\rm BH}$ and no dependence between RLF and $\lambda_{\rm Edd}$. Putting together all the results obtained in this work we get an even steeper decrease in RLF with redshift. We made an attempt at linking these findings with the possible scenarios of the MAD formation, with a focus on the types of galaxy mergers being responsible for triggering AGN activity.

Streszczenie

(Abstract in Polish)

Głównym celem rozprawy jest zbadanie efektywności produkcji dżetów w Aktywnych Jądrach Galaktyk (AGN-ach) przy rozróżnieniu AGN-ów na radiowo-ciche (RQ) i radiowo-głośne (RL). Bazując na obserwacjach radiowych, notowany jest nie tylko znaczny rozrzut tychże efektywności (4-5 rzędów wielkości), ale też niezwykle duże moce dżetów (P_j) wśród obiektów RL, niekiedy przewyższające moce akrecyjne ($P_{\rm accr} = \dot{M}c^2 = L_{\rm bol}/\epsilon_d$, gdzie $L_{\rm bol}$ to jasność bolometryczna oraz ϵ_d to efektywność promienista) tychże AGN-ów. To z kolei prowadzi do pytań: (1) co dokładnie powoduje tak duży zakres efektywności produkcji dżetów ($\eta_j \equiv P_j/P_{\rm accr}$); (2) czy za produkcję obserwowanych przez nas dżetów (wśród obiektów RQ i RL) odpowiada tylko jeden i ten sam mechanizm, czy mamy kilka różnych procesów; (3) czy produkcja silnych dżetów obserwowanych w obiektach RL wiąże się ze spełnieniem jakiegoś warunku/ów granicznego/ych (tj. *threshold*); (4) w jaki sposób otrzymujemy najpotężniejsze z obserwowanych dżetów?

Odpowiedzi na powyższe pytania poszukiwane były w ciągu ostatnich pięciu lat studiów (2016-2021) poprzez staranne analizy różnorodnych zbiorów AGN-ów, przedstawione w trzech recenzowanych pracach. Mimo, iż pozornie badania te, gdy porównane między sobą, mogą wydawać się niekonsystentne (opisane poniżej), to jednak wszystkie zebrane rezultalty oraz ich teoretyczne rozważania wyłaniają spójny obraz i prowadzą do tego samego wniosku – mianowicie nie wszystkie AGN-y są w stanie wytworzyć bardzo silne dżety, gdzie niezywkle istotnym czynnikiem jest odpowiednie nagromadzenie pola magnetycznego w centrum, jako iż jedynym modelem tłumaczącym istnienie dżetów o największych mocach jest model magnetycznie blokowanej akrecji (MAD). W modelu tym dżety produkowane sę w mechanizmie Blandforda-Znajka w którym to są one zasilane energią rotacyjną czarnej dziury zaś duży strumień pola magnetycznego podtrzymywanego na czarnej dziurze przez ciśnienie naporowe akreującej na czarną dziurę (BH) materii zapewnia wysoką efektywność ich produkcji.

W Pracy I analizowane były efektywności produkcji dżetów dla czterech różnorodnych zbiorów AGN-ów, których cechą wspólną była obecność pary płatów radiowych typu FR II, a tym samym możliwość obliczenia ich mocy dżetów z jasności radiowych stosując kalorymetrię tychże płatów. Zestawienie tych obiektów pokazało wyraźny spadek efektywności produkcji dżetów na wyższych tempach akrecji ($\lambda_{\rm Edd} \equiv L_{\rm bol}/L_{\rm Edd}$). Taki spadek, choć mógłby być tłumaczony przejściem między promieniście nieefektywnym, cienkim optycznie, ale grubym geometrycznie, dyskiem akrecyjnym do dysku standardowego, optycznie grubego i geometrycznie cienkiego, to ze względu na obiekty

o średnich tempach akrecji ($\lambda_{\rm Edd} \sim 0.01$), w których $P_j > L_{\rm bol}$ sugeruje obecność MAD-u w tych obiektach, ale przy założeniu grubszych, niż standardowa teoria przewiduje, dysków akrecyjnych.

W Pracy II skupiliśmy się na zbadaniu bimodalności radiowej (tj. rozkładu głośności radiowej, $R = L_{\rm radio}/L_{\rm optical}$, obrazującej $\sim P_j/L_{\rm bol}$) w jednym, starannie wyselekcjonowanym i niezwykle jednorodnym zbiorze AGN-ów. Nasze badania potwierdziły bimodalny rozkład głośności radiowej oraz ujawniły deficyt dżetów o średnich efektywnościach produkcji dżetów (liczonych analogicznie jak w Pracy I jednak z ograniczoną liczbą obiektów z podwójnymi płatami radiowymi) implikując istnienie pewnych warunków granicznych (tj. *threshold*) umożliwiających powstawanie najsilnieszych dżetów. Pracę zakończyliśmy omówieniem różnych możliwych scenariuszy odpowiedzialnych za powstawanie mechanizmu MAD-u.

W Pracy III przeanalizowaliśmy jak zmienia się frakcja RL (RLF) kwazarów (QSOs) z czasem kosmicznym. W tym celu w pierwszym kroku, podobnie jak w Pracy II uważnie wybraliśmy badane obiekty tworząc trzy podzbiory, dla których znaleźliśmy spadek RLF wraz ze wzrostem redshiftu. Dalej, usuwając bias implikowany przez zależność RLF od redshiftu poprzez ustalenie jego wąskiego zakresu, mogliśmy dokładnie zbadać zależność RLF od masy czarnej dziury oraz tempa akrecji znajdując wzrost RLF ze wzrostem $M_{\rm BH}$ oraz brak zależności między RLF a $\lambda_{\rm Edd}$. Zestawiając razem wszystkie otrzymane w tej pracy rezultaty otrzymujemy jeszcze bardziej stromy spadek RLF z redshiftem. Na koniec podjęliśmy próbę powiązania tych wyników z możliwymi scenariuszami powstawania MAD, ze szczególnym uwzględnieniem typów zderzeń galaktyk, które mogą być odpowiedzialne za wyzwolenie aktywności AGN.

Acknowledgments

First and foremost I would like to thank my supervisor, Prof. Marek Sikora without whom the beginning, the course, and the end of my doctoral studies would have been simply impossible. Not only did he support me throughout all these years of my scientific journey, but also discussed many topics both more and less familiar to me, both academic and non-scientific, as well as constantly answering my countless questions. His presence and availability, kind and understanding approach, encouragement and motivation throughout all these years were, are, and will always be greatly appreciated by me.

Studies at the Nicolaus Copernicus Astronomical Center have allowed me to meet many fascinating, intriguing, and warm-hearted people from all over the world. While some of them participated in my life for a short time, with others I traveled and shared a lot, and a special few eventually became my closest of friends. I am grateful for all of them as each and everyone provided me with precious time and life experience. I sincerely hope that those who are in my life nowadays will continue to be for a long enough time.

Many other people contributed in my studies, more and less significantly. The technical and administrative staff of the Center ensured that all the other, non-scientific, and yet quite important aspects went smoothly allowing me to stay focused over this period.

I would definitely not be in my current place in life if not for my parents. Even though my last years had to be definitely cosmic for them (which in Polish would gain an additional meaning – being somewhat crazy) they have always been no less than immensely supportive and helpful, giving me their trust and faith. It is my pleasure to notify them that another chapter of my life, the chapter they have been waiting for for some time, is about to be complete.

Last but tremendously far from least I would like to thank from the very bottom of my heart my best friend, my greatest life companion, and my beloved husband – David Abarca (behind whose name I am also awaiting to add magical Ph.D.!). He has been with me for nearly all the years of my doctoral studies, for better or for worse, through plenty of various works and activities. Without his assistance in all spheres of my life, moments of joy and laugh, unbelievable amount of patience, and many other features (that I cannot so splendidly describe in words) and the days we spent together, I would never have reached this stage. The last few (pandemic) years, even though they have been quite challenging, were incredibly adventurous and resulted in many superb outcomes, and I am more than excited when looking forward to our next decades together.

1 Introduction

1.1 Historical background

The first observation of a jet in an *Active Galactic Nucleus* (AGN) was obtained in the optical regime and belongs to Curtis (1918) who reported 'a curious straight ray... apparently connected with the nucleus by a thin line of matter' in the nebula M 87. At the time neither the rays nor the nebulae were understood. While the latter were rather considered to be galactic sources, the former remained an unstudied mystery for nearly 40 years when Baade and Minkowski (1954b) considered it to be a rapid outflow 'formed by ejection from the nucleus' and termed it a *jet*.

Great progress in the study of AGNs, as well as jets, was achieved especially with the development of radio astronomy (e.g. Jansky 1933; Reber 1944; Ryle and Smith 1948, and many more). Some of the newly discovered radio sources were revealed to have quite extended, symmetrical morphologies with at least two distinct centres of radio emission (precursor of which is Cygnus A, Hanbury Brown et al. 1952; Jennison and Das Gupta 1953). This, together with the linkage of these objects with their counterparts in the visible spectrum (Bolton et al. 1949; Baade and Minkowski 1954a) and later also in the high energy regime (Giacconi et al. 1962; Bowyer et al. 1964; Friedman and Byram 1967; Bowyer et al. 1970), indicated that the nature of these sources was quite complex. They were readily observable over a diverse range of domains of the electromagnetic spectrum and their core emitting regions were constrained to span only a few light days.

The real breakthrough in the understanding of AGNs stems from optical observations. 3C 273 and 3C 48, strong radio sources, were found to be not only extremely bright and variable, appearing as blue star-like images (hence the name *quasars*, QSOs, from *quasi-stellar radio sources*)[1] but also to have redshifts greater than 0.1 (0.16 and 0.37, respectively, Hazard et al. 1963; Greenstein 1963; Oke 1963; Schmidt 1963). This remarkable discovery was not linked to the extragalactic nature of these sources at first.[2]

Objects analogous to quasars (regarding their optical characteristics but differing in the detectability of their radio emission) were noticed by Sandage (1965) who stated that such sources (named *quasi-stellar galaxies*) are about a thousand times more numerous. This finding was the first hint towards a radio bimodality in AGNs.

[1] When first discovered, QSOs and AGNs were treated as separate classes of objects. However, since the physical nature of quasar nuclei relates to accretion, just as in AGNs (and which is described more in the next paragraphs and Sections), QSOs are in fact a subclass of AGNs being their most luminous representatives.

[2] At the time all three kinds of redshifts were considered, i.e. Doppler, gravitational, and cosmological.

The vast number of discoveries (with only some of them being outlined above) were yearning for explanations, the most challenging of which concerned the powering of AGNs. The answer to this puzzle came from Hoyle and Fowler (1963a,b) who proposed a singular energy source in the form of a supermassive star (up to $\sim 10^8\,M_\odot$). This concept was further developed independently by Salpeter (1964) and Zel'dovich (1964) who instead of the contraction of such a massive star suggested the accretion of matter onto a supermassive black hole (SMBH) and which was later supported by Lynden-Bell (1969), Rees (1978), and more.

Finally, with a focus on jets, a troublesome aspect concerned the formation of the double radio morphologies of AGNs which were at first thought to be a pair of plasma blobs ejected from the nuclei during a single event (Shklovskii 1963). This, however, stood against the enormous energy of $\sim 10^{60}\,\mathrm{erg\,s^{-1}}$ indicated by synchrotron radiation widely accepted to be the basic mechanism for radio emission in AGNs (Burbidge 1959). Suggested by Rees (1971) and analyzed more by Blandford and Rees (1974), the idea of jets as relativistic beams transporting plasma out of the nucleus in a continuous manner was proposed. Known as the '*twin exhaust model*', the mechanism for the production of bipolar flows to power the lobes was soon supported by more detailed radio observations, revealing hotspots as well as linear, curved, bent, and more complex structures on small distance scales (Miley 1980; Bridle and Perley 1984).

More than a century after the discovery of AGNs and their jets, our knowledge of them has grown unimaginably large while simultaneously producing just as many, if not more, questions than answers. We still do not fully understand the mechanisms behind the formation, powering, collimation, and acceleration of jets, as well as why they are not present in all AGNs. Does the production of powerful jets require special conditions? Is there a specific threshold controlling the activation of such phenomenon? Do we observe weaker jets as well and if so – are they produced by the same mechanism as their more energetic cousins? While some of these issues have been investigated in the past (see e.g. the review by Blandford et al. 2019, and refs. therein, but also the content of this very work), this dissertation aims to enrich the current state of knowledge by answering these (and other) questions.

1.2 Active Galactic Nuclei

It is now well known that at the center of almost every galaxy lies a **supermassive black hole** (with masses laying within a range of 10^6 up to 10^{10} solar masses), the natural outcome of which, if any matter is present in its vicinity, is accretion. In case of Active Galactic Nuclei, the SMBH is the actual *nucleus* and accretion is considered to be the primary power source responsible for the whole structure of an AGN. AGNs are observed across nearly the entire electromagnetic spectrum, from radio waves up to X-rays (and occasionally even γ-rays), resulting from thermal and non-thermal, primary and secondary, radiation (as shown in Figure 1.1 and discussed below).

The infalling matter forms an **accretion disk**, studied thoroughly, analytically, numerically, and through observations, by many (see reviews by Netzer, 2015 and Davis and Tchekhovskoy, 2020, and refs. therein). Many factors decide about the specific structure and properties of an accretion disk (and, consequently, other components of AGNs as described later), among which the most important are the black hole mass (M_{BH}) and spin (a), accretion rate ($\dot{M}$) and magnetic field strength and topology.

Out of these, the parameter for which the accretion disk structure is most dependent is $\dot{M}$, or more strictly $\dot{M}/M \propto \lambda_{\rm Edd}$ where the $\lambda_{\rm Edd}$ is the Eddington ratio being the ratio of the AGN bolometric luminosity ($L_{\rm bol}$) and the Eddington luminosity ($L_{\rm Edd} = 1.26 \times 10^{38} \times M/M_{\odot}\,{\rm erg\,s^{-1}}$ with $M_{\odot}$ being the solar mass),

$$\lambda_{\rm Edd} = L_{\rm bol}/L_{\rm Edd}. \tag{1.1}$$

The vast majority of AGNs studied in this dissertation accrete at 'moderate' rates, between 1% and 30% of Eddington luminosity. Within this range of Eddington ratios the standard models of accretion disks predict they are cold ($T < 10^5$ K), optically thick ($\tau_{\rm eff} \gg 1$), geometrically thin ($H/R < 0.1$ with H and R denoting the height and radius of the given disk ring, respectively), and radiatively efficient ($\epsilon_d = L_{\rm bol}/\dot{M}c^2 \gtrsim 0.1$, where ϵ_d is the radiative efficiency). They are referred to as classic '*standard disks*', and were introduced by Shakura and Sunyaev (1973) with the relativistic version derived by Novikov and Thorne (1973).

The typical spectral energy distribution (SED) of such AGNs is presented in Figure 1.1 and described below.

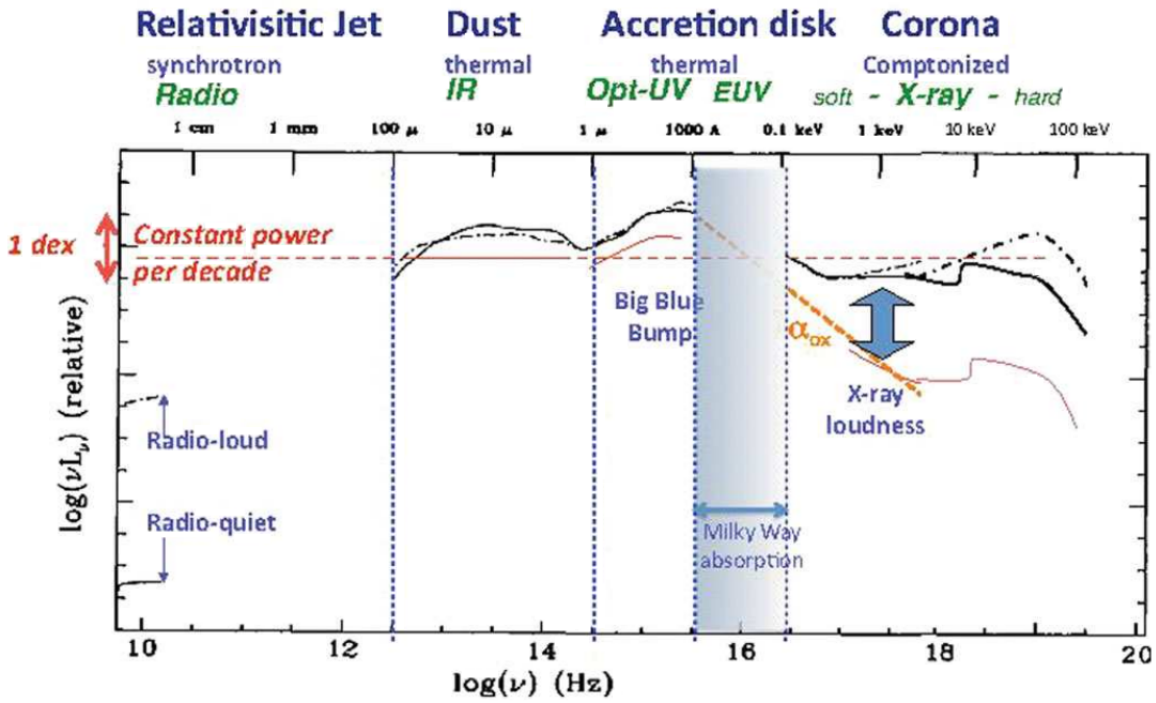

Figure 1.1: An example spectral energy distribution of an AGN accreting at a moderate accretion rate. Sources (top line) and mechanisms of radiation (middle line) in given spectral regimes (bottom line) contributing to the overall complex shape are denoted with text above the graph. Adopted from Elvis (2010).

Observed mostly in the optical and UV range in the form of the 'Big Blue Bump', the emission from the accretion disk is in fact the superposition of black-body radiation produced at different distances from the BH being the hottest in the innermost region.

The accretion disk and its corona excite and ionize the matter in the nearby areas outside the disk, which is manifested by strong emission lines in the spectra of AGNs (see e.g. Antonucci 1993; Zheng et al. 1997; Netzer 2015). These lines, being a result of allowed and forbidden transitions, and consequently having different densities, can be divided due to their full width at half maximum (FWHM)

into narrow ($< 1000\,\mathrm{km\,s^{-1}}$) and broad ($> 1000\,\mathrm{km\,s^{-1}}$) lines indicating the different velocities of the clouds they are created within. Hence we distinguish the **broad-line region** (BLR) and **narrow-line region** (NLR) located in a few tenths and a few tens of parsecs, respectively.

At a larger distance from the SMBH, behind the disk and beyond the sublimation radius with warm temperatures of $\sim 100\,\mathrm{K}-1500\,\mathrm{K}$, (Miley et al. 1985; Krolik and Begelman 1988) matter forms a **torus** – a dusty and opaque structure which absorbs some of the emission from the disk and re-radiates it in the infrared regime. The torus plays a vital role in understanding the spectra of those AGNs which are observed at large inclination angles and in which the UV emission is strongly reduced and the broad emission lines are not visible, both being a result of the obscuration of the internal regions of AGNs precisely by the torus, i.e. when a source is inclined to the observer.

The mechanisms responsible for the emission in the least and most energetic domains, i.e. radio and high X-rays, involve synchrotron emission and thermal Comptonization, respectively. In the radio domain we note quite a large spread in luminosity forming two specific branches (radio-loud and radio-quiet, see Section 1.3.3). These very unique characteristics of AGNs depict a variety of origins of the observed emission, and among them those of special interest to me, i.e. **jets**. Detailed discussions on radio properties of AGNs (their morphologies with the emphasis on the **radio lobes**, and the origins of the observed emission) and jets (especially their strongest representatives) are given in Sections 1.3 and 1.4, respectively.

Information about the spectral energy distribution is necessary for the estimation of the bolometric luminosity of accretion flows. This, however, is only the case for Type 1 AGNs, where the division into Type 1 and Type 2 is based on the presence and lack of the broad emission lines, accordingly, and thus the orientation of the source to the observer (Antonucci 1993). In Type 2 AGNs, in which the inner regions are not seen (and with them – the broad emission lines) the bolometric luminosities can be deduced from mid-IR (MIR) luminosities (see Gupta et al. 2020, and refs. therein) or from narrow line luminosities (Netzer 2009).

The division into Type 1 and Type 2 AGNs is further important when it comes to the BH mass estimations. While in the former the broad emission lines can be used (e.g. Hα or Hβ, Greene and Ho 2005; Trakhtenbrot and Netzer 2012) in the latter their relations with the near-IR (NIR) luminosities of their host galaxies have to be applied (e.g. Marconi and Hunt 2003; Graham 2007).

Even though standard accretion disks can reproduce basic features observed in their spectral properties, the theory behind these disks has its drawbacks (e.g. Begelman and Pringle 2007; Różańska et al. 2015; Sądowski 2016; Davis and Tchekhovskoy 2020). The major ones refer to the thermal instability (which is predicted by theory but not seen in observations), self-gravity (which can lead to fragmentation of the accretion disk, Goodman 2003), and the smaller sizes of accretion disks than indicated by microlensing (Blackburne et al. 2011; Morgan et al. 2018). As shown in studies by Sądowski (2016), Begelman and Silk (2017), Dexter and Begelman (2019), and Lančová et al. (2019) the above disagreements can be avoided by assuming, contrary to standard accretion disk theory, that the dominant contribution to the pressure in accretion disks is provided by large scale magnetic fields. Such disks are called 'magnetically elevated'.

The brief description of the spectral energy distribution provided above refers to AGNs accreting at moderate accretion rates and being observed at inclination angles small enough to be not obscured by the dusty tori, but big enough to avoid domination of the observed radiation spectrum by Doppler

boosted radiation from jets (which is the case for blazars, see e.g. Urry and Padovani 1995). At very high and very low accretion rates the geometry and physical structure of the accretion flow changes quite drastically. There, the disks become geometrically thick and radiatively inefficient (see Abramowicz et al. 1988 and the review by Yuan and Narayan 2014). These, in turn, strongly modify all the other elements of an AGN, making it extremely difficult to estimate their bolometric luminosities and radiative efficiencies.

1.3 Radio observations

Even though AGNs are observed throughout the whole electromagnetic spectrum, they display the most spectacular and diverse morphologies in the radio domain. While the most tremendous structures are powered by very strong jets, the radio emission in AGNs also has other origins, especially in the case of weaker radio sources. This section discusses the above and gives insights into the issue of radio bimodality.

1.3.1 Radio morphologies

Regarding the radio morphologies, AGNs can be simply divided into extended and compact. Such a separation, although it strongly depends on the radio interferometer used, its angular resolution and sensitivity, as well as the radio frequency at which the source is observed, is essential to understand the source of radio emission in a given AGN.

1.3.1.1 Extended sources

While thinking about the extended radio morphology of an AGN one usually refers to the presence of jets (on one or both sides of the nucleus) terminating in diffuse, quite symmetrically placed, lobes. Sources with such structure are named *double* or *triple* according to the visibility of the radio core corresponding to the optical center.

One of the first, and still commonly used, classifications of such lobed AGNs was done by Fanaroff and Riley (1974) who by comparing the radio luminosity and the surface brightness of particular elements of the radio morphology distinguished two classes:

- type I (FR I) which is characterized by a very bright central region with dimmer outer elements which are not well defined and slowly decrease their surface brightness with distance. Such sources are named *edge-darkened*;
- type II (FR II) representing objects with much higher surface brightness further from the core, concentrated in hotspots and lobes rather than around the central area. These sources are referred to as *edge-brightened*.

In the past the distinction between these two classes was quite sharp when comparing their radio luminosities (at 178 MHz) with type II being brighter than type I (Figure 1 in Owen and Ledlow 1994 and in Ledlow and Owen 1996). Recent studies show that many FR II AGNs are in fact as weak as FR I AGNs and that division based solely on the radio luminosity is inconclusive (Croston et al. 2018; Mingo et al. 2019; Kozieł-Wierzbowska et al. 2020; Macconi et al. 2020).

Together with radio morphology, the significant difference between two FR classes relates to the jets powering these objects. Usually visible on both sides of the nucleus, the FR I jets are transonic or mildly supersonic and prone to fluid instabilities, leading to turbulence and deceleration (Bicknell 1984) often resulting in distorted and plume-like structures. On the other hand, the FR II jets, with their smooth, narrow, and well-collimated form, are considered to be relativistic and highly supersonic. As a consequence these jets, despite often seen to be one-sided[3], allow radio sources associated with AGNs to reach bigger sizes and posses hotspots at the positions where the jets interact with the external medium. Whether the difference in jet speeds is driven by the environment or whether the engines that power both classes are different in nature is still an ongoing debate with a prevalence of the former (see review by Tadhunter 2016, and refs. therein).

Many other, much more complex, morphologies are noted when it comes to lobed AGNs. Called *HYbrid MOrphology Radio sources* (HyMoRS, Gopal-Krishna and Wiita 2000), these objects reveal mixed FR I/FR II morphology, i.e. a lobe of each kind located on each side of the nucleus, and may potentially inform about particle acceleration and the formation of a specific lobe structure (Harwood et al. 2020). AGNs with angled jets are found in galaxy clusters and allow for studies of the jet interactions with the surroundings of the AGNs. Depending on how big the angle is between curved jets, these objects are classified as *wide-angled tail* (WAT), *narrow-angled tail* (NAT), and *head-tail* (HT) sources with the latter having the most confusing structure in which both jets and lobes are merged into a single extended tail (e.g. Kozieł-Wierzbowska et al. 2020, and refs. therein).

Radio sources with mentioned above morphologies have typical sizes of tens to hundreds of kpc (e.g. Miley 1980; de Vries et al. 2006; van Velzen et al. 2015; Mingo et al. 2019) but there are sources known for their much greater extent, achieving even a few Mpc. Named as *giant radio sources* (GRSs; for objects bigger than 0.7 Mpc, Kuźmicz and Jamrozy 2012), their morphologies mostly resemble those of their smaller cousins, being doubles and triples, and are believed to be a result of an ongoing activity for a much longer time. As shown in many works, GRSs require very powerful jets (e.g. Kuźmicz et al. 2018) and often occur in regions of low galaxy density (e.g. Dabhade et al. 2020).

Finally, a special group of extended radio morphologies consists of AGNs in which more than one pair of lobes is visible. A plausible explanation is the observation of multiple phases of activity of a nucleus which is indeed the case for *double-double radio galaxies* (DDRGs) in which two pairs of double lobes with a common centre are seen[4]. The observed structures are collinear (within 10°, Schoenmakers et al. 2000) with all the lobes being similar and typical for FR II sources (even though they differ in brightness and in the diffusion of radio emission) which further allows for a distinction between the real inner lobes and fragments of jets (Nandi and Saikia 2012). A very peculiar subgroup of DDRGs are so called *X-shaped* sources in which the axes of the two pairs of double lobes are set at a significant angle to each other (Leahy and Parma 1992). There are many theories explaining their formation (with a solid review provided by Rottmann 2001) not all of which having to do with recurrent activity scenarios.

[3]One-sideness of the jets can be explained by: (1) the asymmetric energy transport with one of the jets carrying less energy; (2) asymmetric dissipation of energy in two directions of the jets; (3) relativistic beaming favoring the detection of the approaching jet over the receding one. A systematic asymmetry in the polarization properties of lobes in double radio sources strongly supports the last scenario (Garrington et al. 1988).

[4]Some sources, e.g. B0925+420 (Brocksopp et al. 2007) and J140948.85-030232.5 (Hota et al. 2011), have traces of activity from three different eras.

1.3.1.2 Compact sources

The extended morphologies described above are a genuine result of strong jets[5]. At smaller scales, the origin of the radio emission can be more perplexing when considering its main contribution, especially since star-forming regions (SFRs, e.g. Kimball et al. 2011), accretion disc winds (e.g. Zakamska et al. 2016), and/or accretion disc coronae (e.g. Raginski and Laor 2016) may dominate the detected radiation. In the case of jets, both weak (Smith et al. 2016) and strong ones are observed. With regards to the latter, a few groups of sources are recognized and described below.

Defined on the basis of their spectral properties (which are discussed in the next Section, 1.3.2), *gigahertz peaked spectrum* (GPS) and *compact steep spectrum* (CSS) objects constitute a significant fraction of AGNs (see the review by O'Dea and Saikia 2021). Sources from both of these classes are powerful ($L_{1.4\,\mathrm{GHz}} > 10^{25}\,\mathrm{W\,Hz^{-1}}$) and have convex synchrotron radio spectra with peak frequencies of $\sim$1 GHz and $\sim$100 MHz for GPS and CSS objects, respectively. Their radio morphologies mostly resemble those of classical FR II sources but with much smaller linear sizes, considered to be no bigger than 1 kpc for the former and less than 20 kpc for the latter. Especially among the GPS sources, in which some distortions in their radio structures are observed (see O'Dea 1998, and refs. therein), we distinguish a subgroup of *compact symmetric objects* (CSO, Wilkinson et al. 1994) known to be the smallest of AGNs with sizes below a few hundred pc.

The small sizes of the above mentioned groups are explained as a result of: (1) their young age; (2) confinement of the jets by the surrounding medium; (3) their episodic activity (e.g. O'Dea 1998; An and Baan 2012; O'Dea and Saikia 2021, and refs. therein). In the first scenario, these objects are believed to evolve into traditional FR I and FR II radio galaxies while in the second their further growth is blocked by the dense environments making their jets 'frustrated'. The third approach assumes that the radio sources have intermittent behavior of the nuclear activity on timescales of $10^4 - 10^5$ years driven by a variability in the accretion rate due to various instabilities within the accretion disc (e.g. Reynolds and Begelman 1997; Czerny et al. 2009; Janiuk and Czerny 2011). As shown by many authors, all these concepts can be true for some subsets of objects (see O'Dea and Saikia 2021).

1.3.1.3 Evolution

All the most known and studied classes of radio-loud and radio-quiet AGNs are shown in Figure 1.2. From their presentation on the radio luminosity vs. linear size plane, one can make an attempt at describing their evolutionary path, presented by O'Dea and Baum (1997), Kunert-Bajraszewska et al. (2010), and An and Baan (2012). Indeed, some of the CSO and GPS sources, for which strong jets will not meet any severe obstacles on their way, may transition to CSS and later to powerful FR II objects. Those, whose fate will be more harsh with denser environments, will still grow, but smaller and weaker, resulting in other, not so well defined as in case of FR II, morphologies and lower luminosities, becoming representatives of radio-weaker populations.

[5] Also relevant but not discussed, neither as extended nor compact sources, is a group of blazars. With a very small angle of the axis to the line of sight, blazars are excluded from the whole dissertation, as its focus is on AGNs with the extended radio emission with visible radio lobes (see especially Sections 1.3.3 and 1.4.2) and which is not the case for blazars.

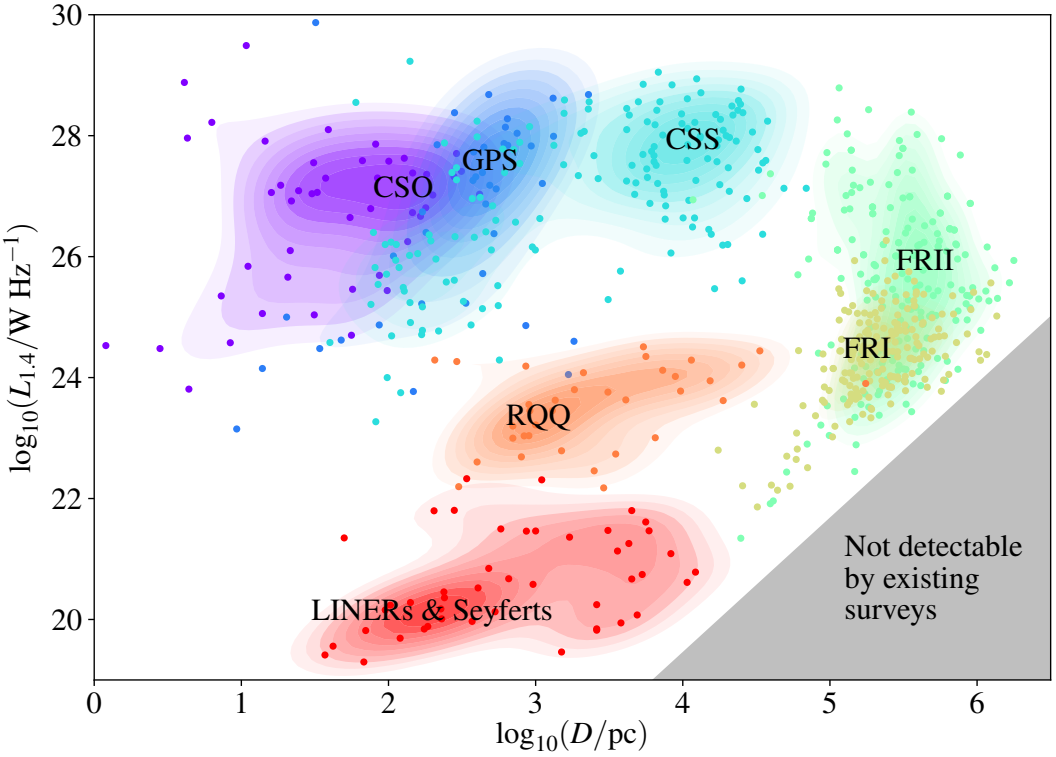

Figure 1.2: A representative radio luminosity vs. linear size plot for various classes of AGNs: CSO, GPS, and CSS with FR I and FR II objects being radio stronger emitters, compact and extended ones, respectively; LINERs & Seyferts in which radio emission is relatively weak (or even not detectable). Adopted from Hardcastle and Croston (2020).

1.3.2 Radio spectra

AGNs are not only very diverse with regards to their radio morphologies and sizes but also their radio spectra which cover a wide range of frequencies (from tens of MHz up to tens of GHz) and take various shapes (described via a single monotonic function or a composite of several functions; see below). A detailed analysis of them provides information about the properties of the source and its surroundings.

1.3.2.1 Synchrotron radiation

The main contribution to radiation in the radio domain is synchrotron emission which results from the motion of electrically charged particles (especially electrons and positrons[6]) moving at relativistic speeds (i.e. $\gamma_e \gg 1$, where γ_e is the Lorentz factor of an electron, $\gamma_e \propto E_e/m_e c^2$, with E_e and m_e being the electron energy and mass, consequently) in the presence of magnetic fields.

The frequency of the observed emission coming from a single electron is dependent on the electron energy and the magnetic field, B, as $\nu_e \propto \gamma_e^2 B$. The emitted power of such an electron is a function of the pitch angle (the angle between the electron velocity and magnetic field). Assuming an isotropic

[6]Protons (as well as other heavier charged particles), even though producing synchrotron radiation, are not taken here into account due to their inefficient emission. These particles, however, have to be considered while estimating the kinetic jet powers (see Section 1.4.2).

distribution of electron velocities, one can take an average over this angle and find that electrons with energy γ_e cool at average rates of $|\dot{\gamma_e}| \propto \gamma_e^2 U_B$, with U_B being the energy density of the magnetic field, $U_B \propto B^2$.

Then one can deduce that synchrotron spectra with spectral index α ($F_\nu \propto \nu^{-\alpha}$, where F_ν is the flux intensity at given frequency) can be reproduced by power-law energy distributions of electrons $N(\gamma_e) \propto \gamma_e^{-n}$ for $n = 2\alpha + 1$.

Even though synchrotron emission is usually discussed regarding radio observations, it can extend far beyond the radio domain, modifying the observed radiation in the infrared and optical regimes. Moreover its presence can also strongly contribute in the high energy part of the spectrum via synchrotron self-Compton (SSC) mechanism in which photons created in synchrotron emission are then Compton scattered to high energies by the very same electrons which produced them.

1.3.2.2 Observed shapes

The shape of the predicted synchrotron spectrum, i.e. the value of α or n and consequently its range, depends on a number of factors including, i.a. the opacity of the emitting region and the acceleration processes of the electrons (the latter being described in Section 1.4.1).

For extended radio sources, which are transparent to synchrotron emission down to $\nu < 100\,\mathrm{MHz}$, and with constant injection of energy into the electrons, the spectrum falls with $0.5 \lesssim \alpha \lesssim 1$ (see Figure 1 in Yuan et al. 2018). Once the acceleration processes are quenched, those with the highest energy are first to cool resulting in a high-frequency break and steepening spectra indicating that the radiating particles have aged the most (and providing information about the age of the source, typically of $10^7 - 10^8$ years for 'classical' doubles, see e.g. Konar et al. 2006; Bird et al. 2008)[7]. The maximum energy of particles is not well defined, depending on a number of assumptions of the models involved, but generally refers to a comparison of acceleration and cooling time scales ($t_{\mathrm{cool}} < t_{acc}$). In many extended radio sources power-law spectra show breaks at the lowest observed frequencies. They can be associated with synchrotron self-absorption or due to a break or low-energy cutoff in the distribution of the injected electrons. The more compact the radio source is, the higher the frequency the low-energy break is observed at (e.g. in GPS being located at GHz frequencies).

In reality the spectra we observe are not as straightforward as the description given above, since the astrophysical sources are characterized by non-uniform distributions of electron energy and magnetic fields with geometrically complex morphologies. The radio source can be optically transparent at all observed frequencies (e.g. as in 3C 123), self-absorption may occur at higher energies (e.g. at 20 GHz as in 3C 84), or the overall shape of the spectrum can become either flat or undulated, due to the superposition of multiple components becoming self-absorbed at different frequencies (e.g. as in 3C 454.3, all in Kellermann and Owen 1988).

Finally, the properties of radio spectra of compact sources (with regards to the AGNs' nuclei) also indicate the origin of radio emission. In the case of bigger emitters (above $\sim 100\,\mathrm{pc}$) not only powerful jets but also the SFRs can be considered (especially for radio weaker objects) while in smaller regions (below $\sim 100\,\mathrm{pc}$) the latter are excluded and the radio emission has to be produced in the more central regions, coming from the winds from the accretion disk, accretion disk coronas, or weak jets.

[7] Another way to estimate the age of the source is to divide its projected linear size by the speed of hotspots, the latter considered to move with $0.01 - 0.1\,c$ (e.g. Scheuer 1995).

1.3.3 Radio loudness

It has been already 40 years since AGNs were been divided into radio-loud (RL) and radio-quiet (RQ) sources. This division, introduced firstly by Strittmatter et al. (1980) and elaborated on by Kellermann et al. (1989), is based on the ratio of radio-to-optical monochromatic luminosities, originally measured at 5 GHz and in B-band, $R_{\rm K} \equiv L_{\nu_5}/L_{\nu_{\rm B}}$, and is named the *radio loudness* parameter. With the cutoff value of $R_{\rm K} = 10$, establishing the shape of the radio loudness distribution ($R_{\rm K} < 10$ for RQ and $R_{\rm K} > 10$ for RL objects, as it was given by Kellermann et al. 1989, see Figure 3 therein)[8], RL AGNs were found to represent $\sim 10\%$ of the total AGNs population.

This seemingly simple classification into RL and RQ AGNs has become increasingly problematic in the following years. Studies conducted by many researchers on radio loudness brought varying results leading to a clear division in the field – with some authors pushing for a strong bimodality in the distribution of radio loudness (e.g. Xu et al. 1999; Ivezić et al. 2002; Sikora et al. 2007) and others claiming a smooth distribution of this quantity (e.g. White et al. 2000; Cirasuolo et al. 2003a,b; Mahony et al. 2012; Singal et al. 2013).

A comprehensive discussion on the topic of the radio bimodality was carried out by Kratzer and Richards (2015) who discussed various factors affecting the shape of the radio loudness distribution. Limiting magnitudes in both the optical and radio domain artificially enhances or reduces the bimodality, strongly altering the number of radio-intermediate, RI, with radio loudness weaker than RL and stronger than RQ, sources (Ivezić et al. 2002). The removal of optical sources with no corresponding radio detection relates only to the RQ population, since the definition of a RL AGN is to be a strong radio emitter, and, furthermore, some of these non-detected RQ AGNs may be emitting in radio at levels too faint to be detected in previous large-scale radio surveys (White et al. 2007, 2015)[9]. The physical extent of the radio emission included in the analysis of radio loudness should be also considered as the radio-loudest AGNs most often manifest their strengths with impressive morphologies (see e.g. Rafter et al. 2009, 2011, who by using the same sample of AGNs, once with exclusion, later inclusion of the extended radio structures, showed that the bimodal distribution of the radio loudness is revealed in the second case). Finally the dependence on the redshift along with which the radio loudness increases should be also taken into account (e.g. Jiang et al. 2007; Singal et al. 2013).

In addition to the above, the radio loudness distribution can also be severely modified by BH mass and accretion rate which determine the nature of the accretion onto the AGN. Studies which account for these parameters were conducted by Ho (2002), Sikora et al. (2007), and Chiaberge and Marconi (2011). Using heterogeneous samples of AGNs, all authors found that the radio loudness increases with decreasing Eddington ratio and the highest radio loudness values are achieved by the more massive black holes.

The real question, however, is not so much about the radio loudness distribution solely as it is about the meaning of the parameter itself. In recent years many authors (Järvelä et al. 2017; Padovani 2017; Berton and Järvelä 2021) have been arguing that the radio loudness is inadequate and obsolete,

[8] Alternative ways to determine whether a source belongs to the RL or RQ group are, e.g.: taken as the ratio of radio to soft X-ray luminosity ($2-10$ keV, Terashima and Wilson 2003); or the ratio of radio to IR flux (at 24 μm, Appleton et al. 2004).

[9] Especially: National Radio Astronomy Observatory (NRAO) Very Large Array (VLA) Sky Survey (NVSS, Condon et al. 1998); Faint Images of the Radio Sky at Twenty-cm (FIRST, Becker et al. 1994); or Sydney University Molonglo Sky Survey (SUMSS, Bock et al. 1999; Mauch et al. 2003). All of those were used for research presented in this dissertation.

and that there is no astrophysical basis for using it to divide AGNs into RL, RI, and RQ classes. I state differently but only when relating the radio loudness parameter to the various mechanisms responsible for the radio emission in each of these groups.

As already listed (Section 1.3.1.2), the radio emission in the radio-quietest objects (the two lowest radio loudness decades[10]) is produced mainly by star-forming regions, accretion disk coronae and winds, and weak jets. The origin of such emission changes with higher values of radio loudness – in case of radio-intermediate objects the radio emission is produced by dissipation of AGN winds and/or jets and as for the radio-loud sources (the top two radio loudness decades) this emission is dominated by very strong jets. Only after considering what is the origin of the observed radio emission and treating radio-loud objects as sources in which powerful jets are being produced, the validity of radio loudness can be acknowledged.

The presence of strong jets is not very well recognized elsewhere than in the radio domain (despite the fact that RL AGNs still produce only a small fraction of their luminosity in the radio band, see Figure 1.1)[11]. Studies of spectral energy distributions of carefully chosen samples of AGNs (i.e. for which all the possible, above-mentioned, biases are eliminated) show that indeed, the only statistically significant difference between RL and RQ AGNs is the X-ray luminosity being a bit higher in RL group (Sanders et al. 1989; Gupta et al. 2018, 2020). This leaves radio observations as the most powerful tool in search for the most energetic jets.

1.4 Strong jet properties

As already stated in the previous sections, jets are fascinating phenomena, capable of remaining well collimated over several orders of magnitude in their length, leading to stunning morphologies, and being detectable over the whole electromagnetic spectrum. Occasionally, they can reach truly extreme powers, exceeding the accretion powers of AGNs in which they operate. In this section some of the properties of their strongest representatives are discussed.

1.4.1 Physical structure

The easiest starting point to analyze the structure of a jet is to consider a classical double, FR II object, with two-sided jets, as shown in Figure 1.3.

Propagating through and interacting with the ambient medium jets eventually result in an external shock wave, or more specifically – the termination shock stopping the incoming jet. The location of this impact corresponds to the jet's head, defined as the jet's front at which the forward and reverse shocks, separated by a contact discontinuity or a strongly unstable shear layer, take place (see e.g. Figure 1 in Smith et al. 1985). Matter entering the jet's head heats up and, due to the differential pressure of the jet and the surrounding medium, flows sideways, forming a cocoon around the jet. Matter outside of the cocoon piles up and compresses leading to a bow shock, as a result of which the ambient medium is accelerated and heated up.

[10] Here no specific value is provided as the radio loudness parameter can be calculated for very diverse frequencies (see Appendix A in Rusinek-Abarca and Sikora 2021).

[11] It should be noted that strong jets also contribute in X-ray radiation (Harris and Krawczynski 2006; Worrall 2009). However, in order to distinguish whether the observed high energy emission comes from jets or other components of an AGN requires much higher resolution than which is available nowadays.

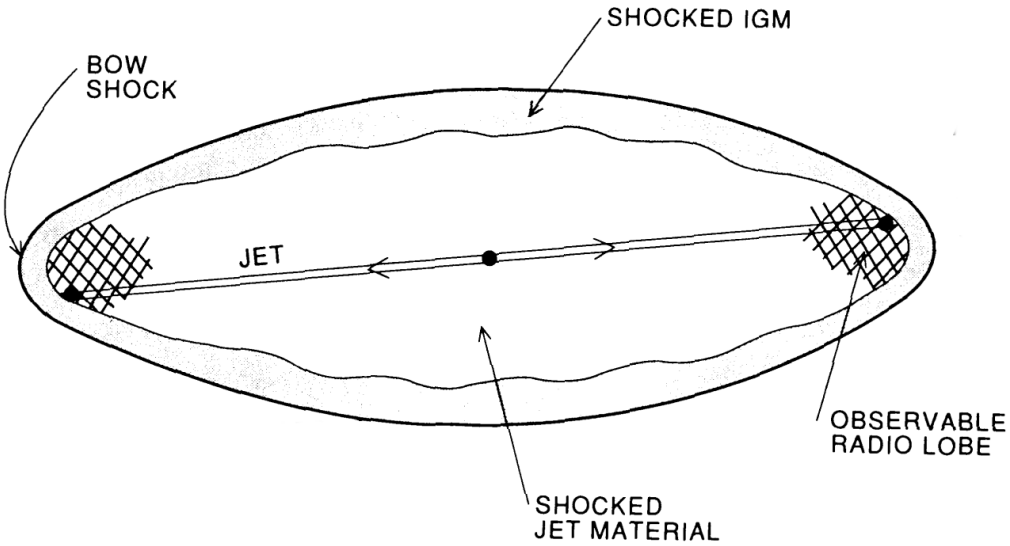

Figure 1.3: A simplified diagram of a cocoon, resulting from the activity of jets and their interaction with the external medium, surrounding the double AGN. Basic elements of its structure are presented. Adopted from Begelman and Cioffi (1989).

As seen in Figure 1.3, the cocoon formed in such a way consists of both the shocked jet material and the shocked intergalactic medium (IGM). Its shape is elongated with quite similar ratios of its width to its length, regardless of the physical size of the object (Kaiser and Alexander 1997). At its ends, where the termination shocks occur, the hotspots and radio lobes created by their transverse expansion with time are observed.

The jet-cocoon interaction is mutual, as the former creates the latter, and the latter defines the shape of the former, being collimated only when the pressure of the cocoon (set by its size and by the energy injected into it from the jet's head) is sufficiently high (Bromberg et al. 2011). The collimation of a jet can be a result of the ram pressure of external gas and presumably proceeds via reconfinement shocks.

Enclosed within the radio sources, particles undergo acceleration under a variety of mechanisms. Among these mechanisms we list the first and second order Fermi accelerations (Rieger et al. 2007). The former, known also as diffusive shock acceleration, describes the energy gain of charged particles via their traveling back and forth through the shock wave multiple times, while the latter, also known as stochastic acceleration, corresponds to the energy gain through particles scattering off of more massive and bigger elements in the form of magnetohydrodynamical (MHD) eddies. Fermi I occurs in various shocks, including terminal, reconfinment, and internal ones, where the internal shocks propagating with relativistic speeds are due to the collisions of components moving with diverse velocities within the jet (Spada et al. 2001). Fermi II takes place in a turbulent plasma resulting from various jet instabilities (Blandford et al. 2019) and in magnetic field reconnection layers, where the source of energy is linked to the magnetic topology rearrangement and partial magnetic field annihilation (Sironi and Spitkovsky 2014; Werner et al. 2018).

The structure of a jet can be even more inhomogeneous with more complicated lateral structure – consisting of an inner, narrow, and moving faster spine with an outer, wider, and slower sheath (e.g. Boccardi et al. 2016; Bruni et al. 2021; Janssen et al. 2021). Such a structure can be the result of nonuniform mass loading of a jet at its base (McKinney et al. 2012; Hawley et al. 2015) and nonuniform

distribution of the magnetic field across the jet.

Described here briefly the complexity of the jet structure is visible in the morphologies of AGNs (not only classical doubles but also their smaller cousins, i.e. CSOs) as less or more collinear continuous flows and/or compositions of individual bright knots and blobs (see e.g. Figure 1 in Godfrey et al. 2012 and in Hardcastle and Croston 2020). In addition to that, vast amounts of knowledge about the jet flows, their content and internal structures, as well as their interactions with the ambient medium, come from numerical simulations (see reviews by Davis and Tchekhovskoy 2020; Komissarov and Porth 2021, and refs. therein).

1.4.2 Powers

The primary relation used in estimating the jet power is its dependence on radio luminosity. Formulated by Willott et al. (1999), this relation refers to radio lobes from a classical double FR II type source (whose structure was described in previous Section, 1.4.1).

The time-averaged jet power estimated by Willott et al. (1999) is the ratio of the total energy content within the radio lobes and the age of the radio source. The minimum energy density required to produce the observed radio surface brightness accounts for the ion content, modifications of the assumed cylindrical geometry, and the lower spectrum cutoff. In the resulting jet power, the deviations from the minimum-energy condition (related to the energy density of the lobe magnetic field) and conversion of the jet energy into other forms (via the expansion work and bulk motions within a lobe), are included with the radiative losses being neglected. The latter is justified by authors who find that the total synchrotron energy radiated over the lifetimes of their studied sources is on the order of a few percent of the jet energy.

Deriving the age of a source through the dimensional analysis of a self-similar model for radio galaxy evolution (Falle 1991; Kaiser and Alexander 1997; Blundell et al. 1999) and by using considerations of radio observations (Scheuer 1995), the final formula for *jet kinetic power* is defined by Willott et al. (1999) as

$$P_j[\mathrm{erg\,s^{-1}}] = 3.43 \times 10^{20} (f)^{3/2} (L_{151}[\mathrm{W\,Hz^{-1}}])^{6/7}, \tag{1.2}$$

where L_{151} is the monochromatic radio luminosity at 151 MHz and f contains all unknown correction factors addressed in the model, with its value between 10 and 20 (see Godfrey and Shabala 2016, and refs. therein).

Shabala and Godfrey (2013) re-examined the relation brought by Willott et al. (1999) with special regard to the diverse sizes of AGNs and found a systematic shift in jet power estimations. As the reason for this discrepancy, they point precisely to the various loss processes, stated to be negligible by Willott et al. (1999). Among the loss mechanisms they list: synchrotron radiation losses; adiabatic expansion of the volume element (in which the electrons were last accelerated); and upscattering of cosmic microwave background (CMB) photons via the inverse Compton process. All those modify the electron energy spectrum and, consequently, the age of the source, affecting the source size as well as the radio luminosity. Expressing the relation between jet power and source size, D, as

$$P_j[\mathrm{erg\,s^{-1}}] = 1.5 \times 10^{43} (L_{151}[\mathrm{W\,Hz^{-1}}]/10^{27})^{0.8} (1+z) (D\,[\mathrm{kpc}])^{0.58}, \tag{1.3}$$

Shabala and Godfrey (2013) demonstrate the importance of the above-mentioned issues, especially in the smallest (~ 10 kpc) and biggest ($\gtrsim 500$ kpc) of AGNs for which the jet powers are over- and

underestimated, accordingly. In light of their results, the Equation 1.2 remains correct[12] when being used for AGNs of typical sizes (see Section 1.3.1).

Other methods for jet power estimations, not exploited more closely in this dissertation, make use of X-ray cavities (Cavagnolo et al. 2010) or hotspot parameters (Godfrey and Shabala 2013), and also include FR I (Godfrey and Shabala 2016).

With regard to the relations found by Willott et al. (1999) and Shabala and Godfrey (2013), it is evident that they can be used only for a minority of AGNs, i.e. objects in which double radio lobes belonging to the FR II class are observed. As shown by many authors, the jet powers calculated for those sources reach very high values, up to even $10^{47}\,\mathrm{erg\,s^{-1}}$ (Punsly 2007; Fernandes et al. 2011; Sikora et al. 2013; van Velzen and Falcke 2013; Inoue et al. 2017; Rusinek et al. 2017), approaching, or, in some cases, even exceeding their associated accretion luminosities by an order of magnitude (see Chapter 2 and refs. therein). Such observations indicate a specific jet production scenario, which is discussed below.

1.4.3 Production efficiency

By comparing the jet powers to the accretion powers, we obtain the *jet production efficiency*,

$$\eta_j \equiv P_j/(\dot{M}c^2), \tag{1.4}$$

which gives us an indirect diagnostic of the physical conditions behind jet launching in AGNs, i.e. the jet formation process and the source of the jet power. The jet production efficiency plays also an important role towards an understanding of the AGN feedback (e.g. Allen et al. 2006; McNamara and Nulsen 2007; Fabian 2012), the cosmological evolution, and the growth of massive BHs (e.g. Fanidakis et al. 2011; Volonteri et al. 2013).

As shown in Section 1.4.2, the jet power can be derived from the radio luminosities of radio lobes, while the accretion power can be calculated applying the bolometric corrections to the observed monochromatic luminosities in optical or IR spectral bands (Richards et al. 2006). Hence, the jet production efficiency refers in fact to the ratio of radio to optical luminosity being the radio loudness ($R = L_r/L_o$ with L_r and L_o being the monochromatic radio and optical luminosities, respectively; see Appendix A in Rusinek-Abarca and Sikora 2021).

From multiannual studies of radio loudness, we know that the values of radio loudness not only span over 5 orders of magnitude (e.g. Kellermann et al. 1989; White et al. 2000; Ivezić et al. 2002; Sikora et al. 2007; Singal et al. 2013; Rusinek et al. 2020, and many more) but also reveal a bimodal distribution (see Section 1.3.3 and Chapter 3). This implies a large diversity in jet production efficiency and raises the question of whether the observed radio bimodality corresponds to some threshold for the production of powerful jets by a certain specific launching mechanism, or whether the same mechanism is responsible for the production of all jets (e.g. Sikora et al. 2007).

There are a few scenarios standing behind the production of jets.

- The mechanism suggested by Blandford and Payne (1982, BP) assumes the creation of jets by recovering the momentum and energy from a rotating accretion disk. Such a process takes place

[12] In a statistical sense. For individual sources it may be inadequate due to the different matter content, the density of the environment into which the lobes are inflated (Hardcastle and Krause 2013), and issues discussed by Shabala and Godfrey (2013).

if the poloidal component of the magnetic field is inclined to the disk rotation axis at angles larger than $60°$. Near the surface of a disk the outflow is initiated by the gas pressure in the hot, magnetically dominated disk corona and accelerated by the centrifugal forces acting on the matter moving along the magnetic field lines.

- Another approach was given by Blandford and Znajek (1977, BZ) who postulated that the momentum and energy are extracted directly from the black hole. In this model the magnetic field penetrates the rotating black hole in result of which it starts to rotate as well, accelerating the charged particles along the axis of its rotation, and therefore – creating jets.

In both cases, the large scale magnetic field is a crucial ingredient in jet formation. The cause of the rotation of the poloidal magnetic field lines (being the keplerian rotation of the disc in BP, and inertial frame dragging by the BH in BZ) leads to the importance of another factor, namely – BH spin (a).

The dependence of jet power on BH spin appears in the BZ mechanism (which is the favored scenario for the production of relativistic jets) in the form of

$$P_{\rm BZ} \propto a^2\, \Phi^2_{\rm BH}, \tag{1.5}$$

where $\Phi_{\rm BH}$ is the magnetic flux confined on the BH by the accretion flow. Thus, it seems that the diversity of the jet powers can be determined equally by both of these factors.

In reality, the first possibility, i.e. the spread of the BH spins leading to a spread in jet powers, known as the *spin paradigm* (Sikora et al. 2007; Fanidakis et al. 2011; Schulze et al. 2017) does not provide a big enough range of these values where the required BH spins in RQ AGNs should be smaller than 0.03, the estimated values by using the 'Soltan argument' are predicted to be ~ 0.6 (Soltan 1982; Elvis et al. 2002; Lacy et al. 2015), and the actual values are large (Reynolds 2019, and refs. therein). This puts a focus on the second parameter which is related to the *magnetic flux paradigm*.

Before examining exactly what the magnetic flux paradigm means and whether it solves the issue of a large diversity in the jet production efficiencies (spread over about two decades, van Velzen and Falcke 2013; Inoue et al. 2017; Rusinek et al. 2017), a specific model of an accretion disk should be introduced. This model explains the highest of jet production efficiencies and involves rapidly rotating black holes with large magnetic fluxes threaded by them. In the most extreme cases the magnetic fields (their poloidal components) dynamically dominate the innermost portions of the accretion flows and the resulting magnetic pressure restricts matter from falling onto the black hole, leading to the *magnetically arrested disk* (MAD) state (Narayan et al. 2003) thoroughly tested in numerical simulations (Igumenshchev 2008; Punsly et al. 2009; Tchekhovskoy et al. 2011; McKinney et al. 2012). In this scenario jet powers can be even up to tens of times stronger than those obtained in the 'classical' BZ mechanism.

In case of MAD, an additional factor on which the jet power depends appears being the geometrical thickness of the accretion flow (H/R),

$$P_{\rm MAD} \propto a^2\, \Phi^2_{\rm BH}\, (H/R)^k, \tag{1.6}$$

where according to Avara et al. (2016) $k \simeq 2$, while Davis and Tchekhovskoy (2020) reports $k \sim 1$. This implies that finding the most powerful jets in AGNs with standard accretion disks (in which $H/R < 0.1$) is rather unlikely.

As shown in the following Chapters and Papers presented therein (Rusinek et al. 2017 in Chapter I, Rusinek et al. 2020 in Chapter II, and Rusinek-Abarca and Sikora 2021 in Chapter III) MAD most probably operates in some of the AGNs with moderate accretion rate. The provision of having strong enough magnetic fields needed for MAD to take place is however far from trivial suggesting some specific conditions that have to be fulfilled and, consequently, that the classification of AGNs based on the radio loudness parameter corresponds to the division of AGNs into those with and without MAD.

2 Paper I: On the efficiency of jet production in FR II radio galaxies and quasars

In Rusinek et al. (2017) we decided on analyzing the jet production efficiencies for four heterogeneous samples of AGNs. Each of these sets has been selected in a different way, and all of them together cover wide range of redshifts (from the local Universe up to $z = 3.5$), black hole masses ($10^6 M_\odot \lesssim M_{\rm BH} \lesssim 10^{10} M_\odot$), and bolometric luminosities (estimated from broad Hβ emission line, B-band, or monochromatic luminosity at 3000 Å or in mid-IR at 12 μm). Furthermore, sources within these samples have smaller and larger accretion rates and represent both narrow and broad emission line radio galaxies (NLRGs, BLRGs) as well as quasars. The unifying feature for all the objects was the presence of double radio lobes of FR II type for which the calculations of the jet powers were obtained by using the calorimetry of these lobes (following Willott et al. 1999).

The results obtained in this paper show a clear decrease in the jet production efficiency ($\sim P_j/L_{\rm bol}$) at higher accretion rates (see Figure 4 therein) which is consistent with the trend found earlier by Sikora et al. (2007) for other radio-loud AGNs. This outcome cannot be justified by a transition from a radiatively inefficient, optically thin, but geometrically thick, accretion disk to a standard, optically thick and geometrically thin disk as the vast majority of AGNs we gathered constitute objects accreting at moderate accretion rates ($0.01 \lesssim \lambda_{\rm Edd} \lesssim 0.30$). Furthermore, the jet powers in some of these AGNs exceed their associated accretion powers (while assuming the radiative efficiency of an accretion disk as $\epsilon_d = 0.1$).

In order to explain our findings we consider the MAD scenario, but assume geometrically thicker accretion disks than standard theory predicts – to agree with jet production efficiencies we obtained.

Monthly Notices
of the
ROYAL ASTRONOMICAL SOCIETY

MNRAS **466,** 2294–2301 (2017)
Advance Access publication 2016 December 23

doi:10.1093/mnras/stw3330

On the efficiency of jet production in FR II radio galaxies and quasars

Katarzyna Rusinek,[1,2⋆] Marek Sikora,[2⋆] Dorota Kozieł-Wierzbowska[3] and Leith Godfrey[4]

[1]*Toruń Centre for Astronomy, Faculty of Physics, Astronomy and Informatics, Nicolaus Copernicus University, Grudziądzka 5, PL-87-100 Toruń, Poland*
[2]*Nicolaus Copernicus Astronomical Center, Polish Academy of Sciences, Bartycka 18, PL-00-716 Warsaw, Poland*
[3]*Astronomical Observatory, Jagiellonian University, ul. Orla, PL-30-244 Kraków, Poland*
[4]*ASTRON, The Netherlands Institute for Radio Astronomy, Postbus 2, NL-7990 AA, Dwingeloo, the Netherlands*

Accepted 2016 December 19. Received 2016 November 18; in original form 2016 August 16

ABSTRACT

Jet powers in many radio galaxies with extended radio structures appear to exceed their associated accretion luminosities. In systems with very low accretion rates, this is likely due to the very low accretion luminosities resulting from radiatively inefficient accretion flows. In systems with high accretion rates, the accretion flows are expected to be radiatively efficient, and the production of such powerful jets may require an accretion scenario, which involves magnetically arrested discs (MADs). However, numerical simulations of the MAD scenario indicate that jet production efficiency is large only for geometrically thick accretion flows and scales roughly with $(H/R)^2$, where H is the disc height and R is the distance from the black hole. Using samples of FR II radio galaxies and quasars accreting at moderate accretion rates, we show that their jets are much more powerful than predicted by the MAD scenario. We discuss possible origins of this discrepancy, suggesting that it can be related to approximations adopted in magnetohydrodynamic simulations to treat optically thick accretion flow within the MAD zone, or may indicate that accretion discs are geometrically thicker than the standard theory predicts.

Key words: acceleration of particles – radiation mechanisms: non-thermal – galaxies: jets.

1 INTRODUCTION

The radio loudness of a quasar is defined as the ratio of radio luminosity (typically at 5 GHz) to optical luminosity (typically in the B band). The radio luminosity of a quasar is related to jet power $P_{\rm j}$, while the optical luminosity is related to accretion power $\dot{M}c^2$, where $\dot{M}$ is the accretion rate. For this reason, the radio loudness is a proxy for the jet production efficiency defined to be $\eta_{\rm j} \equiv P_{\rm j}/(\dot{M}c^2)$.

The first quasars were discovered following the identification of bright radio sources with point-like optical sources. However, not all quasars have such strong radio emission: In fact, the majority of quasars have been found to be radio-quiet (Kellermann et al. 1989). Present-day radio telescopes are able to detect the faint radio emission of radio-quiet quasars (e.g. White et al. 2015, and refs. therein), however, their radio loudness is up to 3–4 orders of magnitude lower than that of the radio loudest active galactic nuclei (AGNs; e.g. White et al. 2007). This indicates a large diversity of jet production efficiency.

There have been several scenarios proposed to explain such a diversity of jet production efficiency. The two most popular scenarios are the so-called 'spin paradigm' (Wilson & Colbert 1995; Sikora, Stawarz & Lasota 2007; Garofalo, Evans & Sambruna 2010; Fanidakis et al. 2011) and the intermittency of jet production (Livio, Pringle & King 2003; Körding, Jester & Fender 2006). According to the spin paradigm, the jets are powered by rotating black holes (BHs) and the jet production efficiency, $\eta_{\rm j}$, is assumed to depend predominantly on the value of the BH spin. The drawback of this assumption is that it implies much lower values of BH spin in radio-quiet AGN than indicated by using 'Sołtan argument' (Sołtan 1982; Elvis, Risaliti & Zamorani 2002; Lacy et al. 2015) and predicted by numerical simulations of cosmological evolution of supermassive BHs (Volonteri et al. 2013). The intermittent jet production scenario involves transitions between two accretion modes: one associated with a standard viscous accretion discs and another associated with accretion being driven by magnetohydrodynamic (MHD) winds. While this scenario may be attractive to explain intermittent jet activity observed directly in GRS 1915+105 (Livio et al. 2003) and the overabundance of compact radio galaxies in flux-limited samples (Reynolds & Begelman 1997), such accretion mode transitions are rather difficult to reconcile with the existence of 10^7–10^8 yr

⋆ E-mail: krusinek@camk.edu.pl (KR); sikora@camk.edu.pl (MS)

old jets observed in FR II radio sources (Blundell, Rawlings & Willott 1999; Bird, Martini & Kaiser 2008; O'Dea et al. 2009; Antognini, Bird & Martini 2012) and also with the lack of evidence for remnant radio lobes around radio-quiet quasars. Furthermore, the 'transition' models predict bimodal distribution of radio loudness (e.g. Nipoti, Blundell & Binney 2005) and this is observed only if other-than-FR II sources are ignored (Lu et al. 2007; Rafter, Crenshaw & Wiita 2011).

Jet production theories are challenged not only by the large spread of radio loudness, but also by the fact that the jet powers in many radio galaxies reach values comparable to the accretion powers (Rawlings & Saunders 1991; Punsly 2007; Fernandes et al. 2011; Sikora et al. 2013). In order to produce jets with such high efficiency in the Blandford–Znajek mechanism (Blandford & Znajek 1977), BHs are required not only to be spinning very fast but also to be threaded by a very large magnetic flux. The required level of magnetic flux threading the BH can only be maintained if it is confined by the ram pressure of the accretion flow. The latter condition implies a magnetically arrested disc (MAD) scenario, in which the innermost portion of the accretion flow is dynamically dominated by the poloidal magnetic field and accretion proceeds via interchange instabilities (Narayan, Igumenshchev & Abramowicz 2003; Igumenshchev 2008; Punsly, Igumenshchev & Hirose 2009; Tchekhovskoy, Narayan & McKinney 2011; McKinney, Tchekhovskoy & Blandford 2012).

Recent studies of the jet powers in a sample of radio-selected FR II quasars by van Velzen & Falcke (2013, see also van Velzen, Falcke & Körding 2015) show that the median jet production efficiency in these objects is 10 times lower than maximal predicted by the MAD scenario. Such low jet production efficiency in the MAD scenario would require very low median BH spin and this led the authors to conclude that jet production in these systems does not involve MAD. However, the MAD models predict that the jet production efficiency depends not only on the BH spin, but also has a very strong dependence on the geometrical thickness of the accretion flow. According to Avara, McKinney & Reynolds (2016), the jet production efficiency at moderate accretion rates, where standard theory predicts very thin accretion discs, should be hundreds of times lower than that obtained from geometrically thick accretion discs. Therefore, due to the strong dependence of jet production efficiency on disc thickness, the problem is actually the opposite of the one claimed by van Velzen & Falcke, and can be expressed by the following question: how is it possible to obtain such high jet production efficiency in these radio-loud AGN, despite their apparently moderate accretion rates, and therefore geometrically thin accretion discs.

In this work, we demonstrate the presence of high-η_j objects at moderate accretion rates, by considering the dependence of P_j/L_d on the Eddington ratio L_d/L_{Edd} (where L_d is the accretion luminosity and L_{Edd} is the Eddington luminosity) for the following radio-loud AGN samples: $z < 0.4$ FR II narrow-line radio galaxies (NLRGs; Sikora et al. 2013) in Section 2.2; FR II quasars (van Velzen & Falcke 2013) in Section 2.3; $0.9 < z < 1.1$ NLRGs (Fernandes et al. 2011) in Section 2.4; and a sample of broad-line radio galaxies plus radio-loud quasars (BLRG+RLQ) compiled by Sikora et al. (2007) in Section 2.5. The theoretical implications of the presented distributions – with particular reference to the applicability of the MAD scenario – are discussed in Section 3 and summarized in Section 4.

We have adopted the Lambda cold dark matter (ΛCDM) cosmology, with $H_0 = 70\,\mathrm{km\,s^{-1}}$, $\Omega_m = 0.3$ and $\Omega_\Lambda = 0.7$.

2 JET PRODUCTION EFFICIENCY

2.1 Overview

In order to adequately assess the distribution of radio galaxies and quasars in the P_j/L_d–L_d/L_{Edd} plane, we have combined four different samples of radio galaxies and quasars. In the following, we describe each of these samples, and the methods used to estimate P_j, L_d and L_{Edd} from the available radio and optical data.

2.2 FR II NLRGs at $z < 0.4$

This sample contains 207 FR II NLRGs extracted from the sample of $z < 0.4$ radio galaxies with extended radio structure selected by Sikora et al. (2013). The objects are taken from Cambridge catalogues and matched with the SDSS (Sloan Digital Sky Survey), FIRST (Faint Images of the Radio Sky at Twenty Centimeters) and NVSS (National Radio Astronomy Observatory (NRAO) Very Large Array (VLA) Sky Survey) catalogues. The sample is presented in Table A1 (Appendix A, as subsequent tables), where additionally to data presented in Sikora et al. we list values of: disc luminosities – L_d; jet powers – P_j; their ratio – P_j/L_d; and the Eddington ratio – $\lambda_{Edd} \equiv L_d/L_{Edd}$. The disc luminosities L_d are calculated using the H α emission line luminosity, $L_{H\alpha}$, which is available for 152 sources, adopting the conversion formula

$$L_d[\mathrm{erg\,s^{-1}}] = 7.8 \times 10^{36} L_{H\alpha}[\mathrm{L_\odot}] \quad (1)$$

(Netzer 2009), which gives the disc luminosity with uncertainty of 0.3 dex. The jet powers are calculated using the 1.4 GHz monochromatic radio luminosity, $L_{1.4}$, along with the scaling relation of Willott et al. (1999):

$$P_j[\mathrm{erg\,s^{-1}}] = 5.0 \times 10^{22} (f/10)^{3/2} (L_{1.4}[\mathrm{W\,Hz^{-1}}])^{6/7}\,, \quad (2)$$

where we have assumed the radio spectral index between 151 MHz and 1.4 GHz is $\alpha_r = 0.8$ (using the convention $F_\nu \propto \nu^{-\alpha}$). The formula is based on calorimetry of radio lobes and f is the parameter accounting for errors in the model assumptions. According to Blundell & Rawlings (2000), the value of f is between 10 and 20. More secure determination of jet power in FR II radio sources is based on the model of hotspots (Godfrey & Shabala 2013). Unfortunately hotspots are often very weak or not visible. However, comparing jet powers of luminous FR II sources obtained using the hotspots and radio lobe calorimetry allowed us to calibrate the Willott et al. formula. For luminous FR II sources, this gives $f \simeq 10$ and uncertainty of P_j calculated using equation (2) is about 0.3 dex.

The distribution of P_j/L_d for this sample is plotted in Fig. 1. For many objects $P_j/L_d > 10$, which for disc radiation efficiency $\epsilon_d \equiv L_d/(\dot{M}c^2) = 0.1$ implies jet production efficiency $\eta_j \equiv \epsilon_d(P_j/L_d) > 1$, where $\dot{M}$ is the accretion rate.

In Fig. 2, we plot the ratio P_j/L_d against the Eddington scaled accretion luminosity, or Eddington ratio, $\lambda_{Edd} \equiv L_d/L_{Edd}$. As can be seen in this figure, the extreme efficiencies with $P_j/L_d > 10$ and hence $\eta_j > 1$ are possessed only by radio galaxies with very low Eddington ratios, which are therefore presumably operating in the radiatively inefficient accretion regime. The median value of P_j/L_d at moderate accretion rates corresponding to $\lambda_{Edd} > 0.003$ is 2.65, implying a modest jet production efficiency of order $\eta_j \sim 0.265\,(\epsilon_d/0.1)$. Marked in the lower left corner of Fig. 2 are the uncertainties for P_j/L_d and λ_{Edd}. These are calculated based on the uncertainties for P_j, L_d and M_{BH} and noting that standard deviations of ratios (and products) of two independently determined quantities, $\sigma_{X/Y} = \sqrt{\sigma_X^2 + \sigma_Y^2}$. The uncertainties of P_j, L_d and M_{BH} are

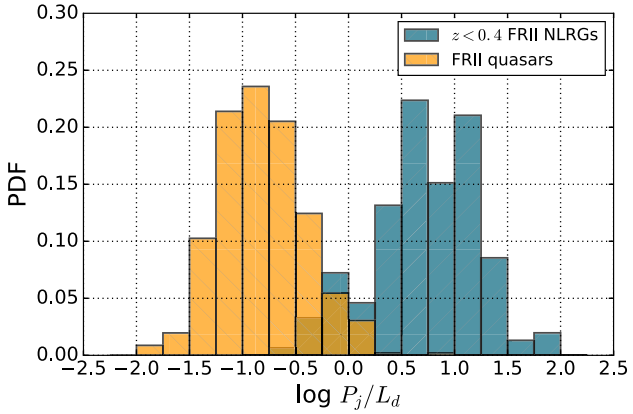

Figure 1. The distribution of the jet efficiency P_j/L_d for $z < 0.4$ FR II NLRGs (152 sources) and FR II quasars (458 sources) samples is represented by blue and orange colours, respectively. The histogram has been normalized so that the sum of the bin heights is equal to unity.

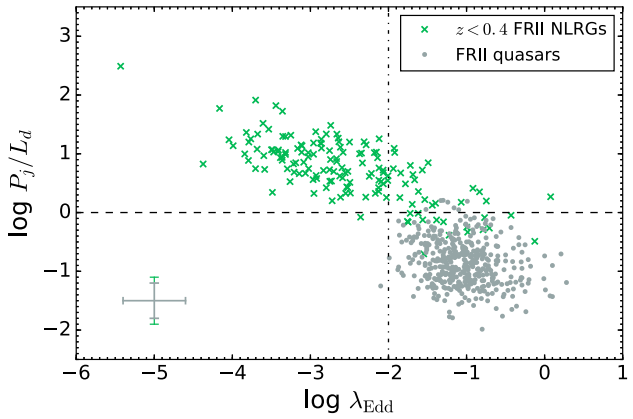

Figure 2. The dependence of P_j/L_d ratio on the Eddington ratio λ_{Edd}. The $z < 0.4$ FR II NLRGs sample is shown by green crosses while grey dots are for FR II quasars sample (here 414 sources). Uncertainties of P_j/L_d and λ_{Edd} (described in the respective subsections) are presented in the lower left corner. The horizontal dashed line corresponds to the level where P_j equals L_d and the vertical dot–dashed line marks an approximate value of the Eddington ratio at which the accretion mode is changing from the radiatively inefficient (left side) to the radiatively efficient (right side; Best & Heckman 2012; Mingo et al. 2014). An apparent anticorrelation exists between these two plotted properties.

estimated to be approximately 0.3 dex (for the latter see Tremaine et al. 2002), resulting in 0.4 dex uncertainties of P_j/L_d and of $\lambda_{Edd} \propto L_d/M_{BH}$.

2.3 The FR II quasar sample

The FR II quasar sample used in this work was first obtained by van Velzen et al. (2015) based on the selection of double-lobed radio sources from the FIRST survey catalogue, and cross-matching with SDSS quasars. In Table A2, we present the relevant data for this sample, including the monochromatic rest-frame luminosity at 1.4 GHz, $L_{1.4}$, and if available, masses of BHs and Eddington ratios. The radio luminosities were calculated based on the 1.4 GHz lobe flux densities given by van Velzen et al., and k-corrected assuming radio spectral index $\alpha_r = 0.85$, along with standard ΛCDM cosmology, as specified in Section 1. The jet power P_j was calculated using equation (2). The BH masses and Eddington ratios, when available,

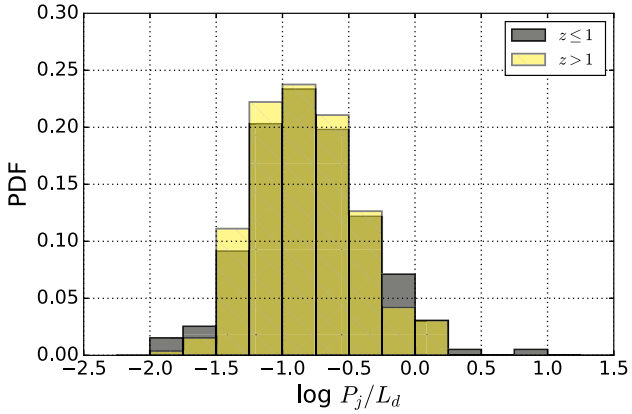

Figure 3. The division of FR II quasars sample (458 sources as it is in Fig. 1) based on the boundary value of redshift $z = 1$. No discrepancy between sources with lower (197 objects marked by grey colour) and higher (261 objects represented by yellow colour) values is present.

were taken from Shen et al. (2011) thereby reducing the sample from 458 to 414 sources.

The P_j/L_d histogram and dependence of P_j/L_d on λ_{Edd} for this sample of FR II quasars are plotted together with $z < 0.4$ FR II NLRGs in Figs 1 and 2. As can be seen, the median jet production efficiency in FR II quasars is $\sim 0.02(\epsilon_d/0.1)$, i.e. $\sim$13 times lower than in the $\lambda_{Edd} > 0.003$ subsample of $z < 0.4$ FR II NLRGs.

In Fig. 3, we show the P_j/L_d distributions for the FR II quasars divided into two subsamples, with $z > 1$ and $z < 1$. The fact that the P_j/L_d distributions are very similar for the high- and low-redshift subsamples indicates that the difference in median η_j between FR II quasars and $z < 0.4$ NLRGs at $\lambda_{Edd} > 0.01$ is not caused by cosmological evolution of jet production efficiency, but rather by the different flux limits and procedures to select the two samples.

Uncertainties of L_d luminosities derived in Shen et al. (2011) using bolometric corrections to optical luminosity at 5100 Å are about 0.1 dex (Richards et al. 2006), while uncertainties of M_{BH} derived by Shen et al. using virial estimators are $\sim$0.4 dex. With these uncertainties and 0.3 dex uncertainty of P_j, the uncertainties of P_j/L_d and λ_{Edd} for FR II quasars are $\sim$0.3 and 0.4 dex, respectively. They are marked, together with uncertainties for the $z < 0.4$ FR II NLRGs sample, in the lower left corner of Fig. 2.

2.4 $0.9 < z < 1.1$ sample of NLRGs

As we can see from Fig. 2, the sample of $z < 0.4$ FR II NLRGs is poorly represented at $\log \lambda_{Edd} > -1.5$. This is primarily due to a low number of high accretion rate AGNs with very massive BHs in the local Universe. In order to verify how much this incompletness affects the average jet production efficiency in FR II RGs, we extend the FR II NLRGs sample by adding 27 $z \sim 1$ NLRGs selected in $0.9 < z < 1.1$ taken from Falder et al. (2010). With a few exceptions, they all have FR II radio morphologies. The relevant data for this sample are presented in Table A3, which are taken from table 1 in Fernandes et al. (2011), as well as table 3 in Fernandes et al. (2015). As before, P_j is calculated based on equation (2). The disc luminosity for this sample has been calculated using mid-IR data from *Spitzer Space Telescope* at wavelength 12 μm along with the following scaling relation: $L_d = 8.5 \times [\nu L_\nu]$ (Richards et al. 2006). BH masses have been derived using relation between the BH and bulge masses (Häring & Rix 2004). Their uncertainty is $\sim$0.3 dex. Combining it with uncertainty of disc luminosities, $\sim$0.2 dex, and

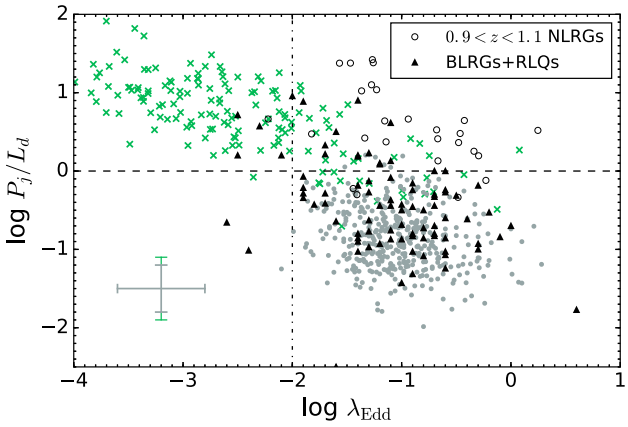

Figure 4. The same plot as in Fig. 2 with two added samples: $0.9 < z < 1.1$ NLRGs as empty circles (27 sources); BLRG+RLQ as black triangles (87 sources). Uncertainties of P_j/L_d and λ_{Edd} for all four samples are presented in the lower left corner (their values for $z < 0.4$ FR II NLRGs and $0.9 < z < 1.1$ NLRGs and for FR II quasars and BLRG+RLQ are equal).

jet powers, 0.3 dex, gives uncertainties of P_j/L_d and of λ_{Edd}, both about 0.4 dex.

The sample is plotted in Fig. 4. The median P_j/L_d is similar to that of the $z < 0.4$ FR II NLRGs sample for $\lambda_{Edd} > 0.003$ and uncertainties of the $z \sim 1$ NLRGs sample are the same. They are marked in the lower left corner.

2.5 A BLRG+RLQ sample

The incompletness of SDSS quasars at moderate accretion rates (Kelly & Shen 2013) may introduce a bias in our analysis of FR II quasars due to underrepresentation of such objects, particularly at $\lambda_{Edd} < 0.03$. In order to verify whether the incompleteness of SDSS quasars at moderate accretion rates can significantly affect the average value of η_j of our sample, we complete our studies of jet production efficiency by adding a sample of BLRGs co-selected with low-redshift RLQs. The sample is comprised of radio-loud broad-line AGN with redshift $z < 0.4$, selected from Véron-Cetty & Véron (1989) by Eracleous & Halpern (1994, 2003) and used by Sikora et al. (2007) to study radio loudness of these objects. Using a formal, luminosity related definition of quasars, these objects were divided by Sikora et al. into two subsamples: BLRG and RLQ. The BLRG+RLQ sample data are listed in Table A4(a) and A4(b). As with the previous samples, P_j is calculated using equation (2), but in this case, we have had to extrapolate flux densities at 5 to 1.4 GHz using a radio spectral index $\alpha_r = 0.8$. The disc luminosity is calculated based on the *B* band and using the bolometric correction from Richards et al. (2006). Its uncertainty is ∼0.1 dex. BH masses have been derived using virial estimators (e.g. Woo & Urry 2002), and uncertainties of such estimators are ∼0.4 dex. With these uncertainties and 0.3 dex uncertainty of P_j, the uncertainties of P_j/L_d and λ_{Edd} are ∼0.3 and 0.4 dex, respectively. They are marked in Fig. 4 in the lower left corner together with uncertainties for the $z \sim 1$ NLRGs sample. As we can see in Fig. 4, despite these large uncertainties, the BLRG+RLQ sample is fully consistent with the sample of FR II quasars from van Velzen et al.

3 DISCUSSION

The applicability of the MAD scenario for the production of powerful AGN jets was recently investigated using 3D general-relativistic, magnetohydrodynamic simulations (Igumenshchev 2008; Punsly et al. 2009; Tchekhovskoy et al. 2011; McKinney et al. 2012). These studies demonstrated that MAD have the ability to launch jets with a power comparable to the accretion power, as is required to explain the energetics of radio lobes in the radio-loud FR II sources (Rawlings & Saunders 1991; Punsly 2007; Fernandes et al. 2011; Sikora et al. 2013).

However, the MAD simulations indicate that there is a clear trend of decreasing efficiency of relativistic jet production with decreasing geometrical thickness of the accretion flow. This trend was found in the case of 'non-radiative' models with disc thickness $H/R = 1.0$–0.3 (Tchekhovskoy et al. 2011; McKinney et al. 2012), and was explained as being due to loading boundary layers of the Blandford–Znajek outflow with mass to such a level that these outflows do not gain relativistic speeds. More recently, simulations of the MAD scenario were extended by Avara et al. (2016) to cover the case of the optically thick accretion flows, with $H/R \sim 0.1$. Combining the results of these simulations with results obtained for non-radiative and geometrically thicker accretion flows they derived the following empirical formula describing a dependence of the jet production efficiency η_j on geometrical thickness and dimensionless BH spin *a*:

$$\eta_j \simeq 4a^2 \left(1 + \frac{0.3a}{1 + 2(H/R)^4}\right)^2 (H/R)^2, \quad (3)$$

which for $H/R \ll 1$ gives $\eta_j \sim 4a^2(1 + 0.3a)^2(H/R)^2$. According to the standard accretion disc model (Novikov & Thorne 1973; Laor & Netzer 1989), maximal thickness of a disc accreting on to a BH with $a \sim 1$ and producing radiation at a rate of $\lambda_{Edd} \sim 0.1$ is $H/R \sim 0.04$. For these parameters, the above formula gives $\eta_j \simeq 0.01$. This is a factor of 2 less than the median value of the FR II quasars sample and by a factor of 20 less than its upper bound in the P_j/L_d versus λ_{Edd} plots. Noting ∼0.4 dex uncertainties of P_j/L_d, it is rather unlikely that above discrepancy is resulting from errors of P_j and/or L_d. Then we can envisage two possible solutions of this discrepancy. One is that because MHD simulations of radiative, optically thick accretion flows are still not fully self-consistent, the extrapolation of dependence of η_j on H/R indicated by non-radiative accretion flows down to the regime of optically thick accretion flows can be quantitatively inaccurate. Another possibility is that optically thick accretion discs are much thicker than predicted by the standard accretion disc theory. The disc can be thicker in presence of strong toroidal magnetic fields (e.g. Begelman & Pringle 2007; Sądowski 2016), or can be accompanied by heavy, viscously driven corona (Begelman, Armitage & Reynolds 2015; Różańska et al. 2015). Furthermore, within the MAD zone the disc is radially balanced against gravity by dynamically dominated poloidal magnetic fields and, therefore, even if outside the MAD zone the disc is geometrically thin, within the MAD zone it can become sub-Keplerian and thicker than the standard one. The suspicion that approximations used by Avara et al. to treat in MHD simulations the optically thick disc are inaccurate is also supported by the fact, that they predict larger radiative efficiency of MADs than of standard accretion discs, whilst observations indicate the opposite: radio-quiet quasars have been found to be more luminous in UV than RLQs (Punsly et al. 2016, and refs. therein).

Obviously, not all RLQs have FR II radio morphology. According to de Vries, Becker & White (2006), most of them have radio structures too compact to be resolved, or if resolved, are recorded as compact symmetric objects, compact steep-spectrum sources and GHz-peaked spectrum sources (An & Baan 2012, and refs. therein). Many of them are as radio loud as FR II RGs and quasars and therefore can also be considered to involve MAD scenario.

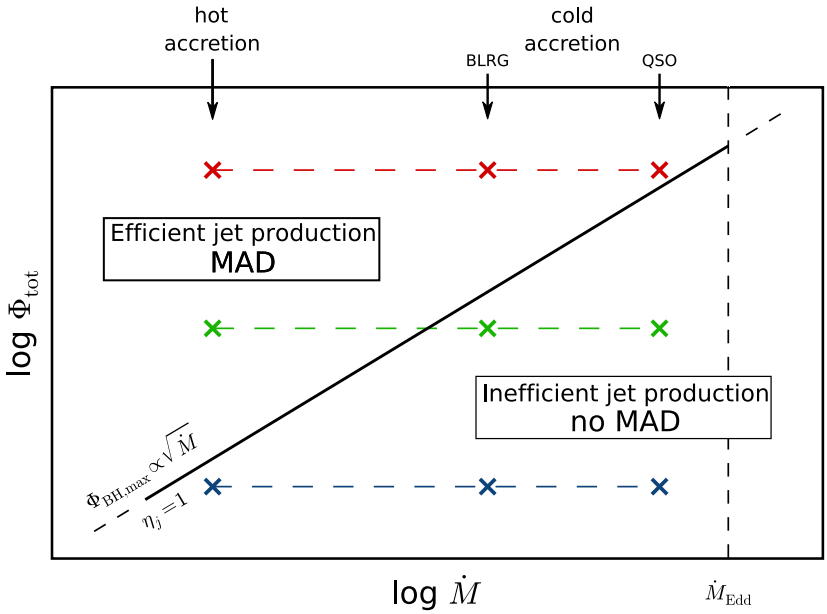

Figure 5. This figure illustrates a condition that must be satisfied in order to obtain the MAD, and also demonstrates how this condition dictates the fraction of radio-loud AGN as a function of accretion rate, $\dot{M}$. The inner accretion flow will become magnetically arrested only if $\Phi_{\rm tot}$ exceeds $\Phi_{\rm BH,max}(\dot{M})$, where $\Phi_{\rm tot}$ is the magnetic flux assumed to be accumulated in the central region of an AGN following the hot accretion phase preceding the higher accretion event associated with the BLRG or quasar phenomenon, while $\Phi_{\rm BH,max}(\dot{M})$ is the maximal magnetic flux that can be confined on a BH by an accretion flow. For $\Phi_{\rm tot} < \Phi_{\rm BH,max}(\dot{M})$ the magnetic flux will be entirely enclosed on the BH and the MAD will not be formed. It is assumed that efficient jet production (and therefore highly radio-loud AGN) only occur in the MAD case, when $\Phi_{\rm tot} > \Phi_{\rm BH,max}(\dot{M})$, while jet production is assumed to be inefficient in the case of No MAD when $\Phi_{\rm tot} < \Phi_{\rm BH,max}(\dot{M})$. This condition implies that the fraction of AGN that are radio loud decreases with increasing $\dot{M}$. For details see Sikora & Begelman (2013).

However, about 90 percent of all quasars are not detected in radio or have very weak radio emission, which can be associated with starburst activities (Kimball et al. 2011) or with shocks formed by the quasar-driven outflows (Zakamska & Greene 2014).

It is tempting to speculate that the reason for a very small fraction of RLQs is associated with 'a steep magnetic-flux function' of quasar precursors developed during a hot, quasi-spherical accretion phase, where the steepness can be determined by different levels of ordering in the magnetic fields that are advected to the centre, and/or by the duration of the quasar pre-phase (Sikora & Begelman 2013). This scenario is schematically illustrated in Fig. 5. For a given amount of magnetic flux $\Phi_{\rm tot}$ accumulated during the quasar pre-phase (Bondi accretion phase), the MAD accretion mode will operate during a subsequent BLRG/quasar phase only if $\Phi_{\rm tot}$ exceeds $\Phi_{\rm BH,max}(\dot{M})$. One can easily deduce from this figure that the fraction of objects operating in the MAD mode is predicted to increase with decreasing accretion rate. Such a trend is indicated at higher accretion rates by studies of quasars (Kratzer & Richards 2015), at moderate accretion rates – by studies of double-peak emission line galaxies (Wu & Liu 2004), and at very low accretion rates – by studies of nearby galaxies (Terashima & Wilson 2003; Chiaberge, Capetti & Macchetto 2005). Indications of a possible MAD scenario operation during the Bondi accretion phase have been recently provided by studies of $P_{\rm j}/\dot{M}_{\rm Bondi}$ in several nearby radio galaxies (Nemmen & Tchekhovskoy 2015).

Finally, we consider variability of the accretion rate as a possible complicating factor in our interpretation of the $P_{\rm j}/L_{\rm d}$–$\lambda_{\rm Edd}$ distribution. The radio luminosity is related to the total energy content of the lobes, and is dependent on the time-averaged jet power averaged over the lifetime of the source. As a result, the jet power calculated from the lobe radio luminosity represents a measure of the time-averaged jet power. The hotspot luminosity may vary on short time-scales due to variation in jet power, but the hotspots typically contribute only a small fraction of the total radio luminosity (Mullin, Riley & Hardcastle 2008), and so the integrated lobe luminosity will not be significantly affected by short time-scale variation in the jet power. In contrast, the disc luminosity is a measure of instantaneous accretion rate, and the accretion rate may vary significantly on time-scales much shorter than the lifetime of the radio galaxy. As a result, variability of the accretion disc luminosity will cause variability in the 'apparent' jet production efficiency and Eddington ratio. Consider for example a source in which the accretion power varies by a factor of 10 between its maximum and minimum accretion rates. This object, if observed during its accretion rate minimum, will appear to have 10 times lower Eddington ratio and 10 times larger jet production efficiency than if it were observed at its accretion rate maximum. In effect, variability of the accretion rate will cause the $P_{\rm j}/L_{\rm d}$–$\lambda_{\rm Edd}$ distribution to be stretched along a line with slope -1 in the $P_{\rm j}/L_{\rm d}$–$\lambda_{\rm Edd}$ plane, broadly consistent with the slope of the distribution of points shown in Fig. 4. Furthermore, for a duty cycle of $\sim$1/2, the object's apparent jet production efficiency will be about five times larger than the true jet production efficiency when observed at its minimum accretion rate, and about two times smaller when observed at its maximum accretion rate. A natural driver of variability in the accretion rate is viscous instabilities in accretion discs (Janiuk, Czerny & Siemiginowska 2002; Janiuk & Czerny 2011). Observational support for this hypothesis may come from the spatial modulation of the radio brightness distributions seen in some large-scale jets (Godfrey et al. 2012).

4 SUMMARY

The compilation of data on $P_{\rm j}/L_{\rm d}$ and $\lambda_{\rm Edd}$ taken from four independently selected samples clearly show a drop of the jet production

efficiency at higher accretion rates (Fig. 4). It is tempting to connect this drop in jet production efficiency with a transition from radiatively inefficient, optically thin accretion flows (RIAF) to the standard, optically thick accretion discs and assume that the key ingredient for jet production is the presence of the hot gas associated with the bulk accretion flow (at low accretion rates) or with the disc corona (at high accretion rates; e.g. Cao 2004; Wu et al. 2013). However, in order to produce at $\lambda_{\rm Edd} > 0.01$ jets with $P_{\rm j}/L_{\rm d}$ approaching unity, as is observed for many objects, requires magnetic fluxes in the central regions too large to be supported by disc coronas. This argument favours the MAD scenario, but with a geometrical thickness of accretion flows much larger than the thickness predicted by standard theory. Whether the discs become thicker once entering the MAD zone, or must be already thicker prior to the MAD zone is the subject for future investigations.

ACKNOWLEDGEMENTS

We thank an anonymous referee for his/her critical comments that helped us to improve the paper. MS thanks Aleksander Sądowski for helpful discussions. The research leading to these results has received funding from the Polish National Science Centre grant 2013/09/B/ST9/00026 and from the European Research Council under the European Union's Seventh Framework Programme (FP/2007-2013)/ERC Advanced Grant RADIOLIFE-320745.

REFERENCES

An T., Baan W. A., 2012, ApJ, 760, 77
Antognini J., Bird J., Martini P., 2012, ApJ, 756, 116
Avara M. J., McKinney J. C., Reynolds C. S., 2016, MNRAS, 462, 636
Begelman M. C., Pringle J. E., 2007, MNRAS, 375, 1070
Begelman M. C., Armitage P. J., Reynolds C. S., 2015, ApJ, 809, 118
Best P. N., Heckman T. M., 2012, MNRAS, 421, 1569
Bird J., Martini P., Kaiser C., 2008, ApJ, 676, 147
Blandford R. D., Znajek R. L., 1977, MNRAS, 179, 433
Blundell K. M., Rawlings S., 2000, AJ, 119, 1111
Blundell K. M., Rawlings S., Willott C. J., 1999, AJ, 117, 677
Cao X., 2004, ApJ, 613, 716
Chiaberge M., Capetti A., Macchetto F. D., 2005, ApJ, 625, 716
de Vries W. H., Becker R. H., White R. L., 2006, AJ, 131, 666
Elvis M., Risaliti G., Zamorani G., 2002, ApJ, 565, L75
Eracleous M., Halpern J. P., 1994, ApJS, 90, 1
Eracleous M., Halpern J. P., 2003, ApJ, 599, 886
Falder J. T. et al., 2010, MNRAS, 405, 347
Fanidakis N., Baugh C. M., Benson A. J., Bower R. G., Cole S., Done C., Frenk C. S., 2011, MNRAS, 410, 53
Fernandes C. A. C. et al., 2011, MNRAS, 411, 1909
Fernandes C. A. C. et al., 2015, MNRAS, 447, 1184
Garofalo D., Evans D. A., Sambruna R. M., 2010, MNRAS, 406, 975
Godfrey L. E. H., Shabala S. S., 2013, ApJ, 767, 12
Godfrey L. E. H. et al., 2012, ApJ, 758, L27
Häring N., Rix H.-W., 2004, ApJ, 604, L89
Igumenshchev I. V., 2008, ApJ, 677, 317
Janiuk A., Czerny B., 2011, MNRAS, 414, 2186
Janiuk A., Czerny B., Siemiginowska A., 2002, ApJ, 576, 908
Kellermann K. I., Sramek R., Schmidt M., Shaffer D. B., Green R., 1989, AJ, 98, 1195
Kelly B. C., Shen Y., 2013, ApJ, 764, 45
Kimball A. E., Kellermann K. I., Condon J. J., Ivezić Ž., Perley R. A., 2011, ApJ, 739, L29
Körding E. G., Jester S., Fender R., 2006, MNRAS, 372, 1366
Kratzer R. M., Richards G. T., 2015, AJ, 149, 61
Lacy M., Ridgway S. E., Sajina A., Petric A. O., Gates E. L., Urrutia T., Storrie-Lombardi L. J., 2015, ApJ, 802, 102
Laor A., Netzer H., 1989, MNRAS, 238, 897
Livio M., Pringle J. E., King A. R., 2003, ApJ, 593, 184
Lu Y., Wang T., Zhou H., Wu J., 2007, AJ, 133, 1615
McKinney J. C., Tchekhovskoy A., Blandford R. D., 2012, MNRAS, 423, 3083
Mingo B., Hardcastle M. J., Croston J. H., Dicken D., Evans D. A., Morganti R., Tadhunter C., 2014, MNRAS, 440, 269
Mullin L. M., Riley J. M., Hardcastle M. J., 2008, MNRAS, 390, 595
Narayan R., Igumenshchev I. V., Abramowicz M. A., 2003, PASJ, 55, L69
Nemmen R. S., Tchekhovskoy A., 2015, MNRAS, 449, 316
Netzer H., 2009, MNRAS, 399, 1907
Nipoti C., Blundell K. M., Binney J., 2005, MNRAS, 361, 633
Novikov I. D., Thorne K. S., 1973, in DeWitt C., DeWitt B. S., eds, Black Holes (Les Astres Occlus). Gordon & Breach, New York, p. 343
O'Dea C. P., Daly R. A., Kharb P., Freeman K. A., Baum S. A., 2009, A&A, 494, 471
Punsly B., 2007, MNRAS, 374, L10
Punsly B., Igumenshchev I. V., Hirose S., 2009, ApJ, 704, 1065
Punsly B., Reynolds C., Marziani P., O'Dea C. P., 2016, MNRAS, 459, 4233
Rafter S. E., Crenshaw D. M., Wiita P. J., 2011, AJ, 141, 85
Rawlings S., Saunders R., 1991, Nature, 349, 138
Reynolds C. S., Begelman M. C., 1997, ApJ, 487, L135
Richards G. T. et al., 2006, ApJS, 166, 470
Różańska A., Malzac J., Belmont R., Czerny B., Petrucci P.-O., 2015, A&A, 580, A77
Shen Y. et al., 2011, ApJS, 194, 45
Sikora M., Begelman M. C., 2013, ApJ, 764, L24
Sikora M., Stawarz Ł., Lasota J.-P., 2007, ApJ, 658, 815
Sikora M., Stasińska G., Kozieł-Wierzbowska D., Madejski G. M., Asari N. V., 2013, ApJ, 765, 62
Sołtan A., 1982, MNRAS, 200, 115
Sądowski A., 2016, MNRAS, 462, 960
Tchekhovskoy A., Narayan R., McKinney J. C., 2011, MNRAS, 418, L79
Terashima Y., Wilson A. S., 2003, ApJ, 583, 145
Tremaine S. et al., 2002, ApJ, 574, 740
van Velzen S., Falcke H., 2013, A&A, 557, L7
van Velzen S., Falcke H., Körding E., 2015, MNRAS, 446, 2985
Véron-Cetty M.-P., Véron P., 1989, ESO Sci. Rep., 7, 1
Volonteri M., Sikora M., Lasota J.-P., Merloni A., 2013, ApJ, 775, 94
White R. L., Helfand D. J., Becker R. H., Glikman E., de Vries W., 2007, ApJ, 654, 99
White S. V., Jarvis M. J., Häußler B., Maddox N., 2015, MNRAS, 448, 2665
Willott C. J., Rawlings S., Blundell K. M., Lacy M., 1999, MNRAS, 309, 1017
Wilson A. S., Colbert E. J. M., 1995, ApJ, 438, 62
Woo J.-H., Urry C. M., 2002, ApJ, 579, 530
Wu X.-B., Liu F. K., 2004, ApJ, 614, 91
Wu Q., Cao X., Ho L. C., Wang D.-X., 2013, ApJ, 770, 31
Zakamska N. L., Greene J. E., 2014, MNRAS, 442, 784

SUPPORTING INFORMATION

Supplementary data are available at *MNRAS* online.

tables.tar.gz

Please note: Oxford University Press is not responsible for the content or functionality of any supporting materials supplied by the authors. Any queries (other than missing material) should be directed to the corresponding author for the article.

APPENDIX A: SAMPLES

Here we present astrophysical properties of our samples with detailed calculations described in Section 2. Complete tables are available as a supplementary material in the online journal. A portion is shown here for guidance regarding its form and content.

Table A1. Radio and optical properties of $z < 0.4$ FR II NLRGs from table 1 in Sikora et al. (2013) with some calculated values in this work. The disc luminosities $L_{\rm d}$ were determined using $L_{\rm H\,\alpha}$.

SDSS ID	Cambridge Cat. ID	Redshift	$\log L_{1.4}$ (WHz^{-1})	$\log L_{\rm H\,\alpha}$ (L$_\odot$)	$\log L_{\rm [O\,III]}$ (L$_\odot$)	$\log L_{\rm d}$ (erg s^{-1})	$\log P_{\rm j}$ (ergs^{-1})	$\log P_{\rm j}/L_{\rm d}$	$\log M_{\rm BH}$ (M$_\odot$)	$\log \lambda_{\rm Edd}$
0312.51689.471	4C +00.56	0.0524	25.34	7.605	7.572	44.497	44.4190	−0.0781	8.74	−2.3568
0349.51699.169	6C B165818.4+630042	0.1063	25.45	6.417	6.579	43.309	44.5133	1.2042	7.83	−2.6348
0366.52017.349	6C B171944.8+591634	0.2212	25.59	7.486	6.889	44.378	44.6333	0.2552	8.29	−2.0258
0432.51884.345	7C B073404.1+402639	0.3905	25.59	...	6.806	...	44.6333	...	8.66	...
0436.51883.010	6C B075738.1+435851	0.2554	25.66	6.899	6.740	43.791	44.6933	0.9022	8.42	−2.7428
0439.51877.637	7C B081405.1+450809	0.1422	25.43	5.690	6.322	42.582	44.4961	1.9140	8.17	−3.7018
0448.51900.335	6C B084421.9+571115	0.1937	26.08	7.515	7.887	44.407	45.0533	0.6462	7.98	−1.6868
0450.51908.330	4C +56.17	0.1409	26.05	7.107	6.912	43.999	45.0275	1.0284	8.04	−2.1548

Table A2. Some properties of FR II quasars from table A1 in van Velzen et al. (2015). Few columns calculated in this work were added, together with BH masses and Eddington ratios taken from Shen et al. (2011).

SDSS RA (°)	SDSS Dec. (°)	Redshift	Lobe flux (Jy)	$\log L_{1.4}$ (WHz^{-1})	$\log L_{\rm d}$ (erg s^{-1})	$\log P_{\rm j}$ (erg s^{-1})	$\log P_{\rm j}/L_{\rm d}$	$\log M_{\rm BH}$ (M$_\odot$)	$\log \lambda_{\rm Edd}$
2.910 161	− 10.749 515	1.2712	0.0963	26.9061	46.5254	45.7613	−0.7641	9.65	−1.19
6.808 142	1.610 954	0.9010	0.1056	26.5880	45.6681	45.4887	−0.1794	...	...
10.165 798	15.055 892	0.8844	0.0294	26.0133	45.9686	44.9961	−0.9725	...	...
11.079 023	− 9.002 630	0.9672	0.0509	26.3449	46.1815	45.2803	−0.9012	7.83	0.10
12.273 874	− 0.514 230	3.2310	0.0196	27.1639	46.3095	45.9823	−0.3272	...	...
13.785 633	− 10.868 412	1.3810	0.0303	26.4898	45.9742	45.4045	−0.5697	...	...
15.872 669	0.681 930	1.4331	0.1200	27.1259	46.6872	45.9497	−0.7375	9.47	−0.94
19.457 974	− 9.098 518	0.8284	0.1041	26.4944	46.0661	45.4085	−0.6576	9.18	−1.34

Table A3. Properties from the table 1 in Fernandes et al. (2011) and table 3 in Fernandes et al. (2015) with added $\log P_{\rm j}$ and $\log P_{\rm j}/L_{\rm d}$ values.

Cambridge Cat. ID	Redshift	$\log L_{\nu 151\,\rm MHz}$ (WHz^{-1}sr^{-1})	$\log L_{\rm d}$ (erg s^{-1})	$\log P_{\rm j}$ (erg s^{-1})	$\log P_{\rm j}/L_{\rm d}$	$\log M_{\rm BH}$ (M$_\odot$)	$\log \lambda_{\rm Edd}$
3C 280	0.997	28.29	46.7070	47.2258	0.5188	8.346	0.2467
3C 268.1	0.974	28.21	45.6890	47.1573	1.4683	7.476	0.0993
3C 356	1.079	28.12	46.4350	47.0801	0.6451	8.746	− 0.4260
3C 184	0.994	28.01	45.6080	46.9858	1.3778	8.966	− 1.4685
3C 175.1	0.920	27.98	45.5780	46.9601	1.3821	8.726	− 1.2596
3C 22	0.937	27.96	46.8130	46.9430	0.1300	9.366	− 0.6676
3C 289	0.967	27.95	46.2710	46.9344	0.6634	9.096	− 0.9393
3C 343	0.988	27.78	46.5940	46.7887	0.1947	8.776	− 0.2958

Table A4. Some properties of BLRGs from table 1 in Sikora et al. (2007) with calculated properties in this work.

IAU	Name	Redshift	m_V	A_V	$\kappa_\star$	$\log L_B$ (erg s^{-1})	F_5 (Jy)	$\log L_R$ (erg s^{-1})	$\log P_{\rm j}$ (erg s^{-1})	$\log P_{\rm j}/L_{\rm d}$	$\log M_{\rm BH}$ (M$_\odot$)	$\log \lambda_{\rm Edd}$
0038−0207	3C 17	0.220	18.0	0.08	0.58	43.9	2.480 00	43.2	45.7920	0.8920	8.7	−1.9
0044+1211	4C+11.06	0.226	19.0	0.26	0.28	43.8	0.220 00	42.2	44.9349	0.1349	7.8	−1.1
0207+2931	3C 59	0.110	16.0	0.21	0.28	44.4	0.670 00	42.0	44.7634	− 0.6366	8.9	−1.6
0224+2750	3C 67	0.311	18.6	0.42	0.82	43.8	0.870 00	43.1	45.7063	0.9063	8.1	−1.4
0238−3048	IRAS 02366−3101	0.062	15.0	0.22	0.30	44.2	0.003 43	39.2	42.3634	− 2.8366	8.6	−1.5
0238+0233	PKS 0236+02	0.207	17.7	0.11	0.46	44.1	0.120 00	41.9	44.6777	− 0.4223	8.8	−1.8
0312+3916	B2 0309+39	0.161	18.2	0.49	0.10	44.0	0.822 00	42.5	45.1920	0.1920	8.3	−1.4
0342−3703	PKS 0340−37	0.285	18.6	0.03	0.19	44.2	0.710 00	42.9	45.5349	0.3349	8.8	−1.7

Table A5. The content of the table is analogous to the Table A4(a), but for RLQs instead of BLRGs.

IAU	Name	Redshift	m_V	A_V	$\kappa_\star$	$\log L_B$ (erg s^{-1})	F_5 (Jy)	$\log L_R$ (erg s^{-1})	$\log P_j$ (erg s^{-1})	$\log P_j/L_d$	$\log M_{BH}$ ($M_\odot$)	$\log \lambda_{Edd}$
0019+2602	4C 25.01	0.284	15.4	0.10	0.00	45.6	0.405	42.7	45.3634	−1.2366	9.1	− 0.6
0113+2958	B2 0110+29	0.363	17.0	0.21	0.00	45.2	0.311	42.8	45.4491	−0.7509	9.2	− 1.1
0157+3154	4C 31.06	0.373	18.0	0.18	0.11	44.8	0.394	43.0	45.6206	−0.1794	9.1	− 1.4
0202−7620	PKS 0202−76	0.389	16.9	0.17	0.00	45.3	0.800	43.3	45.8777	−0.4223	9.2	− 1.0
0217+1104	PKS 0214+10	0.408	17.0	0.36	0.01	45.4	0.460	43.1	45.7063	−0.6937	8.9	− 0.7
0311−7651	PKS 0312−77	0.225	16.1	0.32	0.00	45.2	0.590	42.6	45.2777	−0.9223	8.4	− 0.3
0418+3801	3C 111	0.049	18.0	5.46	0.04	45.1	6.637	42.3	45.0206	−1.0794	8.8	− 0.8
0559−5026	PKS 0558−504	0.138	15.0	0.15	0.00	45.1	0.121	41.5	44.3349	−1.7651	7.4	0.6

This paper has been typeset from a TEX/LATEX file prepared by the author.

3 Paper II: On the diversity of jet production efficiency in *Swift*/BAT AGNs

In Rusinek et al. (2020) we focused on studying the radio bimodality in one carefully selected set of AGNs. These objects (numbering 314 objects) chosen from the X-ray *Swift*/BAT catalog are characterized by low redshift, have BH masses (on which the limit of $M_{\rm BH} \geq 10^{8.5} M_{\odot}$ has been imposed, as RL AGNs have on average higher values than RQ AGNs) and bolometric luminosities calculated in the same way for all sources, and have detailed assignments of radio data from uniform radio catalogs (NVSS and FIRST at 1.4 GHz, SUMSS at 843 MHz). All these steps allowed us to build an extremely homogeneous, possibly free from biases, sample.

Our research revealed the bimodal distribution of radio loudness with most of the radio-loud objects having lobed radio morphologies (82% of RL AGNs and RL AGNs constituting 14% of a whole sample). We confirmed the necessity of the MAD scenario in some of the analyzed sources (following the results from Rusinek et al. 2017) and encountered a deficit of jets with intermediate jet production efficiencies (although, this should be treated with caution as only 16% of all radio-detected sources were found to have double radio lobes which allow for jet power estimation using the formula of Shabala and Godfrey 2013) implying the existence of a certain threshold(s) condition(s) for the production of the strongest jets.

This work was closed with a discussion of the possible MAD formation scenarios directing our attention to another investigation presented in the third and final investigation.

The Astrophysical Journal, 900:125 (13pp), 2020 September 10 https://doi.org/10.3847/1538-4357/aba75f

On the Diversity of Jet Production Efficiency in Swift/BAT AGNs

Katarzyna Rusinek[1], Marek Sikora[1], Dorota Kozieł-Wierzbowska[2], and Maitrayee Gupta[1,3]
[1] Nicolaus Copernicus Astronomical Center, Polish Academy of Sciences, Bartycka 18, 00-716 Warsaw, Poland; krusinek@camk.edu.pl
[2] Astronomical Observatory, Jagiellonian University, Orla 171, 30-244 Kraków, Poland
[3] Harvard Smithsonian Center for Astrophysics, 60 Garden Street, Cambridge, MA 02138, USA
Received 2020 June 12; revised 2020 July 16; accepted 2020 July 17; published 2020 September 8

Abstract

We address the very large diversity of jet production efficiency in active galactic nuclei (AGNs) by using data on low-redshift AGNs selected from the Swift/BAT catalog and having black hole (BH) masses larger than $10^{8.5}\,M_{\odot}$. Most of these AGNs accrete at intermediate rates and have bolometric luminosities dominated by mid-IR radiation. Our sample contains 14% radio-loud (RL), 6% radio-intermediate, and 80% radio-quiet (RQ) AGNs. All RL objects are found to have extended radio structures, and most of them have classical FR II morphology. Converting their radio loudness to jet production efficiency, we find that the median of this efficiency is on the order of $(\epsilon_d/0.1)\%$, where $\epsilon_d = L_{\rm bol}/\dot{M}c^2$ is the radiation efficiency of the accretion disk. Without knowing the contribution of jets to the radio emission in RQ AGNs, we are only able to estimate their efficiencies using upper limits. Their median is found to be $0.002(\epsilon_d/0.1)\%$. Our results suggest that some threshold conditions must be satisfied to allow the production of strong, relativistic jets in RL AGNs. We discuss several possible scenarios and argue that the production of collimated, relativistic jets must involve the Blandford–Znajek mechanism and can be activated only in those AGNs whose lifetime is longer than the time required to enter the magnetically arrested disk (MAD). Presuming that MAD is required to collimate relativistic jets, we expect that the weak nonrelativistic jets observed in some RQ AGNs are produced by accretion disks rather than by rotating BHs.

Unified Astronomy Thesaurus concepts: Radio active galactic nuclei (2134); Radio jets (1347); Relativistic jets (1390); Non-thermal radiation sources (1119); AGN host galaxies (2017); Galaxy accretion disks (562)

Supporting material: machine-readable table

1. Introduction

While the first quasars were discovered following the identification of some radio sources with optical point sources located at cosmological distances (Schmidt 1963), it quickly turned out that most of them were radio quiet (RQ; Sandage 1965). This led to their division into radio-loud quasars (RLQs) and RQ quasars (Kellermann et al. 1989) with an approximate number proportion 1:10. However, later studies using deeper radio surveys led to the discovery of many quasars with intermediate radio loudness, and the often-claimed radio bimodality came into question (see Kratzer & Richards 2015, and references therein).

A broad distribution of radio loudness was also found in active galactic nuclei (AGNs) located at much closer distances than luminous quasars (e.g., Rafter et al. 2009), and if the dominating radio flux of the extended radio sources with which they were associated was included, the bimodality reappeared (Rafter et al. 2011). A bimodal radio distribution in AGNs was also confirmed by the recent studies of Gupta et al. (2018, 2020). In order to avoid biases in the determination of the radio-loudness distribution associated with optical and radio selection limits, Gupta et al. based their studies on a sample of AGNs selected from the Swift/BAT catalog (Ricci et al. 2017). Due to the very low sensitivity of the BAT detector, most of these AGNs are located at low redshift. The radio-loudest AGNs were found, like in quasars, in AGNs with $M_{\rm BH} > 10^8 M_{\odot}$, but with much lower accretion rates. The latter also concerns RQ AGNs with very massive black holes (BHs) and can be explained by the "downsizing effect," according to which the average specific accretion rates in massive AGNs decrease with decreasing redshift (e.g., Fanidakis et al. 2012). In order to minimize the impact of RL and RQ AGNs having different average BH masses and Eddington ratios ($\lambda_{\rm Edd} = L_{\rm bol}/L_{\rm Edd}$) on the compared radio properties, the sample adopted from the Swift/BAT catalog of AGNs was reduced to have RQ and RL AGNs with similar ranges of these parameters.

The advantages of studying the radio properties of AGNs and possible relations to the optical properties of their host galaxies and environments using the low-redshift samples are obvious: (1) almost all of these AGNs have radio detections, (2) studies of radio morphology are not limited to only extended radio sources, (3) studies of optical morphology of their hosts and environment are possible, (4) biases associated with cosmological evolution are minimized, and (5) a much lower probability of having radio-intermediate (RI) AGNs dominated by strong starbursts and accretion disk winds. Hence, studies incorporating such samples have exceptional potential to provide a variety of constraints that can be used to select the most promising scenario to explain the origin of the large diversity of jet production efficiency.

Our work is organized as follows: in Section 2 the sample is defined; in Section 3 the radio-loudness distribution is derived and radio morphologies are determined; in Section 4 bolometric luminosities, BH masses, Eddington ratios, and jet powers are derived and used to construct the distribution of jet production efficiency; and in Section 5 properties of the host galaxies are reviewed. A comparison of our results with others and their theoretical implications and possible interpretations are provided in Section 6 and summarized in Section 7.

Throughout the paper, we assume a ΛCDM cosmology with $H_0 = 70$ km s^{-1} Mpc^{-1}, $\Omega_m = 0.3$, and $\Omega_\Lambda = 0.70$.

2. The Sample

Our initial sample is taken from Gupta et al. (2018, 2020), who performed a comparison of RL and RQ, both Type 1 and

Type 2, AGNs in various spectral bands. The sources in their sample were selected from the BAT AGN Spectroscopic Survey (Ricci et al. 2017), by excluding blazars, Compton-thick ($\log N_{\rm H} > 24$) AGNs, and sources with missing optical spectroscopic classification in Koss et al. (2017), which resulted in 664 objects. The sample in Gupta et al. (2018) was limited to 70 sources. This was due to the limits imposed on BH masses and Eddington ratios ($8.48 \leqslant \log M_{\rm BH} \leqslant 9.5$, $-2.55 \leqslant \log \lambda_{\rm Edd} \leqslant -1$), which gave the authors possibly the best representation of radio galaxies and their RQ counterparts working at intermediate accretion rates. In Gupta et al. (2020), some of the earlier restrictions were relaxed and additionally, using the relation between BH masses and the near-infrared (NIR) luminosities of host galaxies of AGNs (Marconi & Hunt 2003; Graham 2007), the BH masses were calculated. As a result, instead of studying only those sources for which the BH masses are known, the sample studied in Gupta et al. (2020) has 290 objects, all of them with $M_{\rm BH} \geqslant 10^{8.5} M_{\odot}$, $z \leqslant 0.35$ and $0.001 \leqslant \lambda_{\rm Edd} \leqslant 0.03$. Hence, we decided to make use of the sample from Gupta et al. (2020) and complete it by adding RI AGNs (which were excluded by the authors; see Gupta et al. 2018, 2020), choosing them in the same way as the other objects were found. This resulted in finding 24 additional sources (out of which four turned out to be RQ), giving us a final sample consisting of 314 Swift/BAT AGNs.

The detailed description of the data and the procedure used to build this sample, originally described in Gupta et al. (2018, 2020), is reiterated in Appendix A.

3. Radio Properties

3.1. Radio Loudness

Our radio-loudness parameter, as in Gupta et al. (2020), is given as $R = F_{1.4}/F_{\nu_{\rm W3}}$, where $F_{1.4}$ and $F_{\nu_{\rm W3}}$ are the monochromatic fluxes at 1.4 GHz[4] and in the Wide-field Infrared Survey Explorer (WISE) at $\nu_{\rm W3} = 2.5 \times 10^{13}$ Hz, respectively. This relates to the definition given by Kellermann et al. (1989), i.e., $R_{\rm KL} = F_5/F_{\nu_{\rm B}}$, where F_5 and $F_{\nu_{\rm B}}$ are the monochromatic fluxes at 5 GHz and in the B band (6.8×10^{14} Hz), as $R \approx 0.1 \times R_{\rm KL}$, assuming the spectral indices of $\alpha_{1.4\text{–}5} = 0.8$ and $\alpha_{\nu_{\rm B}-\nu_{\rm W3}} = 1$ (see Gupta et al. 2018). Based on this, we partitioned the sources into the following radio classes, strictly corresponding to those in Kellermann et al. (1989): RL when $R > 10$, RI for $1 < R < 10$, and RQ when $R < 1$.

Because we used three radio catalogs differing in radio wavelength, angular resolution, and sensitivity, we decided to adopt the radio flux from the National Radio Astronomy Observatory (NRAO) Very Large Array (VLA) Sky Survey (NVSS), whose data are available for most of the sources and whose sensitivity accounts for all of the extended emission. For objects lacking NVSS data, we took fluxes from the Sydney University Molonglo Sky Survey (SUMSS) and Faint Images of the Radio Sky at Twenty-cm (FIRST).[5] Such an approach resulted in finding 44 RL, 20 RI, and 250 RQ AGNs in our sample, with their radio-loudness medians of 75.40, 1.69, and 0.15, respectively. The exact radio-loudness distribution is presented in the top panel of Figure 1.

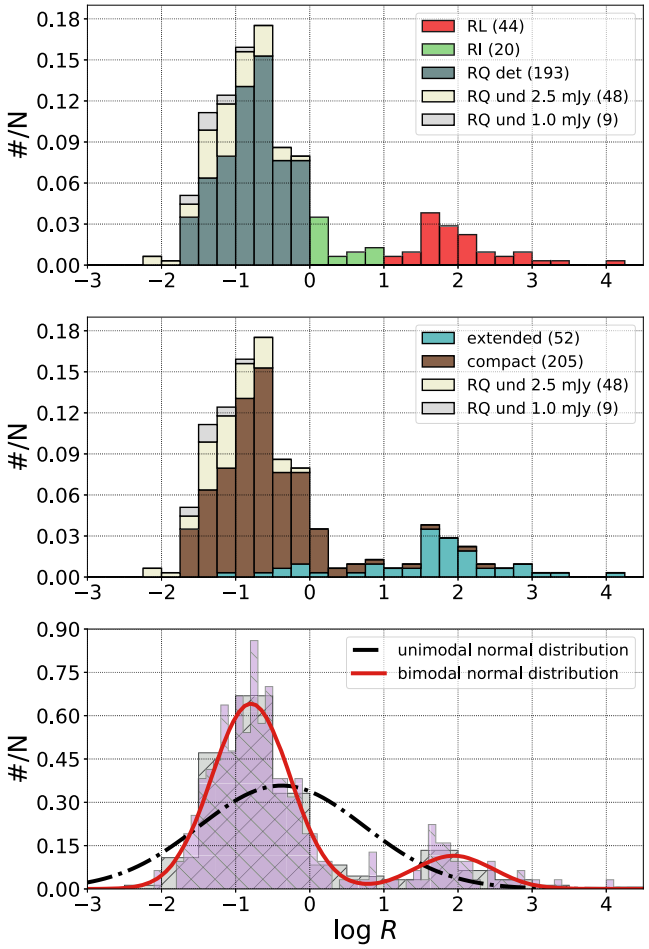

Figure 1. Radio-loudness distribution for Swift/BAT AGNs in our sample. The top panel shows groups of RL (red), RI (green), and RQ (gray) sources, based on the definition of the radio-loudness parameter given as $R = F_{1.4}/F_{\nu_{\rm W3}}$, which, for the given classes, takes values of $R > 10$, $1 < R < 10$, and $R < 1$, with its median value of $\log R$ equal to 1.88, 0.23, and −0.84, respectively. In the RQ class, we separate sources with (RQ detected, dark gray, with a median value of $\log R \simeq -0.75$) and without radio detections, dividing the latter group into two categories: RQ undetected with a 2.5 mJy detection upper limit (light yellow) when the source is in the footprint of NVSS or SUMSS, and RQ undetected up to 1.0 mJy (light gray) when the source is in the FIRST area. The middle panel distinguishes between sources with (teal) and without (brown) extended radio emission together with the same groups of RQ undetected AGNs as mentioned earlier. Here the median values of $\log R$ are 1.74 and −0.72 for extended and compact AGNs, respectively. The characteristics of these radio morphologies are closely described in Sections 3.2.1 and 3.2.2, and exact numbers are presented in Table 1. The bottom panel shows the sample distribution using two different bin widths in gray and purple. Overplotted are the maximum likelihood estimates for unimodal and bimodal normal distributions in black and red, respectively.

Among 314 Swift/BAT AGNs, 257 of them have and 57 lack radio data. As one can see in Figure 1, those radio-undetected sources belong entirely to the RQ class. In the group of radio-detected objects, we can specify two subsamples of sources for which we have both: (1) NVSS and SUMSS data (12 sources) and (2) NVSS and FIRST data (76 sources). While the NVSS and SUMSS total fluxes (compared at 1.4 GHz) are almost the same, the ratio of NVSS to FIRST total fluxes is slightly more significant, with a median of 1.2, showing that, indeed, some of the faint extended radio emission might be lost while using only higher angular resolution and better sensitivity radio data.

[4] Those are taken from NVSS, FIRST, and SUMSS, where radio fluxes from the latest, at 843 MHz, were recalibrated to 1.4 GHz using a radio spectral index of $\alpha_r = 0.8$ and the convention of $F_\nu \propto \nu^{-\alpha}$; see Appendix A.1.

[5] The exception being the group of 57 compact sources, for which, even though they have data in both, NVSS and FIRST, we decided to take the FIRST fluxes. The explanation is given in Appendix B. This choice, however, does not affect the ascription to their radio classes.

3.2. Radio Morphologies

Within the group of 257 radio-detected AGNs, we can distinguish two main subsamples—those with and without extended radio emission, represented by 52 and 205 objects, respectively. Below we give detailed characteristics of our radio morphological classification.

3.2.1. Compact Sources

Sources belonging to the group of compact AGNs are defined as those for which only one radio match, with its location corresponding to the optical center, was found. Based on whether or not the accurate size of the fitted major axis after deconvolution in a given radio catalog was available, compact sources form two groups: resolved and unresolved, consisting of 91 and 114 sources, respectively.

3.2.2. Extended Sources

All AGNs with more than one confirmed radio match are classified as extended. Based on the appearance of their radio morphologies, this subsample has been divided into the following morphological groups:

1. *complex*, in which we include sources with multiple pairs of lobes, i.e. double–double radio galaxies (DDRG) and X-shaped sources (five sources),[6]
2. *triple*, when the core and a pair of lobes are clearly visible (20 sources),
3. *double*, objects with a pair of lobes but with no detection of a core corresponding to the optical center (15 sources),
4. *knotty*, sources with quite extended, yet difficult to define, emission present on the radio map (12 sources).

In general, the extended radio emission from AGNs in our sample can be distinguished into sources with (complex, triple, double) and without (knotty) visible radio lobes.

3.2.3. Radio Morphology versus Radio-loudness Classification

Using the above-described division of radio-detected AGNs, we checked how our radio morphological groups relate to the radio-loudness categorization. In Table 1 we list these characteristics. Most of the RL sources are found to have lobed radio morphologies (36 out of 44),[7] while almost all RQ objects correspond to compact sources (186 out of 193). In the case of RI objects, the ratio of sources with extended radio emission to those without is 1:3. This shows that the fraction of AGNs with extended radio emission decreases along with their radio loudness, which is not only clearly visible in Figure 1 but is also reflected by the quite similar median values of the radio loudness of RL and extended sources (75.40 and 54.61) and of RQ detected and compact sources (0.18 and 0.19).

In addition to the above, we analyzed whether a unimodal or bimodal normal distribution best corresponds to our radio-loudness sample. We performed a maximum likelihood estimate to fit the data to the two distributions and then conducted a Kolmogorov–Smirnov test with $p$values of 3.13×10^{-10} and 0.87 for the uni- and bimodal distributions, respectively. We found that while the unimodal distribution differs significantly from the observed sample, the same cannot be said about the bimodal distribution. The fitted distributions are shown on the bottom panel in Figure 1.

Table 1
Radio Morphologies and Radio Classes of Radio-detected Sources (257 Objects) in Our Sample of Swift/BAT AGNs

Radio Morphology		Radio Class			Total
		RL	RI	RQ	
Extended	Complex	5			5
	Triple	16	4		20
	Double	15			15
	Knotty	4	1	7	12
Compact	Resolved	4	3	84	91
	Unresolved		12	102	114
Total		44	20	193	257

Note. A detailed description is given in Section 3.2.

3.2.4. FR I/II Classification

For sources with a lobed radio morphology (i.e., complex, triple, and double objects; 40 AGNs total) based on the appearance of their radio maps, we established their Fanaroff–Riley classification (Fanaroff & Riley 1974), finding the following: four objects of type FR I, two AGNs of mixed FR I/II class, and 34 type FR II AGNs. Our classification is in an agreement with the data given in, e.g., Rafter et al. (2011), Kozieł-Wierzbowska & Stasińska (2011), and Panessa et al. (2016).

3.3. Physical Sizes

The (projected) largest linear size (LLS) was determined for each radio-detected source in our sample. Noting that the true definition of LLS is given as the distance between two hot spots, the most reliable calculations are available for sources with double radio lobes. For complex AGNs with multiple pairs of lobes, the pair with the largest separation was used. The sizes of knotty radio sources correspond either to the distances between the most distant radio matches or to our measurements obtained from their radio maps. The sizes of compact AGNs (exact measurements for resolved and upper limits for unresolved objects) were taken directly from the radio catalogs as the major axis of the fitted Gaussian (a detailed procedure for the size estimation of compact AGNs is given in Appendix B).

The results for the LLS calculations for all the radio-detected sources are shown in the left panel of Figure 2. Knowing that only three out of six morphological groups (namely, complex, triple, and double sources) presented in this paper have direct measurements of the projected size and the sizes of compact (unresolved and resolved) and knotty sources are upper limits (i.e., are possibly shifted to the left on this chart), a clear trend confirming our results from Section 3.2.3 is found, namely, the most extended AGNs are RL whereas the RQ ones do not achieve such big sizes. This distinction is especially visible in the right panel of Figure 2, where only compact sources with radio data from FIRST (which, within the group of 57 compact sources, provides more precise, and is on average 15 times smaller sizes than NVSS; see Appendix B) are included. This figure shows that compact resolved and compact unresolved objects are in fact located in different parts of the diagram.

[6] Those are PKS 0707–35, B2 1204+34, 3C 403, 3C 445, and PKS 2356–61.

[7] From the literature, we found that four out of eight RL AGNs without lobes have, in fact, double radio structures. Those objects are PKS 0222–23 in Kapahi et al. (1998a), PKS 0326–288 in Kapahi et al. (1998b), [HB89] 1130 +106 in Nilsson (1998), and PKS 1916–300 in Duncan & Sproats (1992).

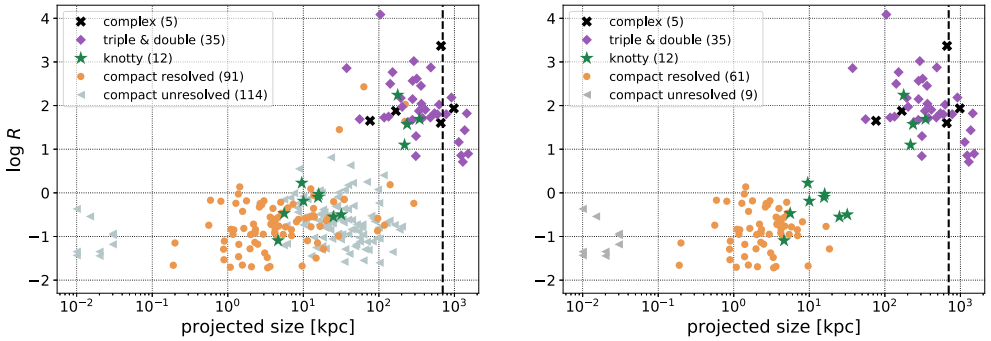

Figure 2. Distribution of radio-detected sources in the log R vs. projected size plane. Morphological groups are presented as follows: complex correspond to black crosses, triples and doubles are presented together as purple diamonds, knotty objects are marked as green stars, and the group of compact resolved sources is shown as orange circles while compact unresolved ones correspond to gray triangles. The left panel presents all radio-detected objects (257 AGNs). Compact sources on the right panel have been limited to those with FIRST data used (122 AGNs total), which allow a clear separation to be seen between resolved and unresolved objects. Nine of our sources have sizes corresponding to GRGs and those are located to the right of the vertical dashed line marking the size of 700 Mpc.

From Figure 2 we note that nine sources have projected sizes beyond 700 kpc, which is the definition of giant radio galaxies (GRGs). The fraction of GRGs in our sample compared to the total number of lobed sources ($9/40 \approx 23\%$) is almost the same as in Bassani et al. (2016), where the authors found that 14 out of their 64 confirmed radio galaxies selected in the soft gamma-ray band and having double-lobe morphologies have giant sizes. Furthermore, Bruni et al. (2019) found that 61% of Bassani et al. giant radio sources have a gigahertz-peaked spectrum (GPS) cores, i.e., young nuclei. We checked that all of our GRGs are in common with those studied by Bruni et al. (2019), with six of them (67%) having GPS cores suggesting the ongoing accretion and reactivation of the jets.[8] By contrast, four of their AGNs are not found in our sample as they were not observed by Swift/BAT or have blazar-like nuclei, while another two sources (namely 4C +63.22 and PKS 2356–61) listed in Bruni et al. are not recognized as GRGs because their sizes, estimated in this work, are slightly below 700 kpc.

4. Jet Production Efficiency

4.1. Bolometric Luminosity

We started our calculations of bolometric luminosity by checking whether or not the method in which MIR W3 fluxes were used to estimate $L_{\rm bol}$, as was done in Gupta et al. (2018), can be successfully applied to our sample of AGNs accreting at a moderate accretion rate. Such verification was possible due to the accessibility of the multiband spectra, and in turn, the exact values of bolometric luminosities, which are presented in Gupta et al. (2020), upon which we built our sample of Swift/BAT AGNs.

We decided to analyze a subsample consisting of 131 (20 RL, 111 RQ) sources—all of those being Type 1 and having strict MIR, NIR, optical-UV, and hard X-rays detections (for more details, see Section 4 in Gupta et al. 2020). This choice was dictated by our need of having possibly the most accurate estimations of $L_{\rm bol}$ in which the obscuration by the dusty torus is minimized.

By representing the given subsample in the $\log(\nu_{\rm W3}\, L_{\nu_{\rm W3}})$ versus $\log L_{\rm bol}$ plane, where $L_{\rm bol}$ is taken from Gupta et al. (2020, the specific formulas can be found in Appendix B therein) and for which the distribution is shown in Figure 3, we found that indeed almost all sources exhibit linear correlation ($r \approx 0.90$, where r is the correlation coefficient) between monochromatic luminosity in the W3 band and bolometric luminosity in their logarithmic quantities.[9] Linear regression produces a formula of such a dependence, which is given as

$$L_{\rm bol}\ [{\rm erg\ s^{-1}}] = 3.25 \times (\nu_{\rm W3}\, L_{\nu_{\rm W3}}\ [{\rm erg\ s^{-1}}])^{1.0086}, \qquad (1)$$

which for $\nu_{\rm W3}\, L_{\nu_{\rm W3}}$ in the range 10^{42}–10^{46} erg s^{-1} is well approximated by

$$L_{\rm bol}\ [{\rm erg\ s^{-1}}] \simeq 7.77 \times \nu_{\rm W3}\, L_{\nu_{\rm W3}}\ [{\rm erg\ s^{-1}}]. \qquad (2)$$

The median ratio of bolometric luminosity obtained from the whole spectral energy distribution (SED) to that calculated from Equation (2) for a studied subsample of 131 sources is 0.96. Hence, we conclude that the estimation of bolometric luminosity for AGNs accreting at a moderate accretion rate from the monochromatic MIR luminosity is reliable and can be effectively used for our whole sample.

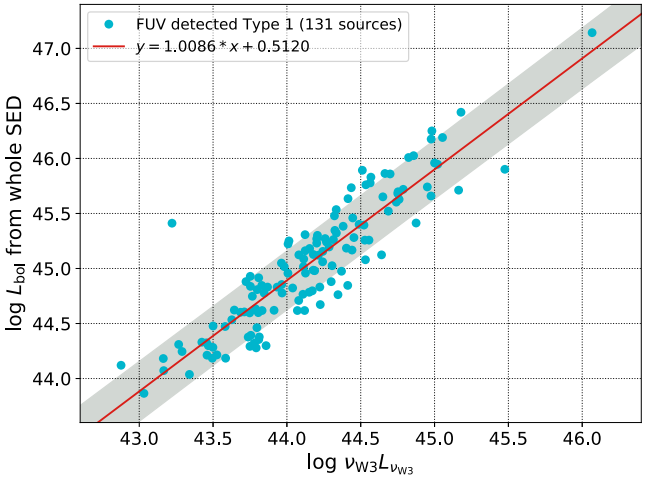

Figure 3. Comparison of monochromatic luminosity in the W3 band, $\nu_{\rm W3}L_{\nu_{\rm W3}}$, and bolometric luminosity estimated from the whole SED, $L_{\rm bol}$, for 131 Type 1 AGNs, for which exact measurements (not upper limits) in the FUV band were given in Gupta et al. (2020). The red line corresponds to the linear dependence found between these two parameters via linear regression, and the shaded area illustrates a 1σ confidence interval. Based on such a relation, the bolometric luminosity for all objects in our sample was calculated using Equation (2).

[8] Those are 2MASX J03181899+6829322, IGR 14488–4008, Mrk 1498, 4C +34.47, 4C +74.26, and PKS 2356–61.

[9] The only source not clearly following this trend is LEDA 100168 ($\log \nu_{\rm W3}L_{\nu_{\rm W3}} = 43.22$, $\log L_{\rm bol} = 45.41$).

4.2. BH Mass and Eddington Ratio

In order to obtain BH masses in a uniform way for all AGNs in our sample, we decided to use the relation between BH masses and NIR luminosities of the host galaxies (Marconi & Hunt 2003), with the NIR data being taken from the Two Micron All Sky Survey (Skrutskie et al. 2006). The formula used for our calculations is given as $\log(M_{\rm BH}/M_{\odot}) = -0.37 \times M_{\rm K} - 0.59$ (Graham 2007), where $M_{\rm K}$ is the absolute K-band magnitude of the galaxy. A more specific explanation of this strategy is given in Gupta et al. (2020, see Appendix A therein).

Having calculated bolometric luminosities and BH masses, we obtained the Eddington ratio as $\lambda_{\rm Edd} = L_{\rm bol}/L_{\rm Edd}$, where $L_{\rm Edd}$ is the Eddington luminosity. Its values for the whole sample range from $0.0004 \leqslant \lambda_{\rm Edd} \leqslant 0.1905$,[10] with a median value of $\lambda_{\rm Edd} = 0.011$, and its distribution is presented in the top histogram of Figure 4.

4.3. Jet Power

Among various methods of estimating jet powers of AGNs, we decided to use the one based on the calorimetry of radio lobes, originally formulated by Willott et al. (1999) and modified by Shabala & Godfrey (2013), who, by accounting for radiative losses, delivered a more correct relation. Therefore, the formula adopted by us is given as

$$P_j\ [\mathrm{erg\ s^{-1}}] = 1.5 \times 10^{43} \left[\left(\frac{\nu\ [\mathrm{MHz}]}{151} \right)^{\alpha} \frac{L_{1.4}\ [\mathrm{W\ Hz^{-1}}]}{10^{27}} \right]^{0.8} \times (1+z)\,(D\ [\mathrm{kpc}])^{0.58}, \quad (3)$$

where $L_{1.4}$ is the monochromatic lobe radio luminosity at $\nu = 1.4$ GHz, $\alpha = 0.8$, and D is the source size.

The conversion from radio luminosity to jet power derived by Shabala & Godfrey (2013) is defined for FR II AGNs. These objects constitute 11% of our sample and limiting to those most powerful radio galaxies would give us information about only a fraction of jetted AGNs, clearly biasing our understanding of the jet production mechanisms in various classes of AGNs. The only way to avoid this confusion is to obtain jet powers for all radio-detected sources in our sample by establishing their upper limits. Hence, three groups can be identified: (i) FR II–type AGNs, (ii) objects with lobed but not FR II–type radio morphologies, and (iii) sources with radio detections but without visible double lobes.

A substantial difference appears in our calculations of lobed and nonlobed sources, as for the latter ones we use their total instead of lobe radio luminosity which was originally introduced in Equation (3) and such a quantity can be estimated only for lobed AGNs. Regarding the extraction of lobe radio luminosities, we ensured (when possible) that it does not include any excess radio emission, such as the set of wings in X-shaped sources farther from the core, the outer pair of lobes in DDRGs, or any other radio emission regions which, based on their location on radio maps, do not belong to the radio lobes. In general, the accuracy of the jet power estimation decreases in each of the groups mentioned in the previous paragraph as we have less information about the exact radio characteristics (morphology, size, and flux) of a given source.

[10] The difference between the ranges of $\lambda_{\rm Edd}$ in our and the Gupta et al. (2020) studies results from different methods of $L_{\rm bol}$ estimation.

All jet power calculations for objects in our sample, scaled by bolometric luminosities, are shown in Figure 4.

Even though the results presented in Figure 4 rely mostly on upper limit estimations of P_j (in 223 out of 257 objects), the bimodal distribution of $P_j/L_{\rm bol}$ is evident, noticeably separating objects powered by relativistic jets from sources in which the radio emission may be dominated by star formation, shocks generated by winds from accretion disks and their coronas, or by low-power jets (Panessa et al. 2019 and references therein). No strong dependence between the Eddington ratio and scaled jet power is found in our sample.

5. Host Galaxies

Having well-defined radio properties for most of the objects in our sample, we checked what the characteristics of their optical counterparts were, specifically their host galaxy morphologies. In order to accomplish that, we decided to use data from the Hubble Space Telescope (HST), Sloan Digital Sky Survey (SDSS), Panoramic Survey Telescope and Rapid Response System (Pan-STARRS), and ESO archives, finding that such information is available for 248 out of 314 AGNs, for which we were able to determine the host galaxy type spanning the entire range of redshifts of our full sample.[11] A detailed description of the data and the procedure used to establish the morphologies of host galaxies is given in Appendix C, and below we describe the most important results.

Based on the appearance of the host galaxy in the optical image, we distinguish five morphological groups: elliptical, lenticular, spiral, distorted, and merger.[12] The last two groups refer to galaxies in which we were not able to attribute any of the Hubble morphological types. We call a galaxy distorted when its morphology is disarranged, most probably resulting from galaxy interactions, but with only one nucleus. Galaxies in which two nuclei are present are classified as mergers. Some signs of galactic interactions (like tails, bridges, or small distortions) are also seen in both ellipticals and spirals, constituting ∼11% of each of these types.

In Table 2, we show the above-described host galaxy morphological classification with regard to AGNs with and without powerful jets, represented by RL and RI and RQ sources, respectively. Keeping in mind that we have information for 57% and 83% sources in the RL and in the RI and RQ groups, respectively, we see that the majority of RL objects are found to reside in ellipticals while none are found in spirals, which is not the case for radio-quieter AGNs, where both ellipticals and spirals are present, with a prevalence of the latter. Such an observed lack of spiral morphologies in AGNs with extended radio structures is well documented (e.g., Wilson & Colbert 1995; McLure & Jarvis 2004; Best et al. 2005; Madrid et al. 2006; Wolf & Sheinis 2008) albeit some studies reveal several radio-lobed AGNs showing clear disk and/or spiral morphologies in optical images (see Table 4 in Tadhunter 2016 and references therein). The fraction of objects with disturbed morphologies (distorted and merger) in RL and in RI and RQ AGNs is not very different, being 28% and 21%, respectively.

[11] In fact, all of our objects were found in the given surveys but not all of them had good-enough data to establish their host morphology resulting in the exclusion of 66 objects.

[12] Additionally, we identify one more group, irregular, consisting of only one source, 2MASX J23444387–4243124. We include this object in the distorted group.

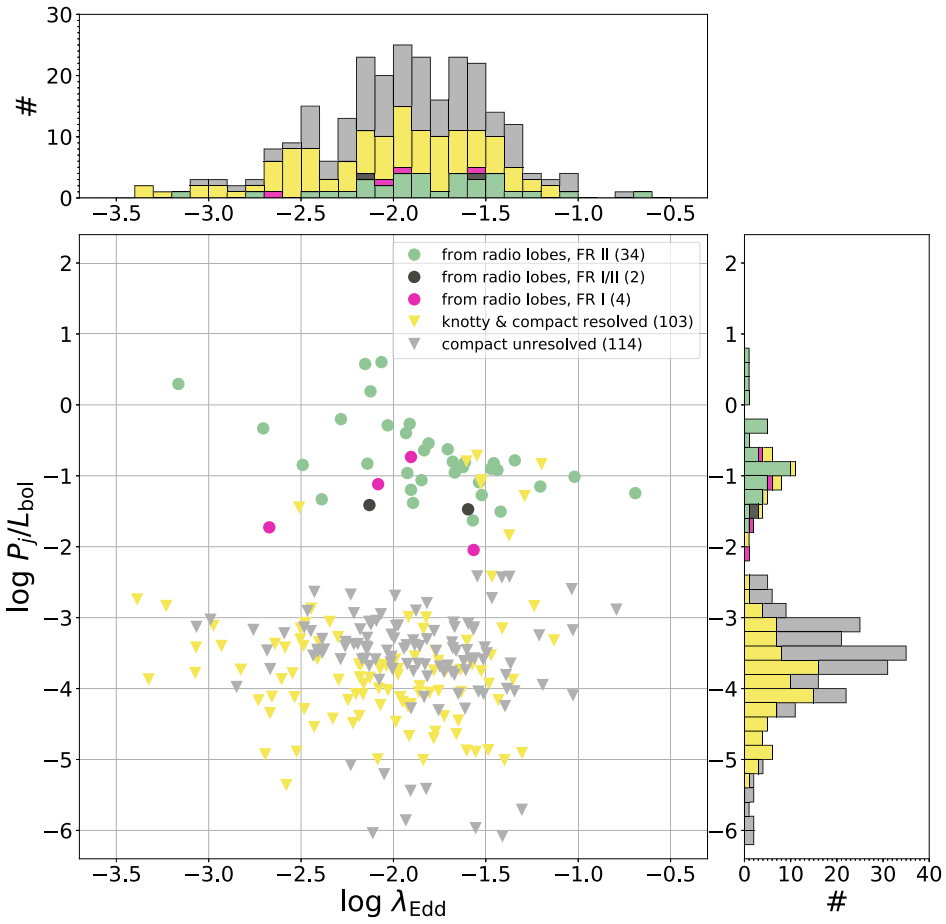

Figure 4. Dependence of the P_j/L_{bol} ratio on the Eddington ratio λ_{Edd}. The sample of 257 radio-detected AGNs has been divided on the basis of how accurate the calculation of jet powers is, i.e., whether the radio emission from lobes can be extracted. The two main groups correspond to lobed sources, which are represented as filled colorful circles (40 objects altogether); and nonlobed radio sources, which are shown as filled colorful triangles (217 objects). Different colors for the group of lobed sources coincide with the Fanaroff–Riley classification: green for FR II, dark gray for FR I/II, and pink for FR I. Nonlobed radio objects are divided into knotty & compact resolved and unresolved ones with yellow and gray colors, respectively.

We note that our results on host galaxies of Swift/BAT AGNs and their relation to radio properties should be treated as the first step toward more extensive research, which we plan to proceed with in the future.

6. Theoretical Implications

While a consensus is almost reached that relativistic jets in RL AGNs are produced involving the Blandford–Znajek (BZ) mechanism (see review by Blandford et al. 2019 and references therein), we are still lacking answers for such basic questions as

(1) what is the dominant driver of the very large diversity of jet production efficiencies indicated by radio observations?
(2) is there any threshold required for the production of jets in RL AGNs?
(3) are the weak jets observed in some RQ AGNs produced by the same mechanism as RL AGNs?
(4) why are powerful jets preferentially produced in AGNs hosted by elliptical galaxies?

Noting that the rate of energy extraction from rotating BHs by the BZ mechanism is $P_{BZ} \propto a^2\Phi_{BH}^2$, where $0 < a < 1$ is the dimensionless BH spin and Φ_{BH} is the magnetic flux confined on the BH by the accretion flow, one may investigate the two following "edge" scenarios to try to explain the diversity of jet production efficiency: the "spin paradigm"—according to which the diversity of the energy extraction rate is driven by the spread in BH spins—and the "magnetic flux paradigm"—where the diversity is determined by the amount of magnetic flux threading the BH.

6.1. Spin Paradigm?

Albeit very popular (Wilson & Colbert 1995; Sikora et al. 2007; Fanidakis et al. 2011; Schulze et al. 2017, and references therein), the "spin paradigm" is seriously challenged by the fact that in order to explain the spread of the jet production efficiency by at least three orders of magnitude, the average BH spin in RQ AGNs should be smaller than 0.03, while that estimated using the "Soltan-type argument" is predicted to be ∼0.6 (Soltan 1982; Chokshi & Turner 1992; Small & Blandford 1992; Elvis et al. 2002; Yu & Tremaine 2002; Lacy et al. 2015). Similarly, large BH spins were found by simulations of the cosmological evolution of BHs (Volonteri et al. 2007, 2013). Hence, in order to reconcile the spin paradigm with RQ AGNs having spins as large as ∼0.6, the dependence of the jet production efficiency on the spin for larger values should be much stronger than quadratic. That possibility was recently claimed to be achievable by Ünal & Loeb (2020) in the model, according to which magnetic fields threading the BH are anchored in the accretion disk. However, noting that magnetic tubes generated in the accretion disk carry on

Table 2
Host Galaxy Morphology of Swift/BAT AGNs of Different Radio Classes

Radio Class	Host Galaxy Morphology						Total
	Elliptical	Lenticular	Spiral	Distorted	Merger	Unknown	
RL	17	1		7		19	44
RI and RQ	45	5	126	40*	7	47	270
Total	62	6	126	47	7	66	314

Note. The source attributed to the irregular group is indicated by a star. The detailed description of host galaxies is given in Section 5.

average zero magnetic flux, the jet is predicted to be produced in a flaring fashion (see, e.g., Yuan et al. 2019; Mahlmann et al. 2020) and the resulting time-averaged jet powers can be much smaller than deduced from observations.

6.2. Magnetic Flux Paradigm?

The above might imply that the large diversity of the jet production efficiency is primarily determined by the amount of magnetic flux collected on the BH. However, in order to convert the electromagnetic outflow generated by the BZ mechanism into narrow, relativistic jets, external confinement is required (Beskin et al. 1998; Chiueh et al. 1998; Lyubarsky & Eichler 2001). Such confinement can be provided by magnetohydrodynamic (MHD) outflows from accretion disks and in the case of powerful jets is presumably associated with magnetically arrested disks (MADs; e.g., Narayan et al. 2003; Tchekhovskoy et al. 2011; McKinney et al. 2012). Because MADs are formed only if the centrally accumulated magnetic flux exceeds the maximum amount that can be confined on the BH by the accretion flow, the division of AGNs into RL and RI/RQ ones is likely to correspond to the division of AGNs with and without MADs, or, equivalently, that the formation of the MAD provides a sort of threshold for launching powerful relativistic jets.

6.3. Jet Powers in AGNs with MADs

In order to reconcile such an "MAD/non-MAD" bimodality with our calculated distribution of the jet production efficiency tracer $P_j/L_{\rm bol}$ (see Figure 4), we need to explain what is the cause of the 2 dex span of this ratio for the RL AGNs assuming they all have MADs. Such a large spread can be an artifact resulting from the calculation of jet powers using their statistical correlation with their radio luminosities (Willott et al. 1999). While adequate in a statistical sense, the conversion formula based on such a correlation may give very large errors for individual sources. Those errors can be associated with the possible spread of parameters such as matter content, minimum electron energy (Willott et al. 1999), cooling effects (Shabala & Godfrey 2013), and density of the environment into which the lobes are inflated (Hardcastle & Krause 2013). But an intrinsic spread of the jet powers in MAD AGNs is also expected, contributed to by the spreads in the BH spin and in the efficiency of the jet collimation by the MHD outflows powered by MADs of different sizes.

It is encouraging to see a similar distribution of $P_j/L_{\rm bol}$ for our RL AGN sample (Figure 4) and for those found by van Velzen & Falcke (2013) and Inoue et al. (2017) for RLQs. They all peak at $P_j/L_{\rm bol} \sim 0.1$ despite the AGNs included in these samples covering very different accretion rates (see also Rusinek et al. 2017, where four various samples of RL AGNs were studied). Such an average value of the jet production efficiency is smaller by a factor ~100 than the maximum predicted for MAD AGNs by numerical simulations (e.g., Tchekhovskoy et al. 2011). However it should be noted that the fraction of maximal magnetic flux confined on the BH by the accretion flow depends on the geometrical thickness of the accretion flow (see Avara et al. 2016) and that $P_j \sim \dot{M}c^2$ (i.e., $P_j \sim 10L_{\rm bol}$ for $\epsilon_d \sim 0.1$) is achievable only for geometrically thick accretion flows, which are not representative for our AGNs nor for quasars.

6.4. Jets in RQ AGNs

As we can see in Table 1, whereas most of the RL AGNs in our sample are extended (40/44), most RI AGNs are compact (15/20). Hence, there is no doubt that the deficiency of RI AGNs with extended structures is real. Such a deficiency does not mean that there is some threshold for operation of the BZ mechanism, but may simply reflect the very inefficient collimation in AGNs without the help of MHD winds from MADs. Then, the badly collimated BZ outflows would be significantly entrained by winds from stars enclosed within the outflow volume, slowed down and shocked, and then most of their kinetic energy would be expected to be converted to plasma heat, rather than used to accelerate relativistic electrons producing synchrotron radiation. Such radio sources, together with accretion disk coronas, presumably represent the compact radio sources observed in RQ and RI AGNs, with others being associated with star formation rates and accretion disk winds/jets (see review by Panessa et al. 2019 and references therein). Some insights into the nature of compact radio sources of RQ Swift/BAT AGNs are provided by Smith et al. (2016, 2020).

6.5. Building Up the MAD

One can envision the following scenarios to form a MAD: by advection of the magnetic flux by accretion flows, by the accumulation of sufficiently large magnetic flux in a galactic core prior to triggering the AGN phase, and by building up the MAD by the so-called "Cosmic Battery" (CB).

Advection of poloidal magnetic fields by accretion disks was predicted to be very efficient by Bisnovatyi-Kogan & Ruzmaikin (1976). Such a possibility was questioned by Lubow et al. (1994), who pointed out that due to the diffusion of magnetic fields in turbulent plasma, such advection cannot proceed in geometrically thin disks. As later studies showed, poloidal magnetic fields can be advected by the surface layers of accretion disks (Bisnovatyi-Kogan & Lovelace 2007; Rothstein & Lovelace 2008; Guilet & Ogilvie 2012, 2013; Zhu & Stone 2018; Cao & Lai 2019). However, the efficiency of such advection can be limited at distances at which models of thin accretion disks predict their fragmentation due to gravitational instabilities (e.g., Hure et al. 1994; Goodman 2003) and ambipolar diffusion in the outer, only partially ionized portions of the accretion flow (e.g., Begelman 1995). Finally, the advected poloidal magnetic field

can be multipolar, and therefore, the formation of a unipolar magnetosphere over the BH and in the innermost portions of the accretion disk—the basic attributes of the MAD—may require more time than the typical lifetime of the AGN, $t_{\rm AGN}$. Then, only AGNs that are at the age $t_{\rm AGN} > \Delta t_{\rm MAD}$ can produce powerful jets, where $\Delta t_{\rm MAD}$ is the time it takes to form the MAD. This possibility seems to be supported by noting that the typical lifetimes of FR II sources are $\sim 3 \times 10^7$ yr (e.g., Bird et al. 2008), while the lifetimes of RQ AGNs are presumably much shorter (e.g., Schawinski et al. 2015; Schmidt et al. 2018; Khrykin et al. 2019). However, it should be noted that the prevalence of MADs in ellipticals over disk galaxies, despite their AGNs having similar lifetimes, can be explained by a larger amount of advected magnetic flux per unit mass in the former.

Regarding the second scenario, Sikora et al. (2013) proposed that the central accumulation of magnetic flux occurs during a hot accretion phase, prior to a cold, higher accretion rate "event" representing the AGN phase. As suggested by Sikora & Begelman (2013), such an event might be triggered by the merger of a giant elliptical galaxy with a disk galaxy.

Finally, MADs can be formed locally via the operation of the CB (Contopoulos & Kazanas 1998; Koutsantoniou & Contopoulos 2014; Contopoulos et al. 2018). The model is based on the Poynting–Robertson radiation drag effect, which generates a nonzero component of the toroidal electric field in the innermost regions of the accretion flow, which in turn gives rise to the growth of poloidal magnetic field loops. Assuming that the outer parts of the loops diffuse outwards, the inner parts must then accumulate onto the BH. The possibility of the formation of a MAD by the CB was numerically confirmed by general-relativistic magnetohydrodynamic (GRMHD) simulations (Contopoulos et al. 2018), though so far only for nonrotating BHs and optically thin accretion flows. Unfortunately, the analytically estimated timescales for building up the MAD for BHs with masses larger than $10^9\ M_\odot$ exceeds the Hubble time (Contopoulos et al. 2018). But, noting that the Poynting–Robertson effect can be much stronger in the case of counter-rotating disks, one cannot exclude the formations of MADs in such AGNs within their lifetime. Combining this possibility with predictions that counterrotating configurations can only be formed following mergers involving giant ellipticals with gas-rich spirals (Garofalo et al. 2020), one can explain why RL AGNs are extremely rarely hosted by spiral galaxies (see Section 5). Furthermore, because the fraction of counterrotating disks formed in such mergers is expected to be <50%, one can also explain why RQ AGNs can be found in both ellipticals and spirals.[13]

[13] The idea of having RL AGNs associated with BHs and accretion disks rotating in opposite directions to each other is not new. It was proposed by Garofalo et al. (2010), based on the works by Reynolds et al. (2006) and Garofalo (2009a, 2009b), who argued that jets produced by the BZ mechanism are more powerful in systems with retrograde disks than in systems with prograde disks. They suggested that this can explain the radio bimodality of AGNs. However, GRMHD simulations showed that the largest jet powers are achievable not in retrograde configurations but in prograde configurations (Tchekhovskoy & McKinney 2012; Tchekhovskoy et al. 2012). This might suggest that opposite to what was proposed by Garofalo et al., RL AGNs should be associated with prograde disks, and, therefore, the fraction of AGNs with retrograde disks should be much larger than the fraction of AGNs with prograde disks. However, the difference of maximal jet powers (those produced assuming the MAD models) produced by AGNs with retro- and prograde disks is much too small (only by a factor ~3) to explain the observed jet production diversity and, therefore, cannot be responsible for the radio-loudness distribution with RL and RQ peaks observed to be separated by a factor of ~500.

7. Summary

In this paper, we investigate in detail the radio properties of massive AGNs ($M_{\rm BH} \geqslant 10^{8.5} M_\odot$) studied by Gupta et al. (2020) and selected from the Swift/BAT catalog (Ricci et al. 2017). Such a sample is excellent for justifying the radio bimodality, claimed by some but questioned by others, and the resulting diversity of jet production efficiency for several reasons. First of all, by selecting via matching the Swift/BAT sources with galaxies, one is avoiding biases associated with radio and optical selection effects; second, most objects in our sample are located at redshifts $z < 0.2$, which allows for the study of their radio and optical morphologies; third, by excluding high accretion rates, we allow the calculation of masses of their host galaxies and, consequently, BH masses using NIR luminosities; fourth, having the radiative output of our objects be dominated by the MIR, given by WISE, and hard X-rays, given by BAT, allowed for reliable estimations of bolometric luminosities; and finally, by excluding Compton-thick AGNs in our sample, we were able to verify the isotropy of some radiative features by comparing them to Type 1 and Type 2 AGNs (see Gupta et al. 2020). Obviously, due to the very low sensitivity of Swift/BAT, the size of our sample is very much limited, and therefore, the presented results must be treated with some caution, but at the same time, they show incredible potential for future use of AGNs selected by the eROSITA survey.

Our main results and their interpretation can be summarized as follows:

1. the distribution of radio loudness in our studied Swift/BAT AGN sample studied is bimodal, with the RL AGNs being on average 500 times radio-louder than RQ AGNs;
2. assuming the same relation between radio luminosity and jet power for the entire sample, the distribution of jet production efficiency and of its upper limits were determined;
3. a deficiency of jets with intermediate jet production efficiency implies the existence of threshold conditions for the production of powerful jets;
4. our premise is that such conditions can be associated with the formation of MADs and that only those AGNs that live longer than the time required to build up the MAD can become RL;
5. the extremely rare cases of having RL AGNs hosted by spiral galaxies and having RQ AGNs hosted by both spiral and elliptical galaxies seem to favor the scenario where the MAD is built up by the CB and can be accomplished within the AGN lifetime only in AGNs with accretion disks rotating in the opposite direction to the BH.

We thank David Abarca for useful discussions and editorial assistance. The research leading to these results has received funding from the Polish National Science Centre grant 2016/21/B/ST9/01620 and NAWA (Polish National Agency for Academic Exchange) grant PPN/IWA/2018/1/00100.

Facilities: Based on observations made with the NASA/ESA Hubble Space Telescope, and obtained from the Hubble Legacy Archive, which is a collaboration between the Space Telescope Science Institute (STScI/NASA), the Space Telescope European Coordinating Facility (ST-ECF/ESA), and the Canadian Astronomy Data Centre (CADC/NRC/CSA).

Funding for the Sloan Digital Sky Survey IV has been provided by the Alfred P. Sloan Foundation, the US Department of Energy Office of Science, and the Participating Institutions. SDSS-IV acknowledges support and resources from the Center for High-Performance Computing at the University of Utah. The SDSS website is www.sdss.org.

SDSS-IV is managed by the Astrophysical Research Consortium for the Participating Institutions of the SDSS Collaboration including the Brazilian Participation Group, the Carnegie Institution for Science, Carnegie Mellon University, the Chilean Participation Group, the French Participation Group, Harvard-Smithsonian Center for Astrophysics, Instituto de Astrofísica de Canarias, The Johns Hopkins University, Kavli Institute for the Physics and Mathematics of the Universe (IPMU)/University of Tokyo, the Korean Participation Group, Lawrence Berkeley National Laboratory, Leibniz Institut für Astrophysik Potsdam (AIP), Max-Planck-Institut für Astronomie (MPIA Heidelberg), Max-Planck-Institut für Astrophysik (MPA Garching), Max-Planck-Institut für Extraterrestrische Physik (MPE), National Astronomical Observatories of China, New Mexico State University, New York University, University of Notre Dame, Observatário Nacional/MCTI, The Ohio State University, Pennsylvania State University, Shanghai Astronomical Observatory, United Kingdom Participation Group, Universidad Nacional Autónoma de México, University of Arizona, University of Colorado Boulder, University of Oxford, University of Portsmouth, University of Utah, University of Virginia, University of Washington, University of Wisconsin, Vanderbilt University, and Yale University.

The Pan-STARRS1 Surveys (PS1) and the PS1 public science archive have been made possible through contributions by the Institute for Astronomy, the University of Hawaii, the Pan-STARRS Project Office, the Max-Planck Society and its participating institutes, the Max Planck Institute for Astronomy, Heidelberg and the Max Planck Institute for Extraterrestrial Physics, Garching, The Johns Hopkins University, Durham University, the University of Edinburgh, the Queen's University Belfast, the Harvard-Smithsonian Center for Astrophysics, the Las Cumbres Observatory Global Telescope Network Incorporated, the National Central University of Taiwan, the Space Telescope Science Institute, the National Aeronautics and Space Administration under grant No. NNX08AR22G issued through the Planetary Science Division of the NASA Science Mission Directorate, the National Science Foundation grant No. AST-1238877, the University of Maryland, Eotvos Lorand University (ELTE), the Los Alamos National Laboratory, and the Gordon and Betty Moore Foundation.

Appendix A
The Data

A.1. Radio Data

Given that the sources in Gupta et al. (2018) are from the Northern as well as Southern Hemisphere, radio data were collected from two catalogs: NVSS (Condon et al. 1998) and SUMSS (Bock et al. 1999; Mauch et al. 2003). Both are characterized by similar sensitivity (∼2.5 mJy) and resolution (45″ FWHM for NVSS and $45\times 45\,\mathrm{cosec}\,|\delta|$ arcsec^2 for SUMSS). NVSS, a 1.4 GHz continuum survey, covers the northern sky from −40° decl. while SUMSS, a wide-field radio imaging survey conducted at 843 MHz, covers the southern sky from −30° decl., so together they map the whole sky. In addition, we decided to include one more catalog, FIRST (Becker et al. 1995). This 1.4 GHz sky survey is distinguished by its high resolution (5.″4) and its sensitivity down to 1 mJy radio flux. It covers a piece of the sky surveyed by NVSS, and therefore having detections in both of these catalogs helps to determine whether the source is compact or extended, but also to examine the accurate sizes of compact sources (see Appendix B for more details).

For NVSS and SUMSS data, a search within a matching radius of 3′ was conducted. For those sources where a single association was found, its exact location was checked—whether the radio match is located within 30″ from the optical center, and if so, this match was assigned to the object. The same procedure was adopted for FIRST data with the only difference being the internal matching radius of 5″ instead of 30″. All the sources having more than one radio association within a matching radius of 3′ were checked by eye. This part was done through visual inspection of radio maps with a size of $0.^\circ45\times 0.^\circ45$ extracted from NVSS,[14] SUMSS,[15] and FIRST[16] by using the NRAO Astronomical Image Processing System[17] package. In order to avoid false associations of radio matches, we downloaded the images from DSS1 and DSS2, which are digitized versions of several photographic astronomical surveys, in addition to radio maps, which can be found at the ESO archive.[18] Comparison of radio and optical sources on maps from both domains, together with the NASA/IPAC Extragalactic Database,[19] enabled us to distinguish incorrect matches. As some sources turned out to have extremely extended, i.e., beyond 3′, radio structures we were gradually increasing the radio search by 1′ as long as the association for the whole structure was found. Once the whole radio-emitting region was identified, the radio flux of each of the components was summed up and assigned to the given source. For sources lacking radio detections, we assigned them upper limits corresponding to the value of the sensitivity of the survey that contains the source in its footprint. While the sensitivity of NVSS and SUMSS is the same, for objects located in the area covered by both NVSS and FIRST, we decided on FIRST upper limits, as its sensitivity is lower than that of NVSS.

Because the radio catalogs we used were conducted at two different frequencies, the radio fluxes at 843 MHz were recalibrated to 1.4 GHz using a radio spectral index of $\alpha_r = 0.8$ (with the convention of $F_\nu \propto \nu^{-\alpha}$) so that the rest of our calculations are consistent.

A.2. Mid-infrared Data

The mid-infrared measurements were taken from the AllWISE Data Release (Cutri et al. 2013) which, by combining data from the cryogenic WISE (Wright et al. 2010) and post-cryogenic NEOWISE ("near-Earth object + WISE," Mainzer et al. 2011) survey phases, resulted in a comprehensive view of the mid-infrared sky. Out of four available bands (at 3.4, 4.6, 12, and 22 μm, corresponding to the W1, W2, W3, and W4 bands, respectively), we decided to make use of the W3 band, which was driven by the fact that at this specific wavelength the

[14] http://www.cv.nrao.edu/nvss/postage.shtml
[15] http://www.astrop.physics.usyd.edu.au/cgi-bin/postage.pl
[16] https://third.ucllnl.org/cgi-bin/firstcutout
[17] http://www.aips.nrao.edu/
[18] http://archive.eso.org/dss/dss
[19] https://ned.ipac.caltech.edu/

dusty torus is transparent enough to observe radiation coming directly from the central region of an AGN. At the shorter wavelengths of the W1 and W2 bands, the dusty, circumnuclear tori are optically thick and radiate anisotropically (Hönig et al. 2011; Netzer 2015). At the longer wavelengths of the W4 band, the dusty torus becomes even more transparent, but its measurements are affected by much larger errors than in W3 because (1) the W4 band traces the warm dust continuum at 22 μm and can be contributed to by starbursts (Ichikawa et al. 2019); (2) the sensitivity in the W4 band is much lower than in the W3 band and its signal-to-noise ratio is the lowest of all the WISE channels, resulting in a lower detected fraction for the objects in our sample; and (3) the resolution of W4 images is worse than in other bands (e.g., 12″ in W4 versus 6.″5 in W3), so for some of our sources (point like in optical, with close neighbors), W4 images could be blended.

Searching for counterparts was conducted within a radius of 5″, which allowed for the avoidance of false matches as the angular resolution of WISE in the W3 band is 6.″5.

The conversion from W3 magnitude, $m_{\rm W3}$, to the monochromatic flux, $F_{\nu_{\rm W3}}$, was done following the formula provided by Wright et al. (2010), given as $F_{\nu_{\rm W3}} = 30.922 \times 10^{(-m_{\rm W3}/2.5)}$.

Appendix B
Size Estimation for Compact AGNs

The radio catalogs we used differ significantly not only in their angular resolutions, and consequently in the accuracy of their fitted deconvolved angular sizes, but also in the data provided for unresolved objects. In NVSS, the angular size is estimated for each object, either as an exact measurement or an upper limit. However, in the case of FIRST and SUMSS, for unresolved sources, a size of 0.″0 is assigned. Therefore, the smallest resolved size listed in each of these catalogs, i.e., 0.″01 and 17.″3 for FIRST and SUMSS, respectively, was taken as an upper limit for unresolved objects detected in these catalogs. Additionally, as was already mentioned in Section 3.1, within a group of 57 compact sources for which data in NVSS and FIRST were available, (1) the angular sizes from NVSS are on average 15 times bigger than those taken from FIRST, and (2) all but five objects are resolved in FIRST (52/57) and only eight are resolved in NVSS (8/57).

Taking into account the above, we decided to use the following procedure to obtain sizes for compact sources:

1. for sources having both NVSS and SUMSS measurements, the NVSS size was adopted (eight sources);
2. for sources having both NVSS and FIRST measurements, the FIRST size estimate was adopted (57 sources); and
3. there are 13 sources with detections only in FIRST, 96 with detections only in NVSS, and 31 with detections only in SUMSS.

Appendix C
Optical Data for Host Galaxy Classification

Optical images for sources in our sample were collected from the following resources: HST through the Hubble Legacy Archive,[20] SDSS Data Release 14 (DR14, Abolfathi et al. 2018) through the ImgCutout Web Service,[21] and Pan-STARRS (Chambers et al. 2016) through the Image Cutout Server.[22] For galaxies that did not have images available in any of those services, we examined (mostly NIR) images retrieved from the ESO Archive Science Portal.[23]

Similarly to radio data, here we also make use of data differing in angular resolution, optical filter, and sensitivity to extended emission, deciding that the most and the least advantageous information are retrieved from HST and Pan-STARRS data, respectively. This translates to the "importance" of the data in the order of HST as the most reliable, SDSS, and Pan-STARRS as the most uncertain. Objects with data taken from ESO archives are excluded from this "sequence" as (1) they are found in only one resource, and (2) their classification is based on mainly NIR, not optical, images.

Knowing about the origin of the data and based on how many details of the host galaxy can be determined, how accurate the optical images are, and how many of them were available for a given source, we introduced the reliability flag describing the qualitative confidence of our classification. Five groups correspond to the following:

(1) when the optical images from all three resources were available and the morphology type is obvious and the same in all of them,
(2) when the optical images from one or two optical resources were available and the morphology type is obvious and the same in all of them,
(3) when the optical images from two or three resources were available and the morphology type differs between them and is well defined in the image coming from the most credible resource,
(4) when the optical images from two or three resources were available and the morphology type differs between them and is unreliable in the image coming from the most credible resource,
(5) when the optical images from one or two resources were available and the morphology type seen there is doubtful.

[20] http://hla.stsci.edu/hlaview.html
[21] http://skyservice.pha.jhu.edu/dr14/ImgCutout/ImgCutout.asmx
[22] https://ps1images.stsci.edu/cgi-bin/ps1cutouts
[23] http://archive.eso.org/scienceportal/

Table C1
The Qualitative Confidence of the Host Galaxy Morphology Classification for 248 AGNs from Our Sample

Reliability	Host Galaxy Morphology					Total
	Elliptical	Lenticular	Spiral	Distorted	Merger	
0	3		18	6	1	28
1	41	2	94	29*	6	172
2	4		4	5		13
3	4	2	1	2		9
4	10	2	9	5		26
Total	62	6	126	47	7	248

Note. The source attributed to the irregular group is indicated by a star.

In general, the reliability of our classification decreases in each of the above groups as it is based on less solid information. Sources with ESO data are assigned to groups 1 or 4 only.

The exact numbers of AGNs flagged as described above are presented in Table C1. A small fraction of all the objects with defined host galaxy morphology belongs to the last three groups corresponding to those with the least reliability (48 out of 248). The classification of most of the sources seem to be quite robust (200 out of 248), although optical images from all three resources exhibiting the same morphological type were only available for a few of them (28 AGNs).

Appendix D
The Sample

Table D1 lists the most important information obtained and discussed in this work for some of the sources in our sample of Swift/BAT AGNs. The complete sample is available as supplementary material.

Table D1
Swift/BAT Sample of 314 AGNs Used in This Study

SWIFT Name	Counterpart Name	z	$\log M_{\rm BH}$ ($M_\odot$)	$\log L_{\rm bol}$ (erg s^{-1})	$\log \lambda_{\rm Edd}$	Radio Flag[a]	$F_{1.4}$ (mJy)	R	Radio Class[b]	Size (kpc)	$\log(P_{\rm j}/L_{\rm bol})$	Radio Morphology[c]	FR[d]	Host Flag[e]	Host Morphology[f]
J1940.4-3015	IGR J19405–3016	0.0525	8.72	45.08	−1.75	N	9.6	−0.94	RQ	28.96[g]	<−3.69	C		P	S
J1952.4+0237	3C 403	0.0584	8.90	45.15	−1.85	N	6045.4	1.88	RL	167.91	−1.06	X	II	H	L
J1959.4+4044	Cygnus A	0.0558	9.29	45.33	−2.06	N	1598189.0	4.09	RL	104.65	0.60	D	II	H	E
J2001.0-1811	2MASX J20005575–1810274	0.0372	8.57	45.27	−1.40	U	2.5	−2.03	RQ					H	L
J2018.4-5539	PKS 2014–55	0.0607	8.86	45.05	−1.91	S	1597.5	1.44	RL	1367.75	−0.73	T	I	E	E
J2030.2-7532	IRAS 20247–7542	0.114	9.02	46.09	−1.03	S	8.6	−1.29	RQ	35.80[g]	<−4.10	C			
J2033.4+2147	4C +21.55	0.174	9.17	45.73	−1.54	N	1940.1	1.82	RL	544.32	−1.09	T	II	P	D
J2040.2-5126	ESO 234–IG 063	0.0541	8.60	45.01	−1.68	S	28.2	−0.38	RQ	18.21[g]	<−3.35	C		E	D
J2042.3+7507	4C +74.26	0.105	9.32	45.90	−1.52	N	1894.0	1.16	RL	1140.84	−1.27	T	II		
J2044.2-1045	Mrk 509	0.0344	8.72	45.19	−1.63	N	18.6	−1.15	RQ	15.42	<−4.05	C		H	S
J2052.0-5704	IC 5063	0.0115	8.56	44.74	−1.92	S	1448.5	0.23	RI	9.53	<−2.99	K		H	E
J2109.2+3531	B2 2107+35A	0.202	9.30	45.88	−1.52	N	1434.4	1.69	RL	344.87	<−1.06	K			
J2114.4+8206	2MASX J21140128+8204483	0.0833	8.87	45.41	−1.57	N	474.9	0.84	RI	308.21	−2.05	T	I	P	E
J2116.3+2512	2MASX J21161028+2517010	0.153	8.62	45.05	−1.67	U	2.5	−0.51	RQ						
J2118.9+3336	2MASX J21192912+3332566	0.0509	8.69	44.33	−2.46	N	3.7	−0.63	RQ	138.17[g]	<−2.91	C		P	E
J2134.9-2729	2MASX J21344509–2725557	0.0667	8.74	45.00	−1.84	N	7.8	−0.74	RQ	118.52	<−3.16	C		P	S_i
J2135.5-6222	1RXS J213623.1–622400	0.059	8.72	45.17	−1.65	S	4.3	−1.28	RQ	19.74[g]	<−4.08	C			
J2137.8-1433	PKS 2135–14	0.2	9.19	45.95	−1.34	N	3864.0	2.04	RL	365.62	−0.78	D	II		
J2145.5+1101	RX J2145.5+1102	0.209	8.73	45.25	−1.57	F	1.1	−0.77	RQ	16.66	<−3.67	C			
J2150.2-1855	6dF J2149581–185924	0.158	8.68	45.26	−1.53	N	528.4	1.64	RL	220.81	<−1.11	C			
J2157.2-6942	PKS 2153-69	0.0283	8.81	44.21	−2.71	S	29203.8	2.86	RL	37.42	−0.33	T	II	H	E
J2200.9+1032	Mrk 520	0.0275	8.54	44.78	−1.86	F	60.8	−0.42	RQ	1.57	<−3.97	C		S	D
J2204.7+0337	2MASX J22041914+0333511	0.0611	8.89	45.58	−1.41	F	8.8	−1.35	RQ	0.01[g]	<−6.08	C		S	D
J2209.1-2747	NGC 7214	0.0227	8.87	44.38	−2.59	N	28.2	−0.52	RQ	13.66	<−3.42	C		P	S
J2214.2-2557	2MASX J22140917–2557487	0.0519	8.70	44.36	−2.45	N	3.1	−0.72	RQ	60.34[g]	<−3.19	C		P	S
J2217.0+1413	Mrk 304	0.0704	8.96	45.26	−1.80	U	2.5	−1.44	RQ						
J2223.9-0207	3C 445	0.0601	8.54	45.43	−1.21	N	5783.9	1.60	RL	660.07	−1.15	X	II		
J2226.8+3628	MCG +06-49-019	0.0213	8.61	43.64	−3.07	N	7.0	−0.44	RQ	18.96[g]	<−3.13	C		S	S
J2234.8-2542	ESO 533–G 050	0.0265	8.67	43.53	−3.24	U	2.5	−0.59	RQ					P	S
J2235.9+3358	NGC 7319	0.0227	8.63	44.28	−2.44	N	53.0	−0.15	RQ	34.71	<−2.87	C		H	S_i
J2246.0+3941	3C 452	0.0811	8.79	44.96	−1.93	N	10556.6	2.62	RL	316.76	−0.40	T	II	H	E
J2248.7-5109	2MASX J22484165–5109338	0.1	8.52	45.34	−1.28	U	2.5	−1.20	RQ						

Notes. This subset of the table demonstrates format and content.
[a] Origin of the radio flux: N—NVSS; S—SUMSS; F—FIRST; U—undetected.
[b] RL—radio loud; RI—radio intermediate; RQ—radio quiet.
[c] X—complex; T—triple; D—double; K—knotty; C—compact.
[d] Our Fanaroff–Riley classification for lobed sources only.
[e] Origin of the host morphology classification: H—HST; S—SDSS; P—Pan-STARRS; E—ESO.
[f] E—elliptical; L—lenticular; S—spiral; D—distorted; Irr—irregular; M—merger. The subscript "i" indicates interacting galaxies.
[g] Compact unresolved sources for which their angular sizes equal the upper limits obtained from a given catalog (Appendix B).

(This table is available in its entirety in machine-readable form.)

ORCID iDs

Katarzyna Rusinek https://orcid.org/0000-0002-6424-6558
Dorota Kozieł-Wierzbowska https://orcid.org/0000-0003-4323-0984

References

Abolfathi, B., Aguado, D. S., Aguilar, G., et al. 2018, ApJS, 235, 42
Avara, M. J., McKinney, J. C., & Reynolds, C. S. 2016, MNRAS, 462, 636
Bassani, L., Venturi, T., Molina, M., et al. 2016, MNRAS, 461, 3165
Becker, R. H., White, R. L., & Helfand, D. J. 1995, ApJ, 450, 559
Begelman, M. C. 1995, PNAS, 92, 11442
Beskin, V. S., Kuznetsova, I. V., & Rafikov, R. R. 1998, MNRAS, 299, 341
Best, P. N., Kauffmann, G., Heckman, T. M., et al. 2005, MNRAS, 362, 25
Bird, J., Martini, P., & Kaiser, C. 2008, ApJ, 676, 147
Bisnovatyi-Kogan, G. S., & Lovelace, R. V. E. 2007, ApJL, 667, L167
Bisnovatyi-Kogan, G. S., & Ruzmaikin, A. A. 1976, Ap&SS, 42, 401
Blandford, R., Meier, D., & Readhead, A. 2019, ARA&A, 57, 467
Bock, D. C. J., Large, M. I., & Sadler, E. M. 1999, AJ, 117, 1578
Bruni, G., Panessa, F., Bassani, L., et al. 2019, ApJ, 875, 88
Cao, X., & Lai, D. 2019, MNRAS, 485, 1916
Chambers, K. C., Magnier, E. A., Metcalfe, N., et al. 2016, arXiv:1612.05560
Chiueh, T., Li, Z.-Y., & Begelman, M. C. 1998, ApJ, 505, 835
Chokshi, A., & Turner, E. L. 1992, MNRAS, 259, 421
Condon, J. J., Cotton, W. D., Greisen, E. W., et al. 1998, AJ, 115, 1693
Contopoulos, I., & Kazanas, D. 1998, ApJ, 508, 859
Contopoulos, I., Nathanail, A., Sądowski, A., Kazanas, D., & Narayan, R. 2018, MNRAS, 473, 721
Cutri, R. M., et al. 2013, yCat, 2328, 0
Duncan, R. A., & Sproats, L. N. 1992, PASAu, 10, 16
Elvis, M., Risaliti, G., & Zamorani, G. 2002, ApJL, 565, L75
Fanaroff, B. L., & Riley, J. M. 1974, MNRAS, 167, 31P
Fanidakis, N., Baugh, C. M., Benson, A. J., et al. 2011, MNRAS, 410, 53
Fanidakis, N., Baugh, C. M., Benson, A. J., et al. 2012, MNRAS, 419, 2797
Garofalo, D. 2009a, ApJL, 699, L52
Garofalo, D. 2009b, ApJ, 699, 400
Garofalo, D., Evans, D. A., & Sambruna, R. M. 2010, MNRAS, 406, 975
Garofalo, D., North, M., Belga, L., & Waddell, K. 2020, ApJ, 890, 144
Goodman, J. 2003, MNRAS, 339, 937
Graham, A. W. 2007, MNRAS, 379, 711
Guilet, J., & Ogilvie, G. I. 2012, MNRAS, 424, 2097
Guilet, J., & Ogilvie, G. I. 2013, MNRAS, 430, 822
Gupta, M., Sikora, M., & Rusinek, K. 2020, MNRAS, 492, 315
Gupta, M., Sikora, M., Rusinek, K., & Madejski, G. M. 2018, MNRAS, 480, 2861
Hardcastle, M. J., & Krause, M. G. H. 2013, MNRAS, 430, 174
Hönig, S. F., Leipski, C., Antonucci, R., & Haas, M. 2011, ApJ, 736, 26
Hure, J. M., Collin-Souffrin, S., Le Bourlot, J., & Pineau des Forets, G. 1994, A&A, 290, 19
Ichikawa, K., Ricci, C., Ueda, Y., et al. 2019, ApJ, 870, 31
Inoue, Y., Doi, A., Tanaka, Y. T., Sikora, M., & Madejski, G. M. 2017, ApJ, 840, 46
Kapahi, V. K., Athreya, R. M., Subrahmanya, C. R., et al. 1998a, ApJS, 118, 327
Kapahi, V. K., Athreya, R. M., van Breugel, W., McCarthy, P. J., & Subrahmanya, C. R. 1998b, ApJS, 118, 275
Kellermann, K. I., Sramek, R., Schmidt, M., Shaffer, D. B., & Green, R. 1989, AJ, 98, 1195
Khrykin, I. S., Hennawi, J. F., & Worseck, G. 2019, MNRAS, 484, 3897
Koss, M., Trakhtenbrot, B., Ricci, C., et al. 2017, ApJ, 850, 74
Koutsantoniou, L. E., & Contopoulos, I. 2014, ApJ, 794, 27
Kozieł-Wierzbowska, D., & Stasińska, G. 2011, MNRAS, 415, 1013
Kratzer, R. M., & Richards, G. T. 2015, AJ, 149, 61
Lacy, M., Ridgway, S. E., Sajina, A., et al. 2015, ApJ, 802, 102
Lubow, S. H., Papaloizou, J. C. B., & Pringle, J. E. 1994, MNRAS, 267, 235
Lyubarsky, Y., & Eichler, D. 2001, ApJ, 562, 494
Madrid, J. P., Chiaberge, M., Floyd, D., et al. 2006, ApJS, 164, 307
Mahlmann, J. F., Levinson, A., & Aloy, M. A. 2020, MNRAS, 494, 4203
Mainzer, A., Bauer, J., Grav, T., et al. 2011, ApJ, 731, 53
Marconi, A., & Hunt, L. K. 2003, ApJL, 589, L21
Mauch, T., Murphy, T., Buttery, H. J., et al. 2003, MNRAS, 342, 1117
McKinney, J. C., Tchekhovskoy, A., & Blandford, R. D. 2012, MNRAS, 423, 3083
McLure, R. J., & Jarvis, M. J. 2004, MNRAS, 353, L45
Narayan, R., Igumenshchev, I. V., & Abramowicz, M. A. 2003, PASJ, 55, L69
Netzer, H. 2015, ARA&A, 53, 365
Nilsson, K. 1998, A&AS, 132, 31
Panessa, F., Baldi, R. D., Laor, A., et al. 2019, NatAs, 3, 387
Panessa, F., Bassani, L., Landi, R., et al. 2016, MNRAS, 461, 3153
Rafter, S. E., Crenshaw, D. M., & Wiita, P. J. 2009, AJ, 137, 42
Rafter, S. E., Crenshaw, D. M., & Wiita, P. J. 2011, AJ, 141, 85
Reynolds, C. S., Garofalo, D., & Begelman, M. C. 2006, ApJ, 651, 1023
Ricci, C., Trakhtenbrot, B., Koss, M. J., et al. 2017, ApJS, 233, 17
Rothstein, D. M., & Lovelace, R. V. E. 2008, ApJ, 677, 1221
Rusinek, K., Sikora, M., Kozieł-Wierzbowska, D., & Godfrey, L. 2017, MNRAS, 466, 2294
Sandage, A. 1965, ApJ, 141, 1560
Schawinski, K., Koss, M., Berney, S., & Sartori, L. F. 2015, MNRAS, 451, 2517
Schmidt, M. 1963, Natur, 197, 1040
Schmidt, T. M., Hennawi, J. F., Worseck, G., et al. 2018, ApJ, 861, 122
Schulze, A., Done, C., Lu, Y., Zhang, F., & Inoue, Y. 2017, ApJ, 849, 4
Shabala, S. S., & Godfrey, L. E. H. 2013, ApJ, 769, 129
Sikora, M., & Begelman, M. C. 2013, ApJL, 764, L24
Sikora, M., Stasińska, G., Kozieł-Wierzbowska, D., Madejski, G. M., & Asari, N. V. 2013, ApJ, 765, 62
Sikora, M., Stawarz, Ł., & Lasota, J.-P. 2007, ApJ, 658, 815
Skrutskie, M. F., Cutri, R. M., Stiening, R., et al. 2006, AJ, 131, 1163
Small, T. A., & Blandford, R. D. 1992, MNRAS, 259, 725
Smith, K. L., Mushotzky, R. F., Koss, M., et al. 2020, MNRAS, 492, 4216
Smith, K. L., Mushotzky, R. F., Vogel, S., Shimizu, T. T., & Miller, N. 2016, ApJ, 832, 163
Soltan, A. 1982, MNRAS, 200, 115
Tadhunter, C. 2016, A&ARv, 24, 10
Tchekhovskoy, A., & McKinney, J. C. 2012, MNRAS, 423, L55
Tchekhovskoy, A., McKinney, J. C., & Narayan, R. 2012, JPhCS, 372, 012040
Tchekhovskoy, A., Narayan, R., & McKinney, J. C. 2011, MNRAS, 418, L79
Ünal, C., & Loeb, A. 2020, MNRAS, 495, 278
van Velzen, S., & Falcke, H. 2013, A&A, 557, L7
Volonteri, M., Sikora, M., & Lasota, J.-P. 2007, ApJ, 667, 704
Volonteri, M., Sikora, M., Lasota, J. P., & Merloni, A. 2013, ApJ, 775, 94
Willott, C. J., Rawlings, S., Blundell, K. M., & Lacy, M. 1999, MNRAS, 309, 1017
Wilson, A. S., & Colbert, E. J. M. 1995, ApJ, 438, 62
Wolf, M. J., & Sheinis, A. I. 2008, AJ, 136, 1587
Wright, E. L., Eisenhardt, P. R. M., Mainzer, A. K., et al. 2010, AJ, 140, 1868
Yu, Q., & Tremaine, S. 2002, MNRAS, 335, 965
Yuan, Y., Spitkovsky, A., Blandford, R. D., & Wilkins, D. R. 2019, MNRAS, 487, 4114
Zhu, Z., & Stone, J. M. 2018, ApJ, 857, 34

4 Paper III: The dependence of the fraction of radio luminous quasars on redshift and its theoretical implications

In Rusinek-Abarca and Sikora (2021) we investigated how the radio-loud fraction (RLF) of quasars changes with cosmic time, and therefore conducted a thorough analysis of the RLF in relation to redshift, BH mass, and Eddington ratio.

By taking a similar approach as in Rusinek et al. (2020), in the first step, we selected objects from the radio catalog LoTSS, which, thanks to its low frequency coverage ($120 - 168$ MHz) and exceptionally high sensitivity, has many AGNs with radio detections in its database. Applying the constraint on BH masses ($M_{\rm BH} \geq 10^{8.5} M_{\odot}$), we further distinguished three subsets in the specific redshift range ($0.7 \leq z < 1.9$) which provided uniform calculations for BH masses and bolometric luminosities. In this part of the work we noted a decrease in RLF with an increase in redshift.

In the next step, the dependence of the RLF on the BH mass and Eddington ratio was examined. This was accomplished by removing the bias implied by the dependence of RLF on redshift by narrowing its range ($0.5 \leq z < 0.7$), which, as earlier, resulted in consistent estimations of BH masses (again, with the removal of the less massive systems) and bolometric luminosities. As the sample analyzed in the first part of this work was not numerous enough at smaller redshifts (at which more sources have known nuclear properties), another set was chosen consisting of QSOs from the SDSS DR7 catalog, to which the radio data (from FIRST at 1.4 GHz) was carefully reassigned. This allowed for a detailed investigation of the dependence of the RLF on BH mass and Eddington ratio with the finding of an increase in RLF with an increase in $M_{\rm BH}$ and no relationship between the RLF and $\lambda_{\rm Edd}$. That implies an even steeper decline in RLF with redshift than concluded without counting the dependence of the RLF on $M_{\rm BH}$.

Finally, we made an attempt at linking these findings with possible scenarios for MAD formation, especially focusing on the types of galaxy mergers being responsible for triggering AGN activity.

The Astrophysical Journal, 922:202 (11pp), 2021 December 1 https://doi.org/10.3847/1538-4357/ac2429

The Dependence of the Fraction of Radio Luminous Quasars on Redshift and its Theoretical Implications

Katarzyna Rusinek-Abarca and Marek Sikora
Nicolaus Copernicus Astronomical Center, Polish Academy of Sciences, Bartycka 18, 00-716 Warsaw, Poland; krusinek@camk.edu.pl
Received 2021 May 25; revised 2021 September 2; accepted 2021 September 3; published 2021 November 30

Abstract

While radio emission in quasars can be contributed to by a variety of processes (involving star-forming regions, accretion disk coronas and winds, and jets), the powering of the radio loudest quasars must involve very strong jets, presumably launched by the Blandford–Znajek mechanism incorporating the magnetically arrested disk (MAD) scenario. We focus on the latter and investigate the dependence of their fraction on redshift. We also examine the dependence of the radio-loud fraction (RLF) on BH mass ($M_{\rm BH}$) and Eddington ratio ($\lambda_{\rm Edd}$), while excluding the redshift bias by narrowing its range. In both of these investigations, we remove the bias associated with: (1) the diversity of source selection by constructing two well-defined, homogeneous samples of quasars (first within $0.7 \leqslant z \leqslant 1.9$, second within $0.5 \leqslant z \leqslant 0.7$); and (2) a strong drop in the RLF of quasars at smaller BH masses by choosing those with BH masses larger than $10^{8.5} M_{\odot}$. We confirm some of the previous results showing the increase in the fraction of radio-loud quasars with cosmic time and that this trend can be even steeper if we account for the bias introduced by the dependence of the RLF on BH mass, whereas the bias introduced by the dependence of the RLF on Eddington ratio is shown to be negligible. Assuming that quasar activities are triggered by galaxy mergers, we argue that such an increase can result from the slower drop with cosmic time of mixed mergers than of wet mergers.

Unified Astronomy Thesaurus concepts: Radio active galactic nuclei (2134); Quasars (1319); Radio jets (1347); Non-thermal radiation sources (1119)

Supporting material: machine-readable table

1. Introduction

As recent studies suggest, the quasi-steady production of strong, relativistic jets in certain quasars over 10^7–10^8 yr (e.g., Bird et al. 2008), with some jet powers approaching their accretion power (van Velzen & Falcke 2013; Inoue et al. 2017; Rusinek et al. 2017), may require the formation of magnetically arrested disks (MADs). Their formation takes place if the net accumulated magnetic flux exceeds the maximal amount that can be confined on the black hole by the accretion flow (Bisnovatyi-Kogan & Ruzmaikin 1976; Narayan et al. 2003; Igumenshchev 2008; McKinney et al. 2012). However, the proposed scenarios that build up MADs and explain why they occur in only a fraction of quasars remain in the realm of speculation. Their uncertainties are mainly associated with our poor knowledge about the magnetic properties (i.e., intensities, topology, and diffusivity) of accretion flows and their dependence on initial conditions that trigger quasar activity (see, e.g., Begelman 1995; Beckwith et al. 2008). The most widely accepted scenarios include:

(A) The possibility of building-up the MAD by the advection of the poloidal magnetic fields by accretion flows (Lubow et al. 1994; Spruit & Uzdensky 2005; Bisnovatyi-Kogan & Lovelace 2007; Rothstein & Lovelace 2008; Beckwith et al. 2009; Guilet & Ogilvie 2012, 2013; Cao 2016; Cao & Lai 2019);
(B) The formation of the MAD in situ, such as via the "cosmic battery" (Contopoulos & Kazanas 1998; Koutsantoniou & Contopoulos 2014);
(C) The survival of the MAD, formed during the thick, hot, very low accretion rate phase, during the transition to the quasar phase (Sikora et al. 2013; Sikora & Begelman 2013).

Observationally, one can try to confront these scenarios by studying the differences between multiband spectra of radio-loud (RL) and radio-quiet (RQ) quasars, the differences between properties of their hosts and environments, and the dependence of the radio-loud fraction (RLF) of quasars on redshift.

The most striking result of comparing the radiative properties of quasars is that the spectral energy distributions (SEDs) of RL and RQ quasars are very similar (e.g., Elvis et al. 1994; Richards et al. 2006; de Vries et al. 2006; Shang et al. 2011; Shankar et al. 2016). Statistically significant differences are only noticed in the X-ray bands. In particular, RLQs are found to be on average X-ray louder and with X-ray spectra harder than RQQs. Although the X-ray hardness may result from the dependence of the X-ray spectra slopes on the Eddington ratio and the lower average Eddington ratio of RL quasars than of RQ quasars, the difference in the X-ray loudness requires something else. Assuming that the production of X-rays is powered by reconnection of magnetic fields in accretion disk coronas (Beloborodov 2017; Sironi & Beloborodov 2020), the efficiency of X-ray production in the vicinity of the BH is likely to be differentiated by the presence/absence of the MAD. Obviously, structures of the innermost portions of accretion flows also depend on values of BH spin. However, noting that many radio-quiet AGNs have very large spins (Reynolds 2019, and refs. therein), the precise value of the spin is not expected to be directly correlated with the X-ray production efficiency. Hence, the similarity of SEDs between RL and RQ quasars for similar Eddington ratios, BH masses,

and spins precludes the existence of MAD from being dependent on the current accretion parameters.

Contrary to the radiative properties, severe differences between RL and RQ quasars are established regarding their hosts and environment, the main ones being:

1. In contrast to RQ quasars, which are found to be hosted by both, elliptical (E) and spiral (Sp) galaxies, the vast majority of RL quasars are hosted by giant ellipticals (gE; e.g., Floyd et al. 2010; Tadhunter 2016; Rusinek et al. 2020);
2. The RL quasars are located in denser environments and have on average much more massive dark matter halos than RQ quasars (e.g., Mandelbaum et al. 2009; Shen 2009; Donoso et al. 2010; Wylezalek et al. 2013; Retana-Montenegro & Röttgering 2017).

Adopting the premise that the triggering of the high accretion events represented by the quasar phenomenon is associated with galactic mergers (e.g., Shen 2009; Bessiere et al. 2012; Treister et al. 2012), one might expect that almost all radio-loud quasars and some fraction of radio-quiet quasars are triggered by mergers of massive elliptical galaxies with disk galaxies, while the remaining RQ quasars formed from mergers of two disk galaxies. Within this scheme, the question remains: what decides the quasar radio-loudness following the merger of a massive elliptical galaxy with a disk galaxy? As was argued by Rusinek et al. (2020), this can be explained by involving the "cosmic-battery" scenario of MAD formation, provided that the merger leads to a BH system that is either corotating or counterrotating, while satisfying the stability criterion derived by King et al. (2005). However, such a duality can also be achieved within the 'C' scenario because not all MADs that formed during the geometrically thick, hot, very low accretion rate phase of MAD can survive the transition of the object to the quasar phase (see Figure 5 in Rusinek et al. 2017).

The possible dependency of MAD formation on the type of galaxy mergers can be verified by comparing the cosmic history of different types of mergers with the dependence of RLF of quasars on redshift. As semi-analytical models indicate (Khochfar & Burkert 2003) and observations support (Lin et al. 2008), the fraction of E–Sp mergers decreases with increasing redshift, while the fraction of Sp–Sp mergers increases with redshift. Then, noting that the dominant fraction of RQ quasars is presumably triggered by the Sp–Sp mergers, while the vast majority of RL quasars—by E–Sp mergers, one might expect to have RLF decreasing with redshift. Unfortunately, the results of studies on such a dependence performed in the past often conflict (see, e.g., Stern et al. 2000; Jiang et al. 2007; Singal et al. 2011, 2013; Kratzer & Richards 2015). The reasons for this are biases associated with the radio and optical flux limits , which work differently for differently selected samples, and the choice of the demarcation value of the radio-loudness parameter used to divide quasars into radio-loud and radio-quiet categories.

To minimize the effects of these biases, we adopt the following strategy:

1. We study the dependence of the RLF on redshift for quasars selected from the sample analyzed by Gürkan et al. (2019), distinguishing three subsamples, altogether covering a redshift range of $0.7 \leqslant z < 1.9$ (see Section 2);
2. We investigate the dependence of the RLF on BH mass and Eddington ratio for a well-defined, homogeneous, and redshift-narrowed ($z \sim 0.6$, thus excluding the dependence of the RLF on the redshift) sample for quasars chosen from the catalog of Shen et al. (2011; see Section 3);
3. We define the RLF as the ratio of RL to the total number of sources, where RL objects are classified as those in which the radio emission is dominated by the presence of strong jets—most likely produced within the MAD scenario;
4. We choose in these samples those sources with BH masses larger than $10^{8.5} M_{\odot}$ to avoid bias associated with a large drop in the fraction of RLQ at smaller BH masses.

The theoretical interpretations of the anticorrelation of the RLF with redshift, the dependence of the RLF on BH mass, $M_{\rm BH}$, and lack thereof with regards to Eddington ratio, $\lambda_{\rm Edd}$, that we found are discussed in Section 4 (such a dependence is observed for QSOs with $\lambda_{\rm Edd} < 0.01$ and is caused by the decrease of the radiative efficiency of the accretion flows at such low Eddington ratios, Sikora et al. 2007). The main results of our work are summarized in Section 5.

Throughout this paper, we assume a ΛCDM cosmology with $H_0 = 70\,{\rm km\,s^{-1}\,Mpc^{-1}}$, $\Omega_m = 0.3$, and $\Omega_\Lambda = 0.70$.

2. The Dependence of Radio-loud Fraction of Quasars on Redshift

With a focus on performing a study of the radio-loud fraction of quasars on redshift, we decide to use sources from Gürkan et al. (2019), who collected 49 925 optically selected quasars for detailed radio analysis. The authors made use of the sensitive and high-resolution low-frequency radio data, for which the extended radio structures of an AGN (lobes, plumes, etc.) dominate the radio emission, while the Doppler boosting is minimized. Together with the wide range of redshifts, BH masses, and Eddington ratios that the objects analyzed by Gürkan et al. (2019) cover (see Table 3 and Figure 8 therein), their sample enabled us to construct a well-controlled and homogeneous population, a thorough description of which is given below.

Objects analyzed by Gürkan et al. (2019) are chosen from the SDSS-IV DR14 quasar catalog (DR14Q). Compiled from the extended Baryon Oscillation Spectroscopic Survey (eBOSS) of SDSS IV by Pâris et al. (2018), and based on works of Myers et al. (2015) and Blanton et al. (2017), DR14Q contains 526 356 quasars and provides redshifts, photometry in five bands, and information about broad absorption line quasars, as well as multiwavelength matching with large-area surveys when available.

Gürkan et al. (2019) focused on quasars from the Hobby-Eberly Telescope Dark Energy Experiment (HETDEX; Hill et al. 2008) Spring field and Herschel-Astrophysical Terahertz Large Area Survey/North Galactic Pole (H-ATLAS/NGP; Hardcastle et al. 2016) region for which data obtained by Low Frequency Array (LOFAR; van Haarlem et al. 2013) as a part of the LOFAR Two-meter Sky Survey (LoTSS; Shimwell et al. 2017) are accessible. The advantage of using LoTSS relates to its high sensitivity ($\sim 100\,\mu$Jy), which—combined with a resolution of $6''$ and the low frequency that it has been conducted at, i.e., 120–168 MHz—allows for the detection of the extended emissions that are often missed at the higher frequencies at which most of the commonly used radio surveys have been carried out (including the Faint Images of the Radio

Sky at Twenty-cm catalog that we used, see Section 3.1.3). Thereby, the sample analyzed by Gürkan et al. (2019) is the largest set of optically selected quasars detected at 144 MHz to date.

Based on the availability and the character of the LOFAR data, Gürkan et al. (2019) divide their quasars into those with and without radio detections, distinguishing compact and extended objects among the former. Unfortunately, we cannot use their classification for our analysis because this information is not provided elsewhere than within the figures presented in their work. From their Figure 4—which shows the radio-loudness distribution, with the radio-loudness parameter being the ratio of monochromatic luminosities at 144 MHz, $L_{\nu_{144}}$, to SDSS i-band, L_{ν_i}, in a logarithmic scale—we can see that while all radio-loud objects (corresponding to those with $L_{\nu_{144}}/L_{\nu_i} > 10^3$, in accordance to the division introduced by Kellermann et al. 1989, see Appendix A) have direct radio measurements, a significant fraction of radio-intermediate (RI, with values of $10^2 < L_{\nu_{144}}/L_{\nu_i} < 10^3$) objects lack direct radio measurements. Furthermore, one can note that sources with extended radio emission, albeit representing about 5% of all detected objects (865 out of 16 259), occupy quite a wide range of radio-loudness values, from 1 up to 10^4.

While selecting quasars from the sample of Gürkan et al. (2019), we decided on a redshift limit of $0.7 \leqslant z < 1.9$ and a BH mass cutoff of $M_{\rm BH} \geqslant 10^{8.5} M_\odot$. The first criterion provided us with a sufficiently large sample size (at lower redshifts the number of sources drops significantly) over a wide enough range of redshifts to perform our study, and (more importantly) was chosen to coincide with uniform calculations of BH masses and bolometric luminosities, $L_{\rm bol}$, which (within the given redshift range) are estimated from the Mg II line and monochromatic luminosity at 3000 Å (values of $M_{\rm BH}$ and $\lambda_{\rm Edd}$ were taken from Shen et al. 2011, and Kozłowski 2017).[1] The second constraint, as already explained, gives possibly the largest ratio of radio-loud to total objects within the sample—the sample contains 9 177 quasars.

We further split our sample into three groups on the basis of their redshift, $0.7 \leqslant z < 1.1$, $1.1 \leqslant z < 1.5$, and $1.5 \leqslant z < 1.9$, amounting to 2 172, 3 210, and 3 795 objects, respectively. The radio-loud fractions computed for each of these populations were found to be 3.64%, 2.65%, and 1.92%, accordingly, clearly decreasing with increasing redshift. The opposite happens with the medians of BH mass and Eddington ratio, which both increase with redshift.[2] The size of each sample, number of RL objects, median redshifts, BH masses, and Eddington ratios are provided in Table 1.

Table 1
Comparison of the Total Numbers of Sources and RL Objects only, RLF Values, Median Redshifts, BH Masses, and Eddington Ratios for three Samples Selected from Gürkan et al. (2019)

Sample	$N_{\rm total}$	$N_{\rm RL}$	RLF	$\tilde{z}$	$\log \tilde{M}_{\rm BH}[M_\odot]$	$\log \tilde{\lambda}_{\rm Edd}$
$0.7 \leqslant z < 1.1$	2 172	79	3.64%	0.93	8.79	−1.20
$1.1 \leqslant z < 1.5$	3 210	85	2.65%	1.31	8.89	−0.96
$1.5 \leqslant z < 1.9$	3 795	73	1.92%	1.69	8.95	−0.88

3. The Dependence of Radio-loud Fraction of Quasars on BH Mass and Eddington Ratio

Since the dependence of the radio-loud fraction of quasars on redshift can be affected not only by the distinct cosmic history of triggers of radio-loud and radio-quiet quasars but also by the dependence of the RLF on the BH mass and the Eddington ratio and the correlation of the median values of $M_{\rm BH}$ and $\lambda_{\rm Edd}$ with redshift (see Table 1), we decided to investigate this dependence in more detail. However, to conduct this study, the analyzed sample of sources has to be chosen from a very narrow redshift range while being quite numerous, especially regarding the ratio of radio-loud to total objects and with as few sources lacking radio data among those with the highest values of radio-loudness as possible. For these reasons, the previously analyzed subsamples from Gürkan et al. (2019) are not sufficient because their RLF is rather small and it drops even further when subject to narrower redshift ranges. Thus, a new sample of quasars located closer has been chosen —with a narrow range of redshift of $0.5 \leqslant z < 0.7$.

3.1. The Sample

3.1.1. Source Selection

The objects collected in our studied sample of quasars at $z \sim 0.6$ are initially taken from the catalog of quasar properties from Sloan Digital Sky Survey Data Release 7 (SDSS DR7), which was compiled by Shen et al. (2011) from works of Schneider et al. (2010) and Abazajian et al. (2009). Besides careful analysis of the continuum and emission line measurements around the Hα, Hβ, Mg II, and C IV regions, the authors also provide information about radio properties, flags indicating quasars with broad absorption lines or disk emitters, and black hole masses. We distinguish four main steps which lead to our final sample (hereinafter: 0.5–0.7 QSOs): narrowing the redshift range; checking whether BH masses and bolometric luminosities (and with those—Eddington ratios) are estimated in the same manner for all the objects; limiting BH masses; and choosing sources in the footprint of Faint Images of the Radio Sky at Twenty-cm (FIRST, Becker et al. 1995) catalog.

The catalog from Shen et al. (2011) gathers 105 783 quasars from within a wide range of redshifts (from the very nearby Universe up to $z = 5.5$). We select from them any quasars that are enclosed within a narrow range of redshifts of $0.5 \leqslant z < 0.7$[3], which leaves us with 7 306 objects. This restraint provides the following advantages: (1) it minimizes the redshift bias from the dependence of the RLF on BH mass and Eddington ratio; and (2) the chosen redshift range achieves a suitable trade-off between minimizing the biases stemming from the optical and radio flux limits, while avoiding a significant reduction in the sample size.

The previous constraint already indicates homogeneous data that should be used for the estimation of $M_{\rm BH}$ and $\lambda_{\rm Edd}$. We

[1] Even though we rejected sources with different estimations of $M_{\rm BH}$ and $L_{\rm bol}$ than mentioned here, we note that the calculations made by Shen et al. (2011) and Kozłowski (2017) may vary slightly. However, these discrepancies do not affect our further analysis because they are smaller than the reported uncertainties of $M_{\rm BH}$ and $L_{\rm bol}$, being ∼0.06 versus ∼0.4 dex and ∼0.01 versus ∼0.1 dex, respectively (see Kozłowski 2017 for more details).

[2] We checked that the trend was preserved while considering the effect of the measurement uncertainties of $M_{\rm BH}$ and $L_{\rm bol}$, which are typically about 0.4 and 0.1 dex, respectively. The uncertainty of $\lambda_{\rm Edd}$, being ∼0.41 dex, was obtained as described in Section 3.1.2.

[3] The redshifts used in our work are taken, just as in Shen et al. (2011), from the SDSS DR7 quasar catalog (Schneider et al. 2010). These values do not differ significantly from the more accurate data provided by Hewett & Wild (2010), and consequently do not affect our final sample size and the obtained results.

Table 2
Subsequent Steps Involved in Constructing our 0.5–0.7 QSOs Sample

Number of Objects	Constraint
105 783	Sample from Shen et al. (2011)
7 306	Redshift cutoff of $0.5 \leqslant z < 0.7$
7 209	Uniform calculation of $M_{\rm BH}$ and $\lambda_{\rm Edd}$
3 734	Limit of $M_{\rm BH} \geqslant 10^{8.5} M_{\odot}$
3 511	Objects within the FIRST footprint

verify this information (Section 3.1.2) and exclude quasars with measurements obtained differently which reduces the sample size by 97 sources.

In the next step, as in the sample from Gürkan et al. (2019), we limited the sample for $M_{\rm BH} \geqslant 10^{8.5} M_{\odot}$, which further restricts our sample to 3 734 objects.

Finally, because the subject of our research is to examine the radio-loud fraction of quasars, we reject all objects that are located outside of the FIRST footprint. Following this step, our final sample is 3 511 quasars. Our reasons for choosing FIRST as our main source of radio data and the way it was assigned to each quasar are explained in more detail in Section 3.1.3.

Table 2 summarizes how each of these steps contributed to the final size of the 0.5–0.7 QSOs sample.

3.1.2. Black Hole Mass, Bolometric Luminosity, and Eddington Ratio

As stated in Shen et al. (2011), the fiducial virial black hole mass for quasars at $z < 0.7$ is estimated from the broad Hβ line following the calibration provided by Vestergaard & Peterson (2006). Meanwhile, the bolometric luminosity for those quasars is computed from the monochromatic luminosity at 5100 Å using the spectral fits and bolometric corrections from Richards et al. (2006). We examined whether the sources that we collected follow these two conditions and rejected those whose $M_{\rm BH}$ and $L_{\rm bol}$ are obtained from other measurements, thus assuring that all of the calculations for our quasars are alike.

The BH masses of objects in our sample have values within the range of $8.5 \leqslant \log M_{\rm BH}\,[M_{\odot}] \leqslant 10.3$ with median of $\log \tilde{M}_{\rm BH}\,[M_{\odot}] = 8.81$. Uncertainties for each BH mass estimate are typically $\sigma_{\log M_{\rm BH}} \sim 0.4$ dex.

Because the bolometric luminosities provided by Shen (2009) are overestimated by including the contribution from infrared radiation (see Marconi et al. 2004 and footnote 19 in Shen et al. 2011), we reduce their bolometric luminosities by one third to account for this IR emission.

The values of $L_{\rm bol}$ for objects in our sample are within a range of $44.10 \leqslant \log L_{\rm bol}\,[{\rm erg\ s^{-1}}] \leqslant 47.09$ with a median of $\log \tilde{L}_{\rm bol}\,[{\rm erg\ s^{-1}}] = 45.54$. The typical uncertainty of the bolometric luminosity measurement is $\sigma_{\log L_{\rm bol}} \sim 0.1$ dex.

Finally, we compute the Eddington ratio, $\lambda_{\rm Edd} \equiv L_{\rm bol}/L_{\rm Edd}$, finding its values enclosed within the range of $-3.30 \leqslant \log \lambda_{\rm Edd} \leqslant -0.07$ with a median of $\log \tilde{\lambda}_{\rm Edd} = -1.39$. The typical uncertainty of the Eddington ratio is estimated as $\sigma_{\log \lambda_{\rm Edd}} = \sqrt{\sigma^2_{\log M_{\rm BH}} + \sigma^2_{\log L_{\rm bol}}}$, which gives ∼0.41 when using the typical uncertainties mentioned earlier.

3.1.3. Radio Data

Even though the radio properties are included in Shen et al. (2011), their procedure to assign radio data is not scrupulous enough with regard to the objective of our study, being particularly biased against extensive double structures. Consequently, we carry out the matching procedure following the strategy adopted by Rusinek et al. (2020).

We used the FIRST radio catalog, which was designed to overlap with the area of SDSS. This 1.4 GHz sky survey is characterized by its high resolution (5.″4) and its sensitivity down to 1 mJy.[4]

At first, we conducted a search within a matching radius of 1′ of the optical position. For sources where only one radio association was uncovered, if the radio location was found to be within 5″ of the optical position, then the match was confirmed and the object was designated as *"compact."* Objects with multiple associations were examined manually through visual inspection of radio maps with sizes of $0.^{\circ}45 \times 0.^{\circ}45$ extracted from FIRST.[5] If, from visual examination, it was determined that the object was not compact (i.e., multiple radio matches were found to be associated with the object), then the source was classified as *"extended."* Among them, we distinguish those in which a pair of lobes was determined, referring to them as *"lobed"* (regardless of the detection of the radio core). For quasars in which much more extended (i.e., beyond 1′) radio morphologies were noticed, the search for radio matches was gradually increased by 1′ until the whole structure was identified. The radio flux from each component was then summed up for every extended source.

Sources with nondetections were assigned an upper limit of 1 mJy, corresponding to the detection limit of FIRST.

Only 16% of 0.5–0.7 QSOs QSOs are radio detected (546 out of 3 511) and 31% of those reveal extended radio morphology (171 out of 546). The radio lobed objects constitute 80% of the radio extended ones (136 out of 171).[6]

3.2. Radio Loudness Distribution

To separate objects with powerful jets dominating the radio emission from those in which this emission is contributed to mainly from other processes, we use the radio-loudness parameter and define it as the ratio of monochromatic luminosities at 1.4 GHz, $L_{\nu_{1.4}}$, to, similarly to Gürkan et al. (2019), SDSS i-band, L_{ν_i}. In Appendix A, we present the general formula for the conversion of the radio-loudness parameter between various frequencies, referring to the definition introduced by Kellermann et al. (1989).

The radio-loudness distribution of our 0.5–0.7 QSOs is presented in the top panel of the Figure 1. Its values spread over four orders of magnitude, $-0.31 \leqslant \log(L_{\nu_{1.4}}/L_{\nu_i}) \leqslant 4.75$, with its peak at $\log(L_{\nu_{1.4}}/L_{\nu_i}) \sim 1.2$, which, as one can see, is strongly dominated by the radio-undetected sources that constitute the vast majority of the whole sample. Meanwhile, the radio-detected sources are much more evenly distributed over the whole range of radio-loudness, with the median being about 10 times higher than for the radio undetected ones (144.41 and 13.87, accordingly).

The bottom panel of Figure 1 shows the Kaplan-Meier estimator for the cumulative distribution function (CDF), $\hat{F}$,

[4] Despite the fact that FIRST has about 10 times worse sensitivity than LoTSS, it is deep enough to proceed with our study of quasars located at $z \sim 0.6$, for which radio structures above ∼33 kpc are resolved.

[5] http://sundog.stsci.edu/

[6] We note that our assignment and categorization of the FIRST radio data, despite being cautious, is more likely incomplete rather than contaminated with false associations because we reject any radio matches with unconvincing linkage to the quasar, which is exactly the opposite to the approach of Shen et al. (2011) who assigned all of the nearby (i.e., located within their 30′ matching radius) associations as authentic.

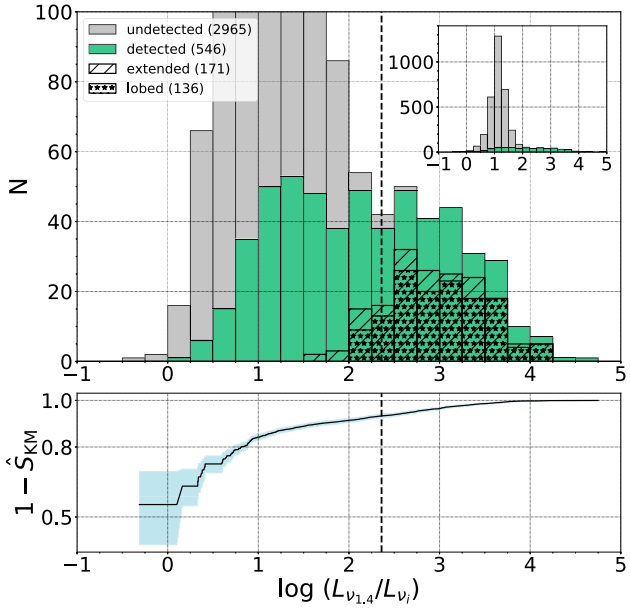

Figure 1. The top panel presents the radio-loudness distribution for our 0.5–0.7 QSOs sample. Sources with and without radio detections are shown separately (in green and gray, accordingly). Within radio-detected objects, we distinguish those with radio extended morphologies (hatched) and those with morphologies that exhibit two clearly separated lobes (starred). The black-dashed line marks the value of $\log(L_{\nu_{1.4}}/L_{\nu_i}) = 2.36$ separating objects into RL and RI&RQ, following the definition of radio-loudness by Kellermann et al. (1989). The characteristics of these radio morphologies are closely described in Section 3.1.3. The bottom panel depicts the estimated cumulative distribution function (black-solid line) taking into account the left-censored data points using the Kaplan-Meier estimator for the survival function (Kaplan & Meier 1958). The light blue area illustrates the 95% confidence interval for the estimator.

which takes into account the upper limits used for the radio-undetected sources (Kaplan & Meier 1958). The estimator was computed using the Python package `lifelines` (Davidson-Pilon 2019) to estimate the survival function $\hat{S}_{\rm KM} = 1 - \hat{F}$. The upper panel might suggest that there are almost no sources with $\log(L_{\nu_{1.4}}/L_{\nu_i}) < 0$ and maybe half the sources with $\log(L_{\nu_{1.4}}/L_{\nu_i}) \lesssim 1$; however, the estimated CDF shows that likely half or more of the sources should have $\log(L_{\nu_{1.4}}/L_{\nu_i}) < 0$ and over 80% should have $\log(L_{\nu_{1.4}}/L_{\nu_i}) < 1$. The blue shaded area represents the 95% confidence interval for the estimator. For higher values of the radio-loudness, the estimated CDF has very low uncertainty because almost all of these sources correspond to real measurements.

Dividing objects into radio-loud, radio-intermediate, and radio-quiet (based on the shape of the radio-loudness distribution and the demarcation introduced by Kellermann et al. (1989) being RL for $\mathcal{R}_{\rm K} > 100$, RI for $10 < \mathcal{R}_{\rm K} < 100$, RQ when $\mathcal{R}_{\rm K} < 10$; see Appendix A for recalculation between $\mathcal{R}_{\rm K}$ and $L_{\nu_{1.4}}/L_{\nu_i}$), we find 235, 695, and 2 581 sources belonging to the given class, respectively. This categorization corresponds well with the presence or lack of detectable radio emission and its character. Extended, and among them lobed, sources are almost exclusively radio-loud, spanning the two highest decades of radio-loudness. This group contains less than 1% of radio-undetected objects[7], which is exactly the opposite for radio-quiet sources being dominated by objects lacking radio

[7] Among the 235 RL sources, only two objects do not have assigned radio data, which are SDSS J003330.69+004251.4, with $\log M_{\rm BH} = 8.6$, $\log \lambda_{\rm Edd} = -2.59$ and SDSS J125303.76+402749.9 with $\log M_{\rm BH} = 8.9$, $\log \lambda_{\rm Edd} = -2.91$.

Table 3
Radio Morphologies and Radio Classes of all 0.5–0.7 QSOs

Radio Morphology		Radio Class			Total
		RL	RI	RQ	
Detected	Extended	145	26		171
	(Lobed)	(122)	(14)		(136)
	Compact	88	160	127	375
Undetected		2	509	2454	2965
Total		235	695	2581	3511

Note. A detailed description is given in Sections 3.1.3 and 3.2. Lobed sources are a subgroup of extended ones. Their exact counts, which are shown in brackets, are not added to the total because they are already included in the numbers for extended sources.

detections. Finally, quasars classified as radio-intermediate have compact, extended, and lobed morphologies but also no radio data assigned. The specific numbers of these relations are listed in Table 3.

3.3. Radio-loud Fraction

Knowing the radio-loudness distribution of 0.5–0.7 QSOs, and splitting them into RL and RI & RQ groups, we place them on the $\lambda_{\rm Edd} - M_{\rm BH}$ plane shown in Figure 2. Both groups occupy similar ranges of both parameters, with RL objects being more massive and having lower accretion rates than RI & RQ ones. The limit of $M_{\rm BH} \geqslant 10^{8.5} M_\odot$ especially affects the radio-quieter sources because their BH mass distribution is smoothly increasing toward lower values of $M_{\rm BH}$.

The lack of quasars in the lower left-hand corner of the diagram is a consequence of the SDSS DR7 optical flux limit in the *i*-band, while the deficiency of quasars in the upper-right corner is associated with the downsizing effect (e.g., Fanidakis et al. 2012; Hirschmann et al. 2014). Most of the objects are located within an area of $-2.5 \leqslant \log \lambda_{\rm Edd} \leqslant -0.5$ and $8.5 \leqslant \log M_{\rm BH} \leqslant 9.5$, which provides the best representation of RL to RI & RQ objects upon which the radio-loud fraction is analyzed (and within which all the radio-loud sources are radio-detected).

Since the probability of production of powerful jets by quasars can depend not only on the redshift but also on the BH mass and on the specific accretion rate (the latter being traced for a given radiative efficiency of the accretion flow by the Eddington ratio), the RLF—which is defined as the ratio of the RL quasars to all quasars—is expected to depend on the distribution of the BH masses and Eddington ratios in the sample. Indeed, as we can see in Figure 2, the number of sources strongly varies in $M_{\rm BH}$ and $\lambda_{\rm Edd}$. Thus, we study the dependence of the RLF of quasars on the BH mass and Eddington ratio within a limited range of both parameters, as presented in Figure 3.

Figure 3 demonstrates the increase of RLF with BH mass and its near lack of a dependence on the Eddington ratio. Some variations among the fixed values of $M_{\rm BH}$ and $\lambda_{\rm Edd}$ are apparent but this should not be surprising after considering the number of sources in specific regions. Despite these variations, the correlation of RLF with BH mass is clearly visible at all Eddington ratio values, while no correlation between RLF and Eddington ratio can be inferred at any of the BH mass values. This trend still persists while considering the nonnegligible

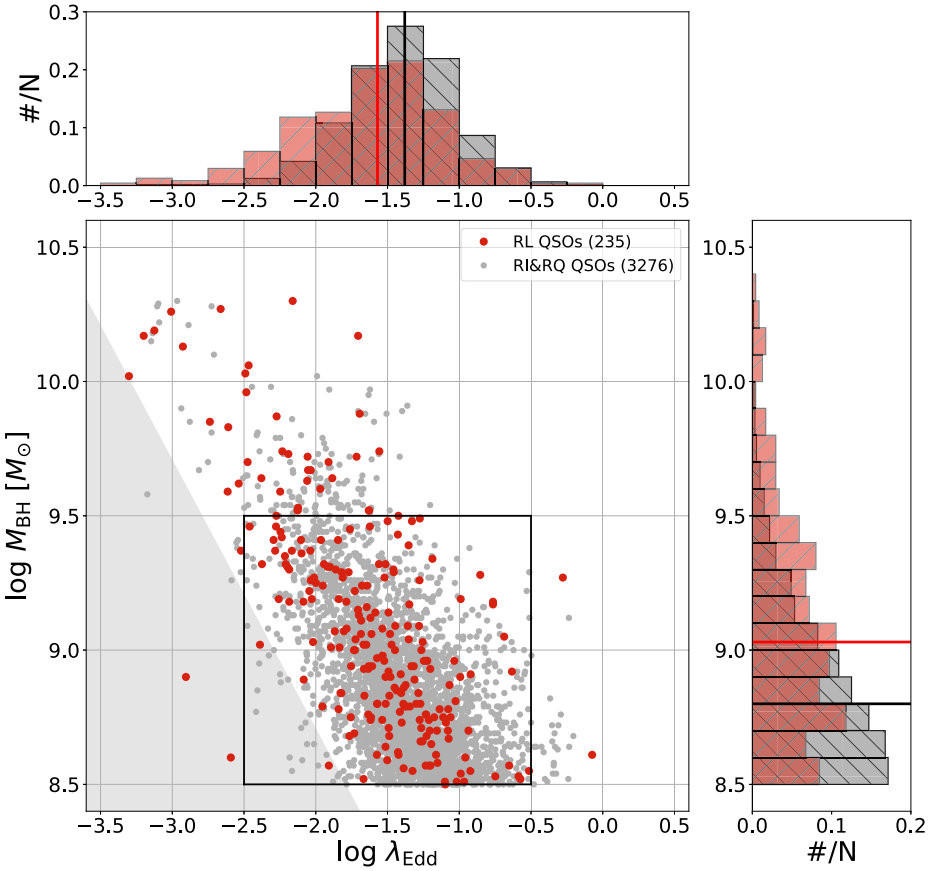

Figure 2. Distribution of all the 0.5–0.7 QSOs in $\log \lambda_{\rm Edd}$ versus $\log M_{\rm BH}$ plane. Radio-loud and radio-intermediate with radio-quiet quasars are shown separately (in red and gray, accordingly). The shaded area on the lower left-hand corner marks the region of sources fainter than those observed by SDSS, corresponding to $L_{\rm bol,\ min} \simeq \frac{2}{3} \times 10^{45}$erg s^{-1} (at $z \sim 0.6$ and $M_i \leqslant -22$), and for which the estimation of Eddington ratio is biased. The best representation of RL to RI&RQ objects overlaps with the limits of the inlaid box, which are further adopted for Figure 3. The median values of $\log \lambda_{\rm Edd}$ and $\log M_{\rm BH}$ presented on the relevant histograms are: $\log \lambda_{\rm Edd,\ RL} = -1.57$ and $\log \lambda_{\rm Edd,RI\&RQ} = -1.38$; $\log M_{\rm BH,\ RL} = 9.03$ and $\log M_{\rm BH,RI\&RQ} = 8.80$ (all marked in red for RL and black for RI&RQ).

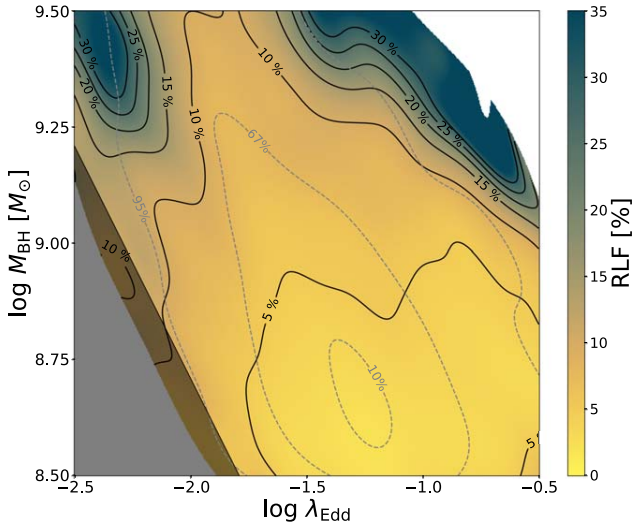

Figure 3. The radio-loud fraction as a function of $\log \lambda_{\rm Edd}$ and $\log M_{\rm BH}$ computed from a Gaussian kernel density estimate for the number density of radio-loud and radio-quiet sources. The shaded area on the left-hand corner demonstrates the region of sources with a biased estimation of Eddington ratio (just as in Figure 2), while the white corners, bottom left-hand and top right-hand, are masked due to the low number density of RL, as well as RI&RQ objects (below 10). The RLF is represented with the color density map and the explicit percentages are shown on the black-solid contours. The gray-dashed contours correspond to isodensity contours enclosing the indicated percentages of the total sample.

effect of the measurement uncertainties on the distributions of $M_{\rm BH}$ and $\lambda_{\rm Edd}$.

4. Discussion

Quasars can be divided into those with radio production dominated by jets and those with dominant radio contribution coming from processes that are not associated with the presence of jets. A particular subclass of the first population are quasars associated with classical FR II radio sources (Fanaroff & Riley 1974). The distribution of their radio-loudness defined by Kellermann et al. (1989), $\mathcal{R}_{\rm K} = L_{\nu_5}/L_{\nu_{\rm B}}$ (see Appendix A) spans the range 10^2–10^4, with a peak at $\sim 10^3$, while the radio of the second population is presumably dominated by star-forming regions (SFRs, e.g., Condon 1992; Kimball et al. 2011; Panessa et al. 2019; Kozieł-Wierzbowska et al. 2021), with their radio-loudness distribution enclosed within the range of $0.1 < \mathcal{R}_{\rm K} < 10$ (see Figure 1). With these representations, they cover well the separated ranges of $\mathcal{R}_{\rm K}$ and form a clear bimodal distribution, with the first population called RLQs and the second population called RQQs. However, not all $\mathcal{R}_{\rm K} > 100$ quasars are FR II: others have more complex radio morphology or are unresolved. Part of them fill up the gap in $\mathcal{R}_{\rm K}$-histograms between quasars with $\mathcal{R}_{\rm K} > 10$ and quasars with $\mathcal{R}_{\rm K} < 100$, and represent the so-called radio-intermediate quasars. Since they are too radio-loud to be explained by processes taking place in SFRs, they are often considered to

have radio emission powered by jets but with most of the jet energy dissipated within galaxies, such as those represented by FR I quasars (Blundell & Rawlings 2001; Heywood et al. 2007). However, $\mathcal{R}_K$ with values up to tens are also achievable by radio emission powered by accretion disk winds (Blundell & Kuncic 2007; Zakamska & Greene 2014; Nims et al. 2015; Zakamska et al. 2016; White et al. 2017; Hwang et al. 2018; Morabito et al. 2019; Rosario et al. 2020; Vayner et al. 2021). Hence, with the possible presence of such quasars in the radio-intermediate band ($10 < \mathcal{R}_K < 100$), the commonly used definition in the literature of the RLF as the ratio of objects with $\mathcal{R}_K > 10$ to their total number may lead to a significant overestimation of the fraction of quasars that have radio emission dominated by jet activity. Noting that such an overestimation can depend on the redshift and that within the RI band there are also objects with upper limits of $\mathcal{R}_K$ (see Table 3), we focused our studies on the RLF of quasars with $\mathcal{R}_K > 100$, where they all are "radio-categorized" (in the sense of not including quasars with only upper limits on the radio flux) and are expected to be fully represented by quasars with strong jets.

The negative correlation of radio-loud fraction with redshift that we identified in Section 2 can be examined toward lower values of redshift. For this purpose, we consider the well-established sample of 0.5–0.7 QSOs introduced in Section 3 (with RLF being 6.69%) and an additional set of AGNs located nearby, which were compiled by Rusinek et al. (2020). The advantage of using the latter arises not only from the great fraction of radio-detected sources studied therein (257 out of 314 objects, 82%) but also from the similar approach of building their sample, i.e., the estimation of BH masses and bolometric luminosities (hence—Eddington ratios), which was performed in the same manner for all the sources, the limitation of $M_{\rm BH} \geqslant 10^{8.5} M_{\odot}$, the usage of radio data at 1.4 GHz (collected from i.a. FIRST), and the division of the sample into RL, RI, and RQ objects, as well as those with and without radio detections. The main differences are the source selection, which in the case of Rusinek et al. was done from the Swift/Burst Alert Telescope (BAT) AGN Spectroscopic Survey catalog (BASS, Ricci et al. 2017), while our 0.5–0.7 QSOs and the samples selected from Gürkan et al. (2019) are based on optical data from SDSS. The calculation of radio-loudness as Rusinek et al. uses infrared instead of optical data to trace the accretion power choosing the W3 band, $\lambda_{\rm W3} = 12\ \mu m$[8], from Wide-field Infrared Survey Explorer (WISE, Cutri et al. (2013). The reasoning behind this choice is provided in Appendix A.2 in Rusinek et al. (2020); see also Gupta et al. 2020). Such a well-defined sample was studied regarding its radio and optical morphologies, radio-loudness distribution, and jet production efficiencies by Rusinek et al. (2020) and analyzed earlier by Gupta et al. (2018, 2020) in the context of the similarities and differences of the spectral energy distributions between RL and RQ AGNs of both Type 1and Type 2.

The relationship between the RLF and redshift with additional two sets of sources is shown in Figure 4. As one can clearly see, the previously found trend is maintained down to the lowest redshifts covered by Swift/BAT AGNs for which the RLF is found to be 14%. The real dependence of RLF on the redshift is expected to be even steeper because it may be affected by the correlation of RLF with BH masses (as shown in Table 1 and studied thoroughly in Section 3). In addition, the radio frequency at which the given sample was observed would also contribute to the steeper dependence of RLF on redshift; i.e., some of the radio-quieter sources in our 0.5–0.7 QSOs and Swift/BAT AGNs taken from Rusinek et al. (2020) could reveal their more extended radio structures with their radio luminosity increasing while being observed at lower frequencies, while the opposite would be observed for radio-loud objects from the sample of Gürkan et al. (2019) seen at higher radio frequencies. Meanwhile, the RLF in the AGN sample taken from Rusinek et al. (2020) can be slightly overestimated, due to the fact that this sample was selected based on X-ray observations and that RLQs are found to be on average X-ray louder than RQQs (see Gupta et al. 2018, 2020).

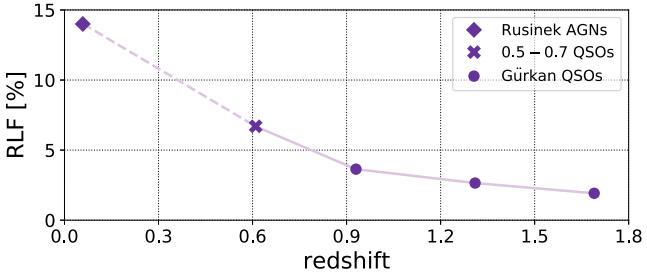

Figure 4. The radio-loud fraction as a function of redshift. The five various samples correspond to: the Swift/BAT AGN sample taken from Rusinek et al. (2020), represented by a diamond; the set of 0.5–0.7 QSOs discussed in Section 3, being marked as a cross; and three populations of quasars selected from Gürkan et al. (2019), which are shown as circles. The specific values of RLF and median redshifts are: 14.00%, 6.69%, 3.64%, 2.65%, 1.92%; and 0.06, 0.61, 0.93, 1.31, 1.69, respectively. These values should be treated with caution because an outline of the dependence that we found between those two parameters (RLF and z), due to some differences between the samples, especially given that the sources in Rusinek et al. were selected based on X-ray instead of optical data.

Even though the specific values of RLF presented in Figure 4 should be treated with caution, the negative correlation of the radio-loud fraction with redshift that we found suggests a differential evolution of the space density of triggers of jetted and nonjetted quasars, with the former dropping with cosmic time more slowly than the latter. In both cases, the quasar triggers are likely to be associated with galaxy mergers (e.g., Lin et al. 2008; Shen 2009; Bessiere et al. 2012; O'Leary et al. 2021). As studies of optical morphologies of nearby RL and RQ objects indicate, those leading to triggering of radio-loud quasars presumably involve mergers of giant ellipticals with gas-rich disk galaxies, while most of radio-quiet quasars are born following mergers of two disk galaxies (e.g., Rusinek et al. 2020). Such a connection between quasar types and merger types is also supported by studies of the redshift evolution of mergers, which show that the ratio of E–Sp merger events to Sp–Sp merger events is increasing with cosmic time (see Lin et al. 2008, and refs. therein). However, there is also a nonnegligible fraction of RQ quasars that (like RL quasars) are hosted by gE, and which (like RL ones) are presumably triggered by mergers of gE with disk galaxies.

4.1. On the Origin of the Diversity of the Jet Production Efficiency in RL Quasars

Using radio lobe calorimetry to calculate jet powers in FR II quasars (e.g., Willott et al. 1999; Shabala & Godfrey 2013) and optical or infrared data to calculate bolometric luminosities of the accretion flow (see Richards et al. 2006, and refs. therein)

[8] As was demonstrated by Ichikawa et al. (2019), mid-IR radiation in nearby luminous AGNs is dominated by dust heated by radiation from the accretion disk.

allows the estimation of the jet production efficiency, $\eta_j = P_j/\dot{M}c^2 = \epsilon_d\, P_j/L_{\rm bol}$, where P_j is the jet power and $\epsilon_d = L_{\rm bol}/\dot{M}c^2$ is the radiative efficiency of the accretion disk with $\dot{M}$ being the accretion rate. According to van Velzen & Falcke (2013), Inoue et al. (2017), and Rusinek et al. (2017), this efficiency is spread over about two decades, with the median on the order of $0.01(\epsilon_d/0.1)$. These efficiencies are achievable in the magnetically arrested disk (MAD) models, according to which $P_j \sim a^2\dot{M}c^2(H/R)$, where $-1 < a < 1$ is the dimensionless BH spin and (H/R) is the geometrical thickness of the accretion flow (see review by Davis & Tchekhovskoy 2020).

4.2. Can MADs Represent Temporary States During the Quasar Lifetime?

Any intermittency of production of jets powering FR II radio structures should result in having some FR IIs without radio cores, which are known to represent Doppler-boosted parcsec-scale portions of the jet (e.g., Blandford & Königl 1979; Marin & Antonucci 2016). Since radio cores are observed in all FR II quasars (e.g., Van Gorkom et al. 2015), such an intermittency is rather excluded. However, this does not exclude the possibility of strong modulation of the jet production, which can be responsible for knotty structures of some large scale jets (see, e.g., Godfrey et al. 2012). Such modulations can be explained in terms of the MAD model by noting that according to this model the power of a jet scales with the accretion rate and this, in turn, can be modulated by the viscous instabilities in the accretion disk (Janiuk & Czerny 2011).

Claims about lacking an intermittency in the production of powerful jets might be contradictory to having too many luminous Gigahertz-Peaked Spectrum (GPS) sources if they are considered to have powerful jets at young ages (Reynolds & Begelman 1997). However, multifrequency monitorings suggest that such an excess is presumably a consequence of treating many blazars as young, unresolved double radio sources (Mingaliev et al. 2012; Sotnikova et al. 2019).

4.3. Why Should MADs Only Be Available in Quasars Activated by Mergers Involving Massive Ellipticals and Why Not in All of Them?

An answer for this double question can be provided in terms of the scenario marked in the Section 1 by "C". According to this scenario, the MAD is formed during the quasi-spherical, low accretion rate phase. The presence of such a phase accompanied by jet activity is indicated by observations of radio activity in the nuclei of massive elliptical galaxies (Sabater et al. 2019). Depending on parameters such as the accretion rate and the size of the formed MAD, some MADs can survive transition to the quasar phase, while others cannot (see Sikora & Begelman 2013 and Figure 5 in Rusinek et al. 2017).

Another possibility may involve scenario "B", according to which the merger may lead to the formation of corotating and counterrotating accretion flows relative to the BH spin (see Garofalo et al. 2020, and refs. therein). As argued by Rusinek et al. (2020), in the latter case the operation of the Poynting–Robertson process can be efficient enough to lead to the formation of a MAD. However, it is not clear that such a counterrotating BH-disk systems can be stable (King et al. 2005).

In both the above scenarios, the probability of getting MAD correlates with the BH mass, which is consistent with the relation between RLF and BH mass found by Kratzer & Richards (2015) and confirmed by us. Having RQ quasars hosted not only by disk galaxies but also by elliptical galaxies weakens the differentiation of the dependence of the RLF of RQ and RL quasars on redshift, but not significantly, if the majority of RQ quasars are hosted by disk galaxies.

5. Summary

We studied the dependence of the radio-loud fraction (RLF) of quasars with BH masses larger than $10^{8.5}M_\odot$ on:

1. Redshift, using three well-defined samples within the range of $0.7 \leqslant z < 1.9$ selected from the SDSS DR14 catalog of quasars matched with the LoTSS radio catalog;
2. Black hole masses and accretion rates, using a highly controlled, and redshift-narrowed (around $z \sim 0.6$) sample selected from the SDSS DR7 catalog of quasars matched with the FIRST radio catalog,

while treating as radio-loud objects those with radio-loudness parameter defined by Kellermann et al. (1989) to be larger than 100. In the first step, we found that the RLF decreases with increasing redshift (see Table 1 and Figure 4, with the addition of two more samples in the latter).

A detailed investigation of the relationships between the RLF and BH masses, and Eddington ratios, as well as a more general study of the radio properties, was conducted with the sample of quasars with redshifts enclosed within the range of $0.5 \leqslant z < 0.7$. This allowed us to verify whether and how the dependence of the RLF on $M_{\rm BH}$ and $\lambda_{\rm Edd}$ can bias the dependence of the RLF on redshift that we found. Our results show that the dependence of the RLF on redshift is expected to be biased only by the dependence of the RLF on BH mass. Since the average BH masses in the Gürkan et al. sample increase with redshift (see Table 1), such a bias weakens the dependence of the RLF on redshift; i.e., without that bias, the drop of the RLF with redshift would be even steeper than presented in the Figure 4.

Assuming that quasar activities are triggered by mergers of galaxies and that, contrary to radio-quiet quasars, the vast majority of RL quasars are hosted by giant ellipticals, we showed that the decreasing fraction of RL quasars with redshift can simply result from the theoretically predicted and observationally confirmed slower drop with cosmic time of mergers of giant ellipticals with spiral galaxies than of mergers of two spiral galaxies. Finally, we speculate about possible scenarios of formation of magnetically arrested disks (MADs), which could explain the connections indicated by observations between types of mergers and the production of powerful jets.

Our studies should be treated as a starting point for further extensive analysis that could be carried out using, for example, the upcoming LoTSS DR2 catalog (T. W. Schimwell et al. 2021, in preparation), which covers a sky area of 5720 $\deg^2$; i.e., over 13 times bigger than a sky area of LoTSS DR1 used by Gürkan et al. (2019).

We thank David Abarca for useful discussions, editorial and linguistic assistance, and technical advice. We thank the anonymous referee for his attentive comments, which significantly contributed to improving the quality of the publication. The research leading to these results has received funding

from the Polish National Science Centre grant 2015/18/A/ST9/00746.

Facilities: Funding for the Sloan Digital Sky Survey IV has been provided by the Alfred P. Sloan Foundation, the U.S. Department of Energy Office of Science, and the Participating Institutions.

SDSS-IV acknowledges support and resources from the Center for High Performance Computing at the University of Utah. The SDSS website is www.sdss.org.

SDSS-IV is managed by the Astrophysical Research Consortium for the Participating Institutions of the SDSS Collaboration including the Brazilian Participation Group, the Carnegie Institution for Science, Carnegie Mellon University, Center for Astrophysics | Harvard & Smithsonian, the Chilean Participation Group, the French Participation Group, Instituto de Astrofísica de Canarias, The Johns Hopkins University, Kavli Institute for the Physics and Mathematics of the Universe (IPMU)/University of Tokyo, the Korean Participation Group, Lawrence Berkeley National Laboratory, Leibniz Institut für Astrophysik Potsdam (AIP), Max-Planck-Institut für Astronomie (MPIA Heidelberg), Max-Planck-Institut für Astrophysik (MPA Garching), Max-Planck-Institut für Extraterrestrische Physik (MPE), National Astronomical Observatories of China, New Mexico State University, New York University, University of Notre Dame, Observatário Nacional / MCTI, The Ohio State University, Pennsylvania State University, Shanghai Astronomical Observatory, United Kingdom Participation Group, Universidad Nacional Autónoma de México, University of Arizona, University of Colorado Boulder, University of Oxford, University of Portsmouth, University of Utah, University of Virginia, University of Washington, University of Wisconsin, Vanderbilt University, and Yale University.

Software: The `Python` package `lifelines` was used to compute the Kaplan-Meier estimator (Davidson-Pilon 2019).

Appendix A
Conversion of Radio Loudness Parameter

Among the various methods that are used to classify quasars into RL or RQ, to this day the most common is still the approach described by Kellermann et al. (1989), defining the radio-loudness parameter as the ratio of radio-to-optical monochromatic luminosity, at 5 GHz and in *B*-band, being

$$\mathcal{R}_{\rm K} = L_{\nu_5}/L_{\nu_{\rm B}} = (F_{\nu_5}/F_{\nu_{\rm B}})(1+z)^{\alpha_{\rm r}-\alpha_{\rm o}}, \tag{A1}$$

where F_{ν_5} and $F_{\nu_{\rm B}}$ are the flux densities at $\nu_5 \equiv 5$ GHz and $\nu_{\rm B} \simeq 6.8\times10^{14}$ Hz with $\alpha_{\rm r}$ and $\alpha_{\rm o}$ being the spectral radio and optical indices, given as $\alpha = -\frac{d\ln F_\nu}{d\ln\nu}$, respectively. Then, the radio-loudness defined at any radio frequency, $\nu_{\rm r}$, and optical frequency, $\nu_{\rm o}$ (alternatively, at infrared, $\nu_{\rm IR}$, or X-ray frequency, $\nu_{\rm X}$) can be converted to the one defined by Kellermann et al. using the formula

$$\mathcal{R}_{\rm K} = \frac{F_{\nu_5}/F_{\nu_{\rm r}}}{F_{\nu_{\rm B}}/F_{\nu_o}} \times \frac{(1+z)^{\alpha_5-\alpha_{\rm r}}}{(1+z)^{\alpha_{\rm B}-\alpha_{\rm o}}} \times \frac{L_{\nu_{\rm r}}}{L_{\nu_{\rm o}}}. \tag{A2}$$

Defining the two-point spectral indices,

$$\langle\alpha_r\rangle = -\frac{\log(F_{\nu_5}/F_{\nu_r})}{\log(\nu_5/\nu_r)} \tag{A3}$$

and

$$\langle\alpha_o\rangle = -\frac{\log(F_{\nu_{\rm B}}/F_{\nu_o})}{\log(\nu_{\rm B}/\nu_o)}, \tag{A4}$$

and noting that for $z<2$, and typical radio and optical/infrared spectral indices, the term $(1+z)^{(\alpha_5-\alpha_{\rm r})-(\alpha_{\rm B}-\alpha_{\rm o})}$ is of the order of unity, one can find that

$$\mathcal{R}_{\rm K} \simeq \frac{(\nu_5/\nu_{\rm r})^{-\langle\alpha_{\rm r}\rangle}}{(\nu_{\rm B}/\nu_{\rm o})^{-\langle\alpha_{\rm o}\rangle}} \times \frac{L_{\nu_{\rm r}}}{L_{\nu_{\rm o}}}. \tag{A5}$$

Using this formula for the Gürkan et al. and 0.5–0.7 QSOs samples (Sections 2 and 3) with $\langle\alpha_r\rangle = 0.7$ (see Yuan et al. 2018) and $\langle\alpha_o\rangle = 0.5$ (see Richards et al. 2006), we get $\mathcal{R}_{\rm K}^{\rm (G)} \simeq 0.12\times L_{\nu_{144}}/L_{\nu_i}$ and $\mathcal{R}_{\rm K}^{(0.5--0.7)} \simeq 0.59\times L_{\nu_{1.4}}/L_{\nu_i}$.

For the sample of Swift/BAT AGNs taken from Rusinek et al. (2020), the two-point spectral index of $\langle\alpha_o\rangle$ between $\nu_{\rm W3}$ and $\nu_{\rm B}$ is on the order of $\sim$1 (see the SED in Gupta et al. 2020) and then $\mathcal{R}_{\rm K}^{\rm (R)} \simeq 11\times L_{\nu_{1.4}}/L_{\nu_{\rm W3}}$.

Appendix B
0.5–0.7 QSOs Sample

Table B.1 presents the most important information about some of the sources in the 0.5–0.7 QSOs sample. The complete sample is available as supplementary material online.

Table B1
Sample of 0.5–0.7 QSOs (total of 3511 Objects) used in this Study

SDSS Name	z	$\log M_{\rm BH}$ ($M_\odot$)	$\log L_{\rm bol}$ (erg s^{-1})	$\log \lambda_{\rm Edd}$	$F_{1.4}$ (mJy)	$L_{\nu 1.4}/L_{\nu i}$	Radio Class[b]	Radio Morphology[a]
081214.31+063653.2	0.6603	8.73	45.89	−0.94	1.0	7.60	RQ	U
081218.40+110300.5	0.6432	9.27	45.58	−1.79	2.1	31.33	RI	C
081259.17+150226.0	0.6048	8.76	45.50	−1.36	1.0	15.16	RQ	U
081259.76+211103.9	0.6123	8.88	45.42	−1.56	1.0	18.79	RQ	U
081318.85+501239.7	0.5714	9.14	45.66	−1.58	487.3	4532.62	RL	L
081322.58+171638.6	0.6121	8.79	45.71	−1.18	1.0	9.57	RQ	U
081327.61+561625.8	0.5063	8.77	45.61	−1.26	4.2	32.64	RI	C
081344.01+171103.2	0.5814	9.30	45.54	−1.86	27.8	350.94	RL	E
081416.99+252935.1	0.6026	9.57	45.50	−2.17	1.0	14.93	RQ	U
081502.81+513313.3	0.5128	8.54	45.39	−1.25	1.0	13.37	RQ	U
081510.31+403750.5	0.5895	8.53	45.44	−1.19	1.0	16.21	RQ	U
081512.01+115311.6	0.5511	8.55	45.61	−1.04	1.0	9.42	RQ	U
081558.06+501232.2	0.5996	9.01	46.09	−1.02	1.0	3.84	RQ	U
081601.94+240925.8	0.5529	9.16	45.63	−1.63	1.0	9.09	RQ	U
081615.35+550615.5	0.6145	8.62	45.52	−1.20	1.0	14.95	RQ	U
081629.13+493249.9	0.6846	8.99	45.75	−1.34	1.0	11.44	RQ	U
081632.66+152008.2	0.6586	8.95	45.44	−1.61	1.0	21.15	RQ	U
081655.34+074311.5	0.6442	8.53	45.65	−0.98	1.0	12.51	RQ	U
081707.04+351819.8	0.694	8.89	45.43	−1.56	1.0	24.56	RI	C
081710.05+321802.1	0.6159	8.60	45.33	−1.37	1.0	23.33	RI	U

Notes. This subset of the table demonstrates format and content.
[a] RL—radio-loud; RI—radio-intermediate; RQ—radio-quiet.
[b] L—lobed; E—extended (but not lobed); C—compact; U—undetected.

(This table is available in its entirety in machine-readable form.)

ORCID iDs

Katarzyna Rusinek-Abarca https://orcid.org/0000-0002-6424-6558
Marek Sikora https://orcid.org/0000-0003-1667-7334

References

Abazajian, K. N., Adelman-McCarthy, J. K., Agüeros, M. A., et al. 2009, ApJS, 182, 543
Becker, R. H., White, R. L., & Helfand, D. J. 1995, ApJ, 450, 559
Beckwith, K., Hawley, J. F., & Krolik, J. H. 2008, ApJ, 678, 1180
Beckwith, K., Hawley, J. F., & Krolik, J. H. 2009, ApJ, 707, 428
Begelman, M. C. 1995, PNAS, 92, 11442
Beloborodov, A. M. 2017, ApJ, 850, 141
Bessiere, P. S., Tadhunter, C. N., Ramos Almeida, C., & Villar Martín, M. 2012, MNRAS, 426, 276
Bird, J., Martini, P., & Kaiser, C. 2008, ApJ, 676, 147
Bisnovatyi-Kogan, G. S., & Lovelace, R. V. E. 2007, ApJL, 667, L167
Bisnovatyi-Kogan, G. S., & Ruzmaikin, A. A. 1976, Ap&SS, 42, 401
Blandford, R. D., & Königl, A. 1979, ApJ, 232, 34
Blanton, M. R., Bershady, M. A., Abolfathi, B., et al. 2017, AJ, 154, 28
Blundell, K. M., & Kuncic, Z. 2007, ApJL, 668, L103
Blundell, K. M., & Rawlings, S. 2001, ApJL, 562, L5
Cao, X. 2016, ApJ, 833, 30
Cao, X., & Lai, D. 2019, MNRAS, 485, 1916
Condon, J. J. 1992, ARA&A, 30, 575
Contopoulos, I., & Kazanas, D. 1998, ApJ, 508, 859
Cutri, R. M., Wright, E. L., Conrow, T., et al. 2013, yCat, 2328, 0
Davidson-Pilon, C. 2019, JOSS, 4, 1317
Davis, S. W., & Tchekhovskoy, A. 2020, ARA&A, 58, 407
de Vries, W. H., Becker, R. H., & White, R. L. 2006, AJ, 131, 666
Donoso, E., Li, C., Kauffmann, G., Best, P. N., & Heckman, T. M. 2010, MNRAS, 407, 1078
Elvis, M., Wilkes, B. J., McDowell, J. C., et al. 1994, ApJS, 95, 1
Fanaroff, B. L., & Riley, J. M. 1974, MNRAS, 167, 31P
Fanidakis, N., Baugh, C. M., Benson, A. J., et al. 2012, MNRAS, 419, 2797
Floyd, D. J. E., Axon, D., Baum, S., et al. 2010, ApJ, 713, 66
Garofalo, D., North, M., Belga, L., & Waddell, K. 2020, ApJ, 890, 144
Godfrey, L. E. H., Lovell, J. E. J., Burke-Spolaor, S., et al. 2012, ApJL, 758, L27
Guilet, J., & Ogilvie, G. I. 2012, MNRAS, 424, 2097
Guilet, J., & Ogilvie, G. I. 2013, MNRAS, 430, 822
Gupta, M., Sikora, M., & Rusinek, K. 2020, MNRAS, 492, 315
Gupta, M., Sikora, M., Rusinek, K., & Madejski, G. M. 2018, MNRAS, 480, 2861
Gürkan, G., Hardcastle, M. J., Best, P. N., et al. 2019, A&A, 622, A11
Hardcastle, M. J., Gürkan, G., van Weeren, R. J., et al. 2016, MNRAS, 462, 1910
Hewett, P. C., & Wild, V. 2010, MNRAS, 405, 2302
Heywood, I., Blundell, K. M., & Rawlings, S. 2007, MNRAS, 381, 1093
Hill, G. J., Gebhardt, K., Komatsu, E., et al. 2008, in ASP Conf. Ser., 399, Panoramic Views of Galaxy Formation and Evolution, ed. T. Kodama, T. Yamada, & K. Aoki (San Francisco, CA: ASP), 115
Hirschmann, M., Dolag, K., Saro, A., et al. 2014, MNRAS, 442, 2304
Hwang, H.-C., Zakamska, N. L., Alexandroff, R. M., et al. 2018, MNRAS, 477, 830
Ichikawa, K., Ricci, C., Ueda, Y., et al. 2019, ApJ, 870, 31
Igumenshchev, I. V. 2008, ApJ, 677, 317
Inoue, Y., Doi, A., Tanaka, Y. T., Sikora, M., & Madejski, G. M. 2017, ApJ, 840, 46
Janiuk, A., & Czerny, B. 2011, MNRAS, 414, 2186
Jiang, L., Fan, X., & Ivezić, Ž. 2007, ApJ, 656, 680
Kaplan, E. L., & Meier, P. 1958, Journal of the American Statistical Association, 53, 457
Kellermann, K. I., Sramek, R., Schmidt, M., Shaffer, D. B., & Green, R. 1989, AJ, 98, 1195
Khochfar, S., & Burkert, A. 2003, ApJL, 597, L117
Kimball, A. E., Kellermann, K. I., Condon, J. J., Ivezić, Ž., & Perley, R. A. 2011, ApJL, 739, L29
King, A. R., Lubow, S. H., Ogilvie, G. I., & Pringle, J. E. 2005, MNRAS, 363, 49
Koutsantoniou, L. E., & Contopoulos, I. 2014, ApJ, 794, 27
Kozieł-Wierzbowska, D., Vale Asari, N., Stasińska, G., et al. 2021, ApJ, 910, 64
Kozłowski, S. 2017, ApJS, 228, 9
Kratzer, R. M., & Richards, G. T. 2015, AJ, 149, 61
Lin, L., Patton, D. R., Koo, D. C., et al. 2008, ApJ, 681, 232
Lubow, S. H., Papaloizou, J. C. B., & Pringle, J. E. 1994, MNRAS, 267, 235

Mandelbaum, R., Li, C., Kauffmann, G., & White, S. D. M. 2009, MNRAS, 393, 377
Marconi, A., Risaliti, G., Gilli, R., et al. 2004, MNRAS, 351, 169
Marin, F., & Antonucci, R. 2016, ApJ, 830, 82
McKinney, J. C., Tchekhovskoy, A., & Blandford, R. D. 2012, MNRAS, 423, 3083
Mingaliev, M. G., Sotnikova, Y. V., Torniainen, I., Tornikoski, M., & Udovitskiy, R. Y. 2012, A&A, 544, A25
Morabito, L. K., Matthews, J. H., Best, P. N., et al. 2019, A&A, 622, A15
Myers, A. D., Palanque-Delabrouille, N., Prakash, A., et al. 2015, ApJS, 221, 27
Narayan, R., Igumenshchev, I. V., & Abramowicz, M. A. 2003, PASJ, 55, L69
Nims, J., Quataert, E., & Faucher-Giguère, C.-A. 2015, MNRAS, 447, 3612
O'Leary, J. A., Moster, B. P., Naab, T., & Somerville, R. S. 2021, MNRAS, 501, 3215
Panessa, F., Baldi, R. D., Laor, A., et al. 2019, NatAs, 3, 387
Pâris, I., Petitjean, P., Aubourg, É., et al. 2018, A&A, 613, A51
Retana-Montenegro, E., & Röttgering, H. J. A. 2017, A&A, 600, A97
Reynolds, C. S. 2019, NatAs, 3, 41
Reynolds, C. S., & Begelman, M. C. 1997, ApJL, 487, L135
Ricci, C., Trakhtenbrot, B., Koss, M. J., et al. 2017, ApJS, 233, 17
Richards, G. T., Lacy, M., Storrie-Lombardi, L. J., et al. 2006, ApJS, 166, 470
Rosario, D. J., Fawcett, V. A., Klindt, L., et al. 2020, MNRAS, 494, 3061
Rothstein, D. M., & Lovelace, R. V. E. 2008, ApJ, 677, 1221
Rusinek, K., Sikora, M., Kozieł-Wierzbowska, D., & Godfrey, L. 2017, MNRAS, 466, 2294
Rusinek, K., Sikora, M., Kozieł-Wierzbowska, D., & Gupta, M. 2020, ApJ, 900, 125
Sabater, J., Best, P. N., Hardcastle, M. J., et al. 2019, A&A, 622, A17
Schneider, D. P., Richards, G. T., Hall, P. B., et al. 2010, AJ, 139, 2360
Shabala, S. S., & Godfrey, L. E. H. 2013, ApJ, 769, 129
Shang, Z., Brotherton, M. S., Wills, B. J., et al. 2011, ApJS, 196, 2
Shankar, F., Calderone, G., Knigge, C., et al. 2016, ApJL, 818, L1
Shen, Y. 2009, ApJ, 704, 89
Shen, Y., Richards, G. T., Strauss, M. A., et al. 2011, ApJS, 194, 45
Shimwell, T. W., Röttgering, H. J. A., Best, P. N., et al. 2017, A&A, 598, A104
Sikora, M., & Begelman, M. C. 2013, ApJL, 764, L24
Sikora, M., Stasińska, G., Kozieł-Wierzbowska, D., Madejski, G. M., & Asari, N. V. 2013, ApJ, 765, 62
Sikora, M., Stawarz, Ł., & Lasota, J.-P. 2007, ApJ, 658, 815
Singal, J., Petrosian, V., Lawrence, A., & Stawarz, Ł. 2011, ApJ, 743, 104
Singal, J., Petrosian, V., Stawarz, Ł., & Lawrence, A. 2013, ApJ, 764, 43
Sironi, L., & Beloborodov, A. M. 2020, ApJ, 899, 52
Sotnikova, Y. V., Mufakharov, T. V., Majorova, E. K., et al. 2019, AstBu, 74, 348
Spruit, H. C., & Uzdensky, D. A. 2005, ApJ, 629, 960
Stern, D., Djorgovski, S. G., Perley, R. A., de Carvalho, R. R., & Wall, J. V. 2000, AJ, 119, 1526
Tadhunter, C. 2016, A&ARv, 24, 10
Treister, E., Schawinski, K., Urry, C. M., & Simmons, B. D. 2012, ApJL, 758, L39
Van Gorkom, K. J., Wardle, J. F. C., Rauch, A. P., & Gobeille, D. B. 2015, MNRAS, 450, 4240
van Haarlem, M. P., Wise, M. W., Gunst, A. W., et al. 2013, A&A, 556, A2
van Velzen, S., & Falcke, H. 2013, A&A, 557, L7
Vayner, A., Zakamska, N. L., Riffel, R. A., et al. 2021, MNRAS, 504, 4445
Vestergaard, M., & Peterson, B. M. 2006, ApJ, 641, 689
White, S. V., Jarvis, M. J., Kalfountzou, E., et al. 2017, MNRAS, 468, 217
Willott, C. J., Rawlings, S., Blundell, K. M., & Lacy, M. 1999, MNRAS, 309, 1017
Wylezalek, D., Galametz, A., Stern, D., et al. 2013, ApJ, 769, 79
Yuan, Z., Wang, J., Worrall, D. M., Zhang, B.-B., & Mao, J. 2018, ApJS, 239, 33
Zakamska, N. L., & Greene, J. E. 2014, MNRAS, 442, 784
Zakamska, N. L., Hamann, F., Pâris, I., et al. 2016, MNRAS, 459, 3144

Bibliography

M. A. Abramowicz, B. Czerny, J. P. Lasota, and E. Szuszkiewicz. Slim Accretion Disks. ApJ, 332:646, September 1988. doi: 10.1086/166683.

S. W. Allen, R. J. H. Dunn, A. C. Fabian, G. B. Taylor, and C. S. Reynolds. The relation between accretion rate and jet power in X-ray luminous elliptical galaxies. MNRAS, 372(1):21–30, October 2006. doi: 10.1111/j.1365-2966.2006.10778.x.

Tao An and Willem A. Baan. The Dynamic Evolution of Young Extragalactic Radio Sources. ApJ, 760 (1):77, November 2012. doi: 10.1088/0004-637X/760/1/77.

Robert Antonucci. Unified models for active galactic nuclei and quasars. ARA&A, 31:473–521, January 1993. doi: 10.1146/annurev.aa.31.090193.002353.

P. N. Appleton, D. T. Fadda, F. R. Marleau, D. T. Frayer, G. Helou, J. J. Condon, P. I. Choi, L. Yan, M. Lacy, G. Wilson, L. Armus, S. C. Chapman, F. Fang, I. Heinrichson, M. Im, B. T. Jannuzi, L. J. Storrie-Lombardi, D. Shupe, B. T. Soifer, G. Squires, and H. I. Teplitz. The Far- and Mid-Infrared/Radio Correlations in the Spitzer Extragalactic First Look Survey. ApJS, 154(1):147–150, September 2004. doi: 10.1086/422425.

Mark J. Avara, Jonathan C. McKinney, and Christopher S. Reynolds. Efficiency of thin magnetically arrested discs around black holes. MNRAS, 462(1):636–648, October 2016. doi: 10.1093/mnras/stw1643.

W. Baade and R. Minkowski. Identification of the Radio Sources in Cassiopeia, Cygnus A, and Puppis A. ApJ, 119:206, January 1954a. doi: 10.1086/145812.

W. Baade and R. Minkowski. On the Identification of Radio Sources. ApJ, 119:215, January 1954b. doi: 10.1086/145813.

Robert H. Becker, Richard L. White, and David J. Helfand. The VLA's FIRST Survey. In D. R. Crabtree, R. J. Hanisch, and J. Barnes, editors, *Astronomical Data Analysis Software and Systems III*, volume 61 of *Astronomical Society of the Pacific Conference Series*, page 165, January 1994.

M. C. Begelman and J. E. Pringle. Accretion discs with strong toroidal magnetic fields. MNRAS, 375 (3):1070–1076, March 2007. doi: 10.1111/j.1365-2966.2006.11372.x.

Mitchell C. Begelman and Denis F. Cioffi. Overpressured Cocoons in Extragalactic Radio Sources. ApJ, 345:L21, October 1989. doi: 10.1086/185542.

Mitchell C. Begelman and Joseph Silk. Magnetically elevated accretion discs in active galactic nuclei: broad emission-line regions and associated star formation. MNRAS, 464(2):2311–2317, January 2017. doi: 10.1093/mnras/stw2533.

Marco Berton and Emilia Järvelä. Peaked sources and narrow-line Seyfert 1s: A love story. *Astronomische Nachrichten*, 342(1066):1066–1070, November 2021. doi: 10.1002/asna.20210036.

G. V. Bicknell. A model for the surface brightness of a turbulent low mach number jet. I. Theoretical development and application to 3C 31. ApJ, 286:68–87, November 1984. doi: 10.1086/162577.

Jonathan Bird, Paul Martini, and Christian Kaiser. The Lifetime of FR II Sources in Groups and Clusters: Implications for Radio-Mode Feedback. ApJ, 676(1):147–162, March 2008. doi: 10.1086/527534.

Jeffrey A. Blackburne, David Pooley, Saul Rappaport, and Paul L. Schechter. Sizes and Temperature Profiles of Quasar Accretion Disks from Chromatic Microlensing. ApJ, 729(1):34, March 2011. doi: 10.1088/0004-637X/729/1/34.

R. D. Blandford and D. G. Payne. Hydromagnetic flows from accretion disks and the production of radio jets. MNRAS, 199:883–903, June 1982. doi: 10.1093/mnras/199.4.883.

R. D. Blandford and M. J. Rees. A "twin-exhaust" model for double radio sources. MNRAS, 169: 395–415, December 1974. doi: 10.1093/mnras/169.3.395.

R. D. Blandford and R. L. Znajek. Electromagnetic extraction of energy from Kerr black holes. MNRAS, 179:433–456, May 1977. doi: 10.1093/mnras/179.3.433.

Roger Blandford, David Meier, and Anthony Readhead. Relativistic Jets from Active Galactic Nuclei. ARA&A, 57:467–509, August 2019. doi: 10.1146/annurev-astro-081817-051948.

Katherine M. Blundell, Steve Rawlings, and Chris J. Willott. The Nature and Evolution of Classical Double Radio Sources from Complete Samples. AJ, 117(2):677–706, February 1999. doi: 10.1086/300721.

B. Boccardi, T. P. Krichbaum, U. Bach, F. Mertens, E. Ros, W. Alef, and J. A. Zensus. The stratified two-sided jet of <ASTROBJ>Cygnus A</ASTROBJ>. Acceleration and collimation. A&A, 585:A33, January 2016. doi: 10.1051/0004-6361/201526985.

D. C. J. Bock, M. I. Large, and Elaine M. Sadler. SUMSS: A Wide-Field Radio Imaging Survey of the Southern Sky. I. Science Goals, Survey Design, and Instrumentation. AJ, 117(3):1578–1593, March 1999. doi: 10.1086/300786.

J. G. Bolton, G. J. Stanley, and O. B. Slee. Positions of Three Discrete Sources of Galactic Radio-Frequency Radiation. Nature, 164(4159):101–102, July 1949. doi: 10.1038/164101b0.

C. Stuart Bowyer, Michael Lampton, John Mack, and Fernando de Mendonca. Detection of X-Ray Emission from 3c 273 and NGC 5128. ApJ, 161:L1, July 1970. doi: 10.1086/180559.

S. Bowyer, E. T. Byram, T. A. Chubb, and H. Friedman. X-ray Sources in the Galaxy. Nature, 201(4926): 1307–1308, March 1964. doi: 10.1038/2011307a0.

Alan H. Bridle and Richard A. Perley. Extragalactic Radio Jets. ARA&A, 22:319–358, January 1984. doi: 10.1146/annurev.aa.22.090184.001535.

C. Brocksopp, C. R. Kaiser, A. P. Schoenmakers, and A. G. de Bruyn. Three episodes of jet activity in the Fanaroff-Riley type II radio galaxy B0925+420. MNRAS, 382(3):1019–1028, December 2007. doi: 10.1111/j.1365-2966.2007.12483.x.

Omer Bromberg, Ehud Nakar, Tsvi Piran, and Re'em Sari. The Propagation of Relativistic Jets in External Media. ApJ, 740(2):100, October 2011. doi: 10.1088/0004-637X/740/2/100.

G. Bruni, J. L. Gómez, L. Vega-García, A. P. Lobanov, A. Fuentes, T. Savolainen, Y. Y. Kovalev, M. Perucho, J. M. Martí, J. M. Anderson, P. G. Edwards, L. I. Gurvits, M. M. Lisakov, A. B. Pushkarev, K. V. Sokolovsky, and J. A. Zensus. RadioAstron reveals a spine-sheath jet structure in 3C 273. A&A, 654:A27, October 2021. doi: 10.1051/0004-6361/202039423.

G. R. Burbidge. Estimates of the Total Energy in Particles and Magnetic Field in the Non-Thermal Radio Sources. ApJ, 129:849–852, May 1959. doi: 10.1086/146680.

K. W. Cavagnolo, B. R. McNamara, P. E. J. Nulsen, C. L. Carilli, C. Jones, and L. Bîrzan. A Relationship Between AGN Jet Power and Radio Power. ApJ, 720(2):1066–1072, September 2010. doi: 10.1088/0004-637X/720/2/1066.

Marco Chiaberge and Alessandro Marconi. On the origin of radio loudness in active galactic nuclei and its relationship with the properties of the central supermassive black hole. MNRAS, 416(2): 917–926, September 2011. doi: 10.1111/j.1365-2966.2011.19079.x.

M. Cirasuolo, A. Celotti, M. Magliocchetti, and L. Danese. Is there a dichotomy in the radio loudness distribution of quasars? MNRAS, 346(2):447–455, December 2003a. doi: 10.1046/j.1365-2966.2003.07105.x.

M. Cirasuolo, M. Magliocchetti, A. Celotti, and L. Danese. The radio-loud/radio-quiet dichotomy: news from the 2dF QSO Redshift Survey. MNRAS, 341(3):993–1004, May 2003b. doi: 10.1046/j.1365-8711.2003.06485.x.

J. J. Condon, W. D. Cotton, E. W. Greisen, Q. F. Yin, R. A. Perley, G. B. Taylor, and J. J. Broderick. The NRAO VLA Sky Survey. AJ, 115(5):1693–1716, May 1998. doi: 10.1086/300337.

J. H. Croston, J. Ineson, and M. J. Hardcastle. Particle content, radio-galaxy morphology, and jet power: all radio-loud AGN are not equal. MNRAS, 476(2):1614–1623, May 2018. doi: 10.1093/mnras/sty274.

H. D. Curtis. Descriptions of 762 Nebulae and Clusters Photographed with the Crossley Reflector. *Publications of Lick Observatory*, 13:9–42, January 1918.

Bożena Czerny, Aneta Siemiginowska, Agnieszka Janiuk, Błażej Nikiel-Wroczyński, and Łukasz Stawarz. Accretion Disk Model of Short-Timescale Intermittent Activity in Young Radio Sources. ApJ, 698(1):840–851, June 2009. doi: 10.1088/0004-637X/698/1/840.

P. Dabhade, H. J. A. Röttgering, J. Bagchi, T. W. Shimwell, M. J. Hardcastle, S. Sankhyayan, R. Morganti, M. Jamrozy, A. Shulevski, and K. J. Duncan. Giant radio galaxies in the LOFAR Two-metre Sky Survey. I. Radio and environmental properties. A&A, 635:A5, March 2020. doi: 10.1051/0004-6361/201935589.

Shane W. Davis and Alexander Tchekhovskoy. Magnetohydrodynamics Simulations of Active Galactic Nucleus Disks and Jets. ARA&A, 58:407–439, August 2020. doi: 10.1146/annurev-astro-081817-051905.

W. H. de Vries, R. H. Becker, and R. L. White. Double-Lobed Radio Quasars from the Sloan Digital Sky Survey. AJ, 131(2):666–679, February 2006. doi: 10.1086/499303.

Jason Dexter and Mitchell C. Begelman. Extreme AGN variability: evidence of magnetically elevated accretion? MNRAS, 483(1):L17–L21, February 2019. doi: 10.1093/mnrasl/sly213.

M. Elvis, G. Risaliti, and G. Zamorani. Most Supermassive Black Holes Must Be Rapidly Rotating. ApJ, 565(2):L75–L77, February 2002. doi: 10.1086/339197.

Martin Elvis. The Quasar Continuum. In Bradley M. Peterson, Rachel S. Somerville, and Thaisa Storchi-Bergmann, editors, *Co-Evolution of Central Black Holes and Galaxies*, volume 267, pages 55–64, May 2010. doi: 10.1017/S1743921310005570.

A. C. Fabian. Observational Evidence of Active Galactic Nuclei Feedback. ARA&A, 50:455–489, September 2012. doi: 10.1146/annurev-astro-081811-125521.

S. A. E. G. Falle. Self-similar jets. MNRAS, 250:581–596, June 1991. doi: 10.1093/mnras/250.3.581.

B. L. Fanaroff and J. M. Riley. The morphology of extragalactic radio sources of high and low luminosity. MNRAS, 167:31P–36P, May 1974. doi: 10.1093/mnras/167.1.31P.

N. Fanidakis, C. M. Baugh, A. J. Benson, R. G. Bower, S. Cole, C. Done, and C. S. Frenk. Grand unification of AGN activity in the ΛCDM cosmology. MNRAS, 410(1):53–74, January 2011. doi: 10.1111/j.1365-2966.2010.17427.x.

C. A. C. Fernandes, M. J. Jarvis, S. Rawlings, A. Martínez-Sansigre, E. Hatziminaoglou, M. Lacy, M. J. Page, J. A. Stevens, and E. Vardoulaki. Evidence for a maximum jet efficiency for the most powerful radio galaxies. MNRAS, 411(3):1909–1916, March 2011. doi: 10.1111/j.1365-2966.2010.17820.x.

H. Friedman and E. T. Byram. X-rays from Sources 3C 273 and M 87. *Science*, 158(3798):257–259, October 1967. doi: 10.1126/science.158.3798.257.

S. T. Garrington, J. P. Leahy, R. G. Conway, and R. A. Laing. A systematic asymmetry in the polarization properties of double radio sources with one jet. Nature, 331(6152):147–149, January 1988. doi: 10.1038/331147a0.

Riccardo Giacconi, Herbert Gursky, Frank R. Paolini, and Bruno B. Rossi. Evidence for x Rays From Sources Outside the Solar System. Phys. Rev. Lett., 9(11):439–443, December 1962. doi: 10.1103/PhysRevLett.9.439.

L. E. H. Godfrey and S. S. Shabala. AGN Jet Kinetic Power and the Energy Budget of Radio Galaxy Lobes. ApJ, 767(1):12, April 2013. doi: 10.1088/0004-637X/767/1/12.

L. E. H. Godfrey and S. S. Shabala. Mutual distance dependence drives the observed jet-power-radio-luminosity scaling relations in radio galaxies. MNRAS, 456(2):1172–1184, February 2016. doi: 10.1093/mnras/stv2712.

L. E. H. Godfrey, J. E. J. Lovell, S. Burke-Spolaor, R. Ekers, G. V. Bicknell, M. Birkinshaw, D. M. Worrall, D. L. Jauncey, D. A. Schwartz, H. L. Marshall, J. Gelbord, E. S. Perlman, and M. Georganopoulos. Periodic Structure in the Megaparsec-scale Jet of PKS 0637-752. ApJ, 758(2):L27, October 2012. doi: 10.1088/2041-8205/758/2/L27.

Jeremy Goodman. Self-gravity and quasi-stellar object discs. MNRAS, 339(4):937–948, March 2003. doi: 10.1046/j.1365-8711.2003.06241.x.

Gopal-Krishna and P. J. Wiita. Extragalactic radio sources with hybrid morphology: implications for the Fanaroff-Riley dichotomy. A&A, 363:507–516, November 2000.

Alister W. Graham. The black hole mass - spheroid luminosity relation. MNRAS, 379(2):711–722, August 2007. doi: 10.1111/j.1365-2966.2007.11950.x.

Jenny E. Greene and Luis C. Ho. Estimating Black Hole Masses in Active Galaxies Using the Hα Emission Line. ApJ, 630(1):122–129, September 2005. doi: 10.1086/431897.

Jesse L. Greenstein. Red-Shift of the Unusual Radio Source: 3C 48. Nature, 197(4872):1041–1042, March 1963. doi: 10.1038/1971041a0.

Maitrayee Gupta, Marek Sikora, Katarzyna Rusinek, and Greg M. Madejski. Comparison of hard X-ray spectra of luminous radio galaxies and their radio-quiet counterparts. MNRAS, 480(3):2861–2871, November 2018. doi: 10.1093/mnras/sty2043.

Maitrayee Gupta, Marek Sikora, and Katarzyna Rusinek. Comparison of SEDs of very massive radio-loud and radio-quiet AGN. MNRAS, 492(1):315–325, February 2020. doi: 10.1093/mnras/stz3384.

R. Hanbury Brown, R. C. Jennison, and M. K. Das Gupta. Apparent Angular Sizes of Discrete Radio Sources: Observations at Jodrell Bank, Manchester. Nature, 170(4338):1061–1063, December 1952. doi: 10.1038/1701061a0.

M. J. Hardcastle and J. H. Croston. Radio galaxies and feedback from AGN jets. New A Rev., 88: 101539, June 2020. doi: 10.1016/j.newar.2020.101539.

M. J. Hardcastle and M. G. H. Krause. Numerical modelling of the lobes of radio galaxies in cluster environments. MNRAS, 430(1):174–196, March 2013. doi: 10.1093/mnras/sts564.

D. E. Harris and Henric Krawczynski. X-Ray Emission from Extragalactic Jets. ARA&A, 44(1):463–506, September 2006. doi: 10.1146/annurev.astro.44.051905.092446.

Jeremy J. Harwood, Tessa Vernstrom, and Andra Stroe. Unveiling the cause of hybrid morphology radio sources (HyMoRS). MNRAS, 491(1):803–822, January 2020. doi: 10.1093/mnras/stz3069.

John F. Hawley, Christian Fendt, Martin Hardcastle, Elena Nokhrina, and Alexander Tchekhovskoy. Disks and Jets. Gravity, Rotation and Magnetic Fields. Space Sci. Rev., 191(1-4):441–469, October 2015. doi: 10.1007/s11214-015-0174-7.

C. Hazard, M. B. Mackey, and A. J. Shimmins. Investigation of the Radio Source 3C 273 By The Method of Lunar Occultations. Nature, 197(4872):1037–1039, March 1963. doi: 10.1038/1971037a0.

Luis C. Ho. On the Relationship between Radio Emission and Black Hole Mass in Galactic Nuclei. ApJ, 564(1):120–132, January 2002. doi: 10.1086/324399.

Ananda Hota, S. K. Sirothia, Youichi Ohyama, C. Konar, Suk Kim, Soo-Chang Rey, D. J. Saikia, J. H. Croston, and Satoki Matsushita. Discovery of a spiral-host episodic radio galaxy. MNRAS, 417(1): L36–L40, October 2011. doi: 10.1111/j.1745-3933.2011.01115.x.

F. Hoyle and W. A. Fowler. On the nature of strong radio sources. MNRAS, 125:169, January 1963a. doi: 10.1093/mnras/125.2.169.

F. Hoyle and William A. Fowler. Nature of Strong Radio Sources. Nature, 197(4867):533–535, February 1963b. doi: 10.1038/197533a0.

Igor V. Igumenshchev. Magnetically Arrested Disks and the Origin of Poynting Jets: A Numerical Study. ApJ, 677(1):317–326, April 2008. doi: 10.1086/529025.

Yoshiyuki Inoue, Akihiro Doi, Yasuyuki T. Tanaka, Marek Sikora, and Grzegorz M. Madejski. Disk-Jet Connection in Active Supermassive Black Holes in the Standard Accretion Disk Regime. ApJ, 840 (1):46, May 2017. doi: 10.3847/1538-4357/aa6b57.

Željko Ivezić, Kristen Menou, Gillian R. Knapp, Michael A. Strauss, Robert H. Lupton, Daniel E. Vanden Berk, Gordon T. Richards, Christy Tremonti, Michael A. Weinstein, Scott Anderson, Neta A. Bahcall, Robert H. Becker, Mariangela Bernardi, Michael Blanton, Daniel Eisenstein, Xiaohui Fan, Douglas Finkbeiner, Kristian Finlator, Joshua Frieman, James E. Gunn, Pat B. Hall, Rita S. J. Kim, Ali Kinkhabwala, Vijay K. Narayanan, Constance M. Rockosi, David Schlegel, Donald P. Schneider, Iskra Strateva, Mark SubbaRao, Aniruddha R. Thakar, Wolfgang Voges, Richard L. White, Brian Yanny, Jonathan Brinkmann, Mamoru Doi, Masataka Fukugita, Gregory S. Hennessy, Jeffrey A. Munn, Robert C. Nichol, and Donald G. York. Optical and Radio Properties of Extragalactic Sources Observed by the FIRST Survey and the Sloan Digital Sky Survey. AJ, 124(5):2364–2400, November 2002. doi: 10.1086/344069.

Agnieszka Janiuk and Bożena Czerny. On different types of instabilities in black hole accretion discs: implications for X-ray binaries and active galactic nuclei. MNRAS, 414(3):2186–2194, July 2011. doi: 10.1111/j.1365-2966.2011.18544.x.

Karl G. Jansky. Radio Waves from Outside the Solar System. Nature, 132(3323):66, July 1933. doi: 10.1038/132066a0.

Michael Janssen, Heino Falcke, Matthias Kadler, Eduardo Ros, Maciek Wielgus, Kazunori Akiyama, Mislav Baloković, Lindy Blackburn, Katherine L. Bouman, Andrew Chael, Chi-kwan Chan, Koushik Chatterjee, Jordy Davelaar, Philip G. Edwards, Christian M. Fromm, José L. Gómez, Ciriaco Goddi,

Sara Issaoun, Michael D. Johnson, Junhan Kim, Jun Yi Koay, Thomas P. Krichbaum, Jun Liu, Elisabetta Liuzzo, Sera Markoff, Alex Markowitz, Daniel P. Marrone, Yosuke Mizuno, Cornelia Müller, Chunchong Ni, Dominic W. Pesce, Venkatessh Ramakrishnan, Freek Roelofs, Kazi L. J. Rygl, Ilse van Bemmel, Event Horizon Telescope Collaboration, Antxon Alberdi, Walter Alef, Juan Carlos Algaba, Richard Anantua, Keiichi Asada, Rebecca Azulay, Anne-Kathrin Baczko, David Ball, David Ball, John Barrett, Bradford A. Benson, Dan Bintley, Dan Bintley, Raymond Blundell, Wilfred Boland, Wilfred Boland, Geoffrey C. Bower, Hope Boyce, Michael Bremer, Christiaan D. Brinkerink, Roger Brissenden, Silke Britzen, Avery E. Broderick, Dominique Broguiere, Thomas Bronzwaer, Do-Young Byun, John E. Carlstrom, Shami Chatterjee, Ming-Tang Chen, Yongjun Chen, Paul M. Chesler, Ilje Cho, Pierre Christian, John E. Conway, James M. Cordes, Thomas M. Crawford, Geoffrey B. Crew, Alejandro Cruz-Osorio, Yuzhu Cui, Yuzhu Cui, Mariafelicia De Laurentis, Roger Deane, Jessica Dempsey, Gregory Desvignes, Jason Dexter, Sheperd S. Doeleman, Ralph P. Eatough, Joseph Farah, Joseph Farah, Vincent L. Fish, Ed Fomalont, H. Alyson Ford, Raquel Fraga-Encinas, Per Friberg, Per Friberg, Antonio Fuentes, Peter Galison, Charles F. Gammie, Roberto García, Zachary Gelles, Olivier Gentaz, Boris Georgiev, Boris Georgiev, Roman Gold, Roman Gold, Arturo I. Gómez-Ruiz, Minfeng Gu, Mark Gurwell, Kazuhiro Hada, Daryl Haggard, Michael H. Hecht, Ronald Hesper, Elizabeth Himwich, Luis C. Ho, Paul Ho, Mareki Honma, Chih-Wei L. Huang, Lei Huang, David H. Hughes, Shiro Ikeda, Makoto Inoue, Makoto Inoue, David J. James, Buell T. Jannuzi, Buell T. Jannuzi, Britton Jeter, Wu Jiang, Alejandra Jimenez-Rosales, Alejandra Jimenez-Rosales, Svetlana Jorstad, Taehyun Jung, Mansour Karami, Ramesh Karuppusamy, Tomohisa Kawashima, Garrett K. Keating, Mark Kettenis, Dong-Jin Kim, Jae-Young Kim, Jae-Young Kim, Jongsoo Kim, Motoki Kino, Motoki Kino, Yutaro Kofuji, Shoko Koyama, Michael Kramer, Carsten Kramer, Carsten Kramer, Cheng-Yu Kuo, Tod R. Lauer, Sang-Sung Lee, Aviad Levis, Yan-Rong Li, Zhiyuan Li, Michael Lindqvist, Rocco Lico, Greg Lindahl, Greg Lindahl, Kuo Liu, Kuo Liu, Wen-Ping Lo, Andrei P. Lobanov, Laurent Loinard, Colin Lonsdale, Ru-Sen Lu, Nicholas R. MacDonald, Jirong Mao, Nicola Marchili, Nicola Marchili, Nicola Marchili, Alan P. Marscher, Iván Martí-Vidal, Satoki Matsushita, Lynn D. Matthews, Lia Medeiros, Karl M. Menten, Izumi Mizuno, Izumi Mizuno, James M. Moran, Kotaro Moriyama, Monika Moscibrodzka, Monika Moscibrodzka, Gibwa Musoke, Alejandro Mus Mejías, Hiroshi Nagai, Neil M. Nagar, Masanori Nakamura, Ramesh Narayan, Gopal Narayanan, Iniyan Natarajan, Antonios Nathanail, Joey Neilsen, Roberto Neri, Roberto Neri, Aristeidis Noutsos, Michael A. Nowak, Hiroki Okino, Héctor Olivares, Gisela N. Ortiz-León, Tomoaki Oyama, Feryal Özel, Daniel C. M. Palumbo, Jongho Park, Nimesh Patel, Ue-Li Pen, Ue-Li Pen, Vincent Piétu, Richard Plambeck, Aleksandar PopStefanija, Oliver Porth, Felix M. Pötzl, Ben Prather, Jorge A. Preciado-López, Dimitrios Psaltis, Hung-Yi Pu, Hung-Yi Pu, Ramprasad Rao, Mark G. Rawlings, Alexander W. Raymond, Luciano Rezzolla, Angelo Ricarte, Bart Ripperda, Bart Ripperda, Alan Rogers, Alan Rogers, Mel Rose, Arash Roshanineshat, Helge Rottmann, Alan L. Roy, Chet Ruszczyk, Chet Ruszczyk, Salvador Sánchez, David Sánchez-Arguelles, Mahito Sasada, Tuomas Savolainen, F. Peter Schloerb, Karl-Friedrich Schuster, Lijing Shao, Zhiqiang Shen, Des Small, Bong Won Sohn, Jason SooHoo, He Sun, Fumie Tazaki, Alexandra J. Tetarenko, Paul Tiede, Remo P. J. Tilanus, Michael Titus, Pablo Torne, Tyler Trent, Efthalia Traianou, Sascha Trippe, Ilse van Bemmel, Huib Jan van Langevelde, Daniel R. van Rossum, Jan Wagner, Derek Ward-Thompson, John Wardle, Jonathan Weintroub, Norbert Wex, Robert Wharton, Robert Wharton, George N.

Wong, Qingwen Wu, Doosoo Yoon, André Young, Ken Young, Ziri Younsi, Feng Yuan, Ye-Fei Yuan, J. Anton Zensus, Guang-Yao Zhao, and Shan-Shan Zhao. Event Horizon Telescope observations of the jet launching and collimation in Centaurus A. *Nature Astronomy*, 5:1017–1028, July 2021. doi: 10.1038/s41550-021-01417-w.

E. Järvelä, A. Lähteenmäki, H. Lietzen, A. Poudel, P. Heinämäki, and M. Einasto. Large-scale environments of narrow-line Seyfert 1 galaxies. A&A, 606:A9, September 2017. doi: 10.1051/0004-6361/201731318.

R. C. Jennison and M. K. Das Gupta. Fine Structure of the Extra-terrestrial Radio Source Cygnus I. Nature, 172(4387):996–997, November 1953. doi: 10.1038/172996a0.

Linhua Jiang, Xiaohui Fan, Željko Ivezić, Gordon T. Richards, Donald P. Schneider, Michael A. Strauss, and Brandon C. Kelly. The Radio-Loud Fraction of Quasars is a Strong Function of Redshift and Optical Luminosity. ApJ, 656(2):680–690, February 2007. doi: 10.1086/510831.

Christian R. Kaiser and Paul Alexander. A self-similar model for extragalactic radio sources. MNRAS, 286(1):215–222, March 1997. doi: 10.1093/mnras/286.1.215.

K. I. Kellermann, R. Sramek, M. Schmidt, D. B. Shaffer, and R. Green. VLA Observations of Objects in the Palomar Bright Quasar Survey. AJ, 98:1195, October 1989. doi: 10.1086/115207.

Kenneth I. Kellermann and Frazer N. Owen. *Radio Galaxies and Quasars*, pages 563–602. Springer New York, New York, NY, 1988. ISBN 978-1-4612-3936-9. doi: 10.1007/978-1-4612-3936-9_13. URL https://doi.org/10.1007/978-1-4612-3936-9_13.

Amy E. Kimball, K. I. Kellermann, J. J. Condon, Željko Ivezić, and Richard A. Perley. The Two-component Radio Luminosity Function of Quasi-stellar Objects: Star Formation and Active Galactic Nucleus. ApJ, 739(1):L29, September 2011. doi: 10.1088/2041-8205/739/1/L29.

Serguei Komissarov and Oliver Porth. Numerical simulations of jets. New A Rev., 92:101610, June 2021. doi: 10.1016/j.newar.2021.101610.

C. Konar, D. J. Saikia, M. Jamrozy, and J. Machalski. Spectral ageing analysis of the double-double radio galaxy J1453+3308. MNRAS, 372(2):693–702, October 2006. doi: 10.1111/j.1365-2966.2006.10874.x.

Dorota Kozieł-Wierzbowska, Arti Goyal, and Natalia Żywucka. Radio Sources Associated with Optical Galaxies and Having Unresolved or Extended Morphologies (ROGUE). I. A Catalog of SDSS Galaxies with FIRST Core Identifications. ApJS, 247(2):53, April 2020. doi: 10.3847/1538-4365/ab63d3.

Rachael M. Kratzer and Gordon T. Richards. Mean and Extreme Radio Properties of Quasars and the Origin of Radio Emission. AJ, 149(2):61, February 2015. doi: 10.1088/0004-6256/149/2/61.

Julian H. Krolik and Mitchell C. Begelman. Molecular Tori in Seyfert Galaxies: Feeding the Monster and Hiding It. ApJ, 329:702, June 1988. doi: 10.1086/166414.

M. Kunert-Bajraszewska, M. P. Gawroński, A. Labiano, and A. Siemiginowska. A survey of low-luminosity compact sources and its implication for the evolution of radio-loud active galactic nuclei - I. Radio data. MNRAS, 408(4):2261–2278, November 2010. doi: 10.1111/j.1365-2966.2010.17271.x.

A. Kuźmicz and M. Jamrozy. Optical and radio properties of giant radio quasars: central black hole characteristics. MNRAS, 426(2):851–867, October 2012. doi: 10.1111/j.1365-2966.2012.21576.x.

Agnieszka Kuźmicz, Marek Jamrozy, Katarzyna Bronarska, Katarzyna Janda-Boczar, and D. J. Saikia. An Updated Catalog of Giant Radio Sources. ApJS, 238(1):9, September 2018. doi: 10.3847/1538-4365/aad9ff.

M. Lacy, S. E. Ridgway, A. Sajina, A. O. Petric, E. L. Gates, T. Urrutia, and L. J. Storrie-Lombardi. The Spitzer Mid-infrared AGN Survey. II. The Demographics and Cosmic Evolution of the AGN Population. ApJ, 802(2):102, April 2015. doi: 10.1088/0004-637X/802/2/102.

Debora Lančová, David Abarca, Włodek Kluźniak, Maciek Wielgus, Aleksander Sądowski, Ramesh Narayan, Jan Schee, Gabriel Török, and Marek Abramowicz. Puffy Accretion Disks: Sub-Eddington, Optically Thick, and Stable. ApJ, 884(2):L37, October 2019. doi: 10.3847/2041-8213/ab48f5.

J. P. Leahy and P. Parma. Multiple outbursts in radio galaxies. In Jacques Roland, Hilhne Sol, and Guy Pelletier, editors, *Extragalactic Radio Sources. From Beams to Jets*, pages 307–308, January 1992.

Michael J. Ledlow and Frazer N. Owen. 20 CM VLA Survey of Abell Clusters of Galaxies. VI. Radio/Optical Luminosity Functions. AJ, 112:9, July 1996. doi: 10.1086/117985.

D. Lynden-Bell. Galactic Nuclei as Collapsed Old Quasars. Nature, 223(5207):690–694, August 1969. doi: 10.1038/223690a0.

D. Macconi, E. Torresi, P. Grandi, B. Boccardi, and C. Vignali. Radio morphology-accretion mode link in Fanaroff-Riley type II low-excitation radio galaxies. MNRAS, 493(3):4355–4366, April 2020. doi: 10.1093/mnras/staa560.

Elizabeth K. Mahony, Elaine M. Sadler, Scott M. Croom, Ronald D. Ekers, Ilana J. Feain, and Tara Murphy. Is the Observed High-frequency Radio Luminosity Distribution of QSOs Bimodal? ApJ, 754(1):12, July 2012. doi: 10.1088/0004-637X/754/1/12.

Alessandro Marconi and Leslie K. Hunt. The Relation between Black Hole Mass, Bulge Mass, and Near-Infrared Luminosity. ApJ, 589(1):L21–L24, May 2003. doi: 10.1086/375804.

T. Mauch, T. Murphy, H. J. Buttery, J. Curran, R. W. Hunstead, B. Piestrzynski, J. G. Robertson, and E. M. Sadler. SUMSS: a wide-field radio imaging survey of the southern sky - II. The source catalogue. MNRAS, 342(4):1117–1130, July 2003. doi: 10.1046/j.1365-8711.2003.06605.x.

Jonathan C. McKinney, Alexander Tchekhovskoy, and Roger D. Blandford. General relativistic magnetohydrodynamic simulations of magnetically choked accretion flows around black holes. MNRAS, 423(4):3083–3117, July 2012. doi: 10.1111/j.1365-2966.2012.21074.x.

B. R. McNamara and P. E. J. Nulsen. Heating Hot Atmospheres with Active Galactic Nuclei. ARA&A, 45(1):117–175, September 2007. doi: 10.1146/annurev.astro.45.051806.110625.

G. Miley. The structure of extended extragalactic radio sources. ARA&A, 18:165–218, January 1980. doi: 10.1146/annurev.aa.18.090180.001121.

G. K. Miley, G. Neugebauer, and B. T. Soifer. IRAS observations of Seyfert galaxies. ApJ, 293:L11–L14, June 1985. doi: 10.1086/184481.

B. Mingo, J. H. Croston, M. J. Hardcastle, P. N. Best, K. J. Duncan, R. Morganti, H. J. A. Rottgering, J. Sabater, T. W. Shimwell, W. L. Williams, M. Brienza, G. Gurkan, V. H. Mahatma, L. K. Morabito, I. Prandoni, M. Bondi, J. Ineson, and S. Mooney. Revisiting the Fanaroff-Riley dichotomy and radio-galaxy morphology with the LOFAR Two-Metre Sky Survey (LoTSS). MNRAS, 488(2):2701–2721, September 2019. doi: 10.1093/mnras/stz1901.

Christopher W. Morgan, Gregory E. Hyer, Vivien Bonvin, Ana M. Mosquera, Matthew Cornachione, Frederic Courbin, Christopher S. Kochanek, and Emilio E. Falco. Accretion Disk Size Measurement and Time Delays in the Lensed Quasar WFI 2033-4723. ApJ, 869(2):106, December 2018. doi: 10.3847/1538-4357/aaed3e.

S. Nandi and D. J. Saikia. Double-double radio galaxies from the FIRST survey. *Bulletin of the Astronomical Society of India*, 40(2):121–137, June 2012.

Ramesh Narayan, Igor V. Igumenshchev, and Marek A. Abramowicz. Magnetically Arrested Disk: an Energetically Efficient Accretion Flow. PASJ, 55:L69–L72, December 2003. doi: 10.1093/pasj/55.6.L69.

Hagai Netzer. Accretion and star formation rates in low-redshift type II active galactic nuclei. MNRAS, 399(4):1907–1920, November 2009. doi: 10.1111/j.1365-2966.2009.15434.x.

Hagai Netzer. Revisiting the Unified Model of Active Galactic Nuclei. ARA&A, 53:365–408, August 2015. doi: 10.1146/annurev-astro-082214-122302.

I. D. Novikov and K. S. Thorne. Astrophysics of black holes. In *Black Holes (Les Astres Occlus)*, pages 343–450, January 1973.

Christopher P. O'Dea. The Compact Steep-Spectrum and Gigahertz Peaked-Spectrum Radio Sources. PASP, 110(747):493–532, May 1998. doi: 10.1086/316162.

Christopher P. O'Dea and Stefi A. Baum. Constraints on Radio Source Evolution from the Compact Steep Spectrum and GHz Peaked Spectrum Radio Sources. AJ, 113:148–161, January 1997. doi: 10.1086/118241.

Christopher P. O'Dea and D. J. Saikia. Compact steep-spectrum and peaked-spectrum radio sources. A&A Rev., 29(1):3, December 2021. doi: 10.1007/s00159-021-00131-w.

J. B. Oke. Absolute Energy Distribution in the Optical Spectrum of 3C 273. Nature, 197(4872):1040–1041, March 1963. doi: 10.1038/1971040b0.

F. N. Owen and M. J. Ledlow. The FRI/II Break and the Bivariate Luminosity Function in Abell Clusters of Galaxies. In Geoffrey V. Bicknell, Michael A. Dopita, and Peter J. Quinn, editors, *The Physics of Active Galaxies*, volume 54 of *Astronomical Society of the Pacific Conference Series*, page 319, January 1994.

Paolo Padovani. On the two main classes of active galactic nuclei. *Nature Astronomy*, 1:0194, August 2017. doi: 10.1038/s41550-017-0194.

Brian Punsly. Kinetically dominated FRII radio sources. MNRAS, 374(1):L10–L14, January 2007. doi: 10.1111/j.1745-3933.2006.00254.x.

Brian Punsly, Igor V. Igumenshchev, and Shigenobu Hirose. Three-Dimensional Simulations of Vertical Magnetic Flux in the Immediate Vicinity of Black Holes. ApJ, 704(2):1065–1085, October 2009. doi: 10.1088/0004-637X/704/2/1065.

Stephen E. Rafter, D. Michael Crenshaw, and Paul J. Wiita. Radio Properties of Low-Redshift Broad Line Active Galactic Nuclei. AJ, 137(1):42–52, January 2009. doi: 10.1088/0004-6256/137/1/42.

Stephen E. Rafter, D. Michael Crenshaw, and Paul J. Wiita. Radio Properties of Low-redshift Broad-line Active Galactic Nuclei Including Extended Radio Sources. AJ, 141(3):85, March 2011. doi: 10.1088/0004-6256/141/3/85.

I. Raginski and Ari Laor. AGN coronal emission models - I. The predicted radio emission. MNRAS, 459(2):2082–2096, June 2016. doi: 10.1093/mnras/stw772.

Grote Reber. Cosmic Static. ApJ, 100:279, November 1944. doi: 10.1086/144668.

M. J. Rees. New Interpretation of Extragalactic Radio Sources. Nature, 229(5283):312–317, January 1971. doi: 10.1038/229312a0.

M. J. Rees. Accretion and the quasar phenomenon. Phys. Scr, 17:193–200, March 1978. doi: 10.1088/0031-8949/17/3/010.

Christopher S. Reynolds. Observing black holes spin. *Nature Astronomy*, 3:41–47, January 2019. doi: 10.1038/s41550-018-0665-z.

Christopher S. Reynolds and Mitchell C. Begelman. Intermittant Radio Galaxies and Source Statistics. ApJ, 487(2):L135–L138, October 1997. doi: 10.1086/310894.

Gordon T. Richards, Mark Lacy, Lisa J. Storrie-Lombardi, Patrick B. Hall, S. C. Gallagher, Dean C. Hines, Xiaohui Fan, Casey Papovich, Daniel E. Vanden Berk, George B. Trammell, Donald P. Schneider, Marianne Vestergaard, Donald G. York, Sebastian Jester, Scott F. Anderson, Tamás Budavári, and Alexander S. Szalay. Spectral Energy Distributions and Multiwavelength Selection of Type 1 Quasars. ApJS, 166(2):470–497, October 2006. doi: 10.1086/506525.

Frank M. Rieger, Valentí Bosch-Ramon, and Peter Duffy. Fermi acceleration in astrophysical jets. Ap&SS, 309(1-4):119–125, June 2007. doi: 10.1007/s10509-007-9466-z.

H. Rottmann. *Jet-Reorientation in X-shaped Radio Galaxies*. PhD thesis, -, August 2001.

A. Różańska, J. Malzac, R. Belmont, B. Czerny, and P. O. Petrucci. Warm and optically thick dissipative coronae above accretion disks. A&A, 580:A77, August 2015. doi: 10.1051/0004-6361/201526288.

Katarzyna Rusinek, Marek Sikora, Dorota Kozieł-Wierzbowska, and Leith Godfrey. On the efficiency of jet production in FR II radio galaxies and quasars. MNRAS, 466(2):2294–2301, April 2017. doi: 10.1093/mnras/stw3330.

Katarzyna Rusinek, Marek Sikora, Dorota Kozieł-Wierzbowska, and Maitrayee Gupta. On the Diversity of Jet Production Efficiency in Swift/BAT AGNs. ApJ, 900(2):125, September 2020. doi: 10.3847/1538-4357/aba75f.

Katarzyna Rusinek-Abarca and Marek Sikora. The Dependence of the Fraction of Radio Luminous Quasars on Redshift and its Theoretical Implications. ApJ, 922(2):202, December 2021. doi: 10.3847/1538-4357/ac2429.

M. Ryle and F. G. Smith. A New Intense Source of Radio-Frequency Radiation in the Constellation of Cassiopeia. Nature, 162(4116):462–463, September 1948. doi: 10.1038/162462a0.

E. E. Salpeter. Accretion of Interstellar Matter by Massive Objects. ApJ, 140:796–800, August 1964. doi: 10.1086/147973.

Allan Sandage. The Existence of a Major New Constituent of the Universe: the Quasistellar Galaxies. ApJ, 141:1560, May 1965. doi: 10.1086/148245.

D. B. Sanders, E. S. Phinney, G. Neugebauer, B. T. Soifer, and K. Matthews. Continuum Energy Distributions of Quasars: Shapes and Origins. ApJ, 347:29, December 1989. doi: 10.1086/168094.

P. A. G. Scheuer. Lobe asymmetry and the expansion speeds of radio sources. MNRAS, 277:331–340, November 1995. doi: 10.1093/mnras/277.1.331.

M. Schmidt. 3C 273 : A Star-Like Object with Large Red-Shift. Nature, 197(4872):1040, March 1963. doi: 10.1038/1971040a0.

Arno P. Schoenmakers, A. G. de Bruyn, H. J. A. Röttgering, H. van der Laan, and C. R. Kaiser. Radio galaxies with a 'double-double morphology' - I. Analysis of the radio properties and evidence for interrupted activity in active galactic nuclei. MNRAS, 315(2):371–380, June 2000. doi: 10.1046/j.1365-8711.2000.03430.x.

Andreas Schulze, Chris Done, Youjun Lu, Fupeng Zhang, and Yoshiyuki Inoue. Evidence for Higher Black Hole Spin in Radio-loud Quasars. ApJ, 849(1):4, November 2017. doi: 10.3847/1538-4357/aa9181.

S. S. Shabala and L. E. H. Godfrey. Size Dependence of the Radio-luminosity-Mechanical-power Correlation in Radio Galaxies. ApJ, 769(2):129, June 2013. doi: 10.1088/0004-637X/769/2/129.

N. I. Shakura and R. A. Sunyaev. Black holes in binary systems. Observational appearance. A&A, 24:337–355, 1973.

I. S. Shklovskii. On the Nature of Radio Galaxies. Soviet Ast., 6:465, February 1963.

Marek Sikora, Łukasz Stawarz, and Jean-Pierre Lasota. Radio Loudness of Active Galactic Nuclei: Observational Facts and Theoretical Implications. ApJ, 658(2):815–828, April 2007. doi: 10.1086/511972.

Marek Sikora, Grażyna Stasińska, Dorota Kozieł-Wierzbowska, Greg M. Madejski, and Natalia V. Asari. Constraining Jet Production Scenarios by Studies of Narrow-line Radio Galaxies. ApJ, 765(1): 62, March 2013. doi: 10.1088/0004-637X/765/1/62.

J. Singal, V. Petrosian, Ł. Stawarz, and A. Lawrence. The Radio and Optical Luminosity Evolution of Quasars. II. The SDSS Sample. ApJ, 764(1):43, February 2013. doi: 10.1088/0004-637X/764/1/43.

Lorenzo Sironi and Anatoly Spitkovsky. Relativistic Reconnection: An Efficient Source of Non-thermal Particles. ApJ, 783(1):L21, March 2014. doi: 10.1088/2041-8205/783/1/L21.

Aleksander Sądowski. Magnetic flux stabilizing thin accretion discs. MNRAS, 462(1):960–965, October 2016. doi: 10.1093/mnras/stw1852.

Krista Lynne Smith, Richard F. Mushotzky, Stuart Vogel, Thomas T. Shimizu, and Neal Miller. Radio Properties of the BAT AGNs: the FIR-radio Relation, the Fundamental Plane, and the Main Sequence of Star Formation. ApJ, 832(2):163, December 2016. doi: 10.3847/0004-637X/832/2/163.

M. D. Smith, M. L. Norman, K. H. A. Winkler, and L. Smarr. Hotspots in radio galaxies : a comparison with hydrodynamic simulations. MNRAS, 214:67–85, May 1985. doi: 10.1093/mnras/214.2.67.

A. Soltan. Masses of quasars. MNRAS, 200:115–122, July 1982. doi: 10.1093/mnras/200.1.115.

Maddalena Spada, Gabriele Ghisellini, Davide Lazzati, and Annalisa Celotti. Internal shocks in the jets of radio-loud quasars. MNRAS, 325(4):1559–1570, August 2001. doi: 10.1046/j.1365-8711.2001.04557.x.

P. A. Strittmatter, P. Hill, I. I. K. Pauliny-Toth, H. Steppe, and A. Witzel. Radio observations of optically selected quasars. A&A, 88(3):L12–L15, August 1980.

Clive Tadhunter. Radio AGN in the local universe: unification, triggering and evolution. A&A Rev., 24(1):10, June 2016. doi: 10.1007/s00159-016-0094-x.

Alexander Tchekhovskoy, Ramesh Narayan, and Jonathan C. McKinney. Efficient generation of jets from magnetically arrested accretion on a rapidly spinning black hole. MNRAS, 418(1):L79–L83, November 2011. doi: 10.1111/j.1745-3933.2011.01147.x.

Yuichi Terashima and Andrew S. Wilson. Chandra Snapshot Observations of Low-Luminosity Active Galactic Nuclei with a Compact Radio Source. ApJ, 583(1):145–158, January 2003. doi: 10.1086/345339.

Benny Trakhtenbrot and Hagai Netzer. Black hole growth to z = 2 - I. Improved virial methods for measuring M_{BH} and L/L_{Edd}. MNRAS, 427(4):3081–3102, December 2012. doi: 10.1111/j.1365-2966.2012.22056.x.

C. Megan Urry and Paolo Padovani. Unified Schemes for Radio-Loud Active Galactic Nuclei. PASP, 107:803, September 1995. doi: 10.1086/133630.

Sjoert van Velzen and Heino Falcke. The contribution of spin to jet-disk coupling in black holes. A&A, 557:L7, September 2013. doi: 10.1051/0004-6361/201322127.

Sjoert van Velzen, Heino Falcke, and Elmar Körding. Nature and evolution of powerful radio galaxies at z $\sim$ 1 and their link with the quasar luminosity function. MNRAS, 446(3):2985–3001, January 2015. doi: 10.1093/mnras/stu2213.

M. Volonteri, M. Sikora, J. P. Lasota, and A. Merloni. The Evolution of Active Galactic Nuclei and their Spins. ApJ, 775(2):94, October 2013. doi: 10.1088/0004-637X/775/2/94.

G. R. Werner, D. A. Uzdensky, M. C. Begelman, B. Cerutti, and K. Nalewajko. Non-thermal particle acceleration in collisionless relativistic electron-proton reconnection. MNRAS, 473(4):4840–4861, February 2018. doi: 10.1093/mnras/stx2530.

Richard L. White, Robert H. Becker, Michael D. Gregg, Sally A. Laurent-Muehleisen, Michael S. Brotherton, Chris D. Impey, Catherine E. Petry, Craig B. Foltz, Frederic H. Chaffee, Gordon T. Richards, William R. Oegerle, David J. Helfand, Richard G. McMahon, and Juan E. Cabanela. The FIRST Bright Quasar Survey. II. 60 Nights and 1200 Spectra Later. ApJS, 126(2):133–207, February 2000. doi: 10.1086/313300.

Richard L. White, David J. Helfand, Robert H. Becker, Eilat Glikman, and Wim de Vries. Signals from the Noise: Image Stacking for Quasars in the FIRST Survey. ApJ, 654(1):99–114, January 2007. doi: 10.1086/507700.

Sarah V. White, Matt J. Jarvis, Boris Häußler, and Natasha Maddox. Radio-quiet quasars in the VIDEO survey: evidence for AGN-powered radio emission at S_{1.4 GHz < 1} mJy. MNRAS, 448(3): 2665–2686, April 2015. doi: 10.1093/mnras/stv134.

P. N. Wilkinson, A. G. Polatidis, A. C. S. Readhead, W. Xu, and T. J. Pearson. Two-sided Ejection in Powerful Radio Sources: The Compact Symmetric Objects. ApJ, 432:L87, September 1994. doi: 10.1086/187518.

Chris J. Willott, Steve Rawlings, Katherine M. Blundell, and Mark Lacy. The emission line-radio correlation for radio sources using the 7C Redshift Survey. MNRAS, 309(4):1017–1033, November 1999. doi: 10.1046/j.1365-8711.1999.02907.x.

D. M. Worrall. The X-ray jets of active galaxies. A&A Rev., 17:1–46, January 2009. doi: 10.1007/s00159-008-0016-7.

Chun Xu, Mario Livio, and Stefi Baum. Radio-loud and Radio-quiet Active Galactic Nuclei. AJ, 118(3): 1169–1176, September 1999. doi: 10.1086/301007.

Feng Yuan and Ramesh Narayan. Hot Accretion Flows Around Black Holes. ARA&A, 52:529–588, August 2014. doi: 10.1146/annurev-astro-082812-141003.

Zunli Yuan, Jiancheng Wang, D. M. Worrall, Bin-Bin Zhang, and Jirong Mao. Determining the Core Radio Luminosity Function of Radio AGNs via Copula. ApJS, 239(2):33, December 2018. doi: 10.3847/1538-4365/aaed3b.

Nadia L. Zakamska, Fred Hamann, Isabelle Pâris, W. N. Brandt, Jenny E. Greene, Michael A. Strauss, Carolin Villforth, Dominika Wylezalek, Rachael M. Alexandroff, and Nicholas P. Ross. Discovery of

extreme [O III] λ5007 Å outflows in high-redshift red quasars. MNRAS, 459(3):3144–3160, July 2016. doi: 10.1093/mnras/stw718.

Ya. B. Zel'dovich. The Fate of a Star and the Evolution of Gravitational Energy Upon Accretion. *Soviet Physics Doklady*, 9:195, September 1964.

Wei Zheng, Gerard A. Kriss, Randal C. Telfer, John P. Grimes, and Arthur F. Davidsen. A Composite HST Spectrum of Quasars. ApJ, 475(2):469–478, February 1997. doi: 10.1086/303560.